



U. S. DEPARTMENT OF COMMERCE

Maurice H. Stans, Secretary

ENVIRONMENTAL SCIENCE SERVICES ADMINISTRATION

Robert M. White, Administrator

RESEARCH LABORATORIES

George S. Benton, Director

ESSA TECHNICAL REPORT ERL 112-ITS 80

Experimental Verification of an Ionospheric Channel Model

C.C. WATTERSON

J.R. JUROSHEK

W.D. BENSEMA

INSTITUTE FOR TELECOMMUNICATION SCIENCES
BOULDER, COLORADO
July 1969

For sale by the Superintendent of Documents, U.S. Government Printing Office, Washington, D.C. 20402
Price \$1.50

FOREWORD

This research was supported by
the Defense Communications Agency
under Reimbursable Order No. 24-65.

TABLE OF CONTENTS

	<u>Page</u>
FOREWORD	ii
GLOSSARY OF SYMBOLS	iv
ABSTRACT	x
1. INTRODUCTION	1
2. CHANNEL MODELS	4
2.1 General Models	4
2.2 Channel Characterization	8
2.3 Specific Models	22
2.4 Chosen Model	25
3. MEASURING TECHNIQUE	30
3.1 Method	30
3.2 Equipment	36
3.3 Measurements	45
4. ANALYTICAL METHODS	47
4.1 Deterministic Fit	48
4.2 Statistical Fit	51
4.3 Hypothesis Tests	55
5. RESULTS	61
5.1 Sample I1	61
5.2 Sample I2	69
5.3 Sample I3	77
6. CONCLUSIONS	83
7. ACKNOWLEDGMENTS	85
8. REFERENCES	86
APPENDIX A. Least-Squares Deterministic Fit	89
APPENDIX B. Least-Squares Statistical Fit	93
APPENDIX C. Effective Number of Independent Values	95
APPENDIX D. Tests of Correlation Estimates	101
APPENDIX E. Recommended Simulator Specifications	111
FIGURES	119

GLOSSARY OF SYMBOLS

Following is a list of symbols used in this report. Subscripts "m", "d", and "s" designating quantities in the measured, deterministic, and statistical channels, respectively, and horizontal bars above variables, designating normalized quantities, are not included in order to simplify the list. With three exceptions (B, P, and T), upper-case letters represent complex quantities and lower-case letters represent real quantities.

- $a, b =$ subscripts identifying the magnetoionic components.
- $B =$ bandwidth over which the statistical channel model is accurate.
- $\tilde{B} =$ bandwidth of a real Gaussian function.
- $B_{e,i} =$ effective bandwidth of the tap-gain spectrum for the i -th path.
- $c =$ integer controlling the abscissa spacing of values used in the least-squares statistical fit.
- $c_1(\Delta t), c_2(\Delta t) =$ true autocorrelation functions of real Gaussian functions.
- $c_{12}(\Delta t) =$ true crosscorrelation function of two real Gaussian functions.
- $\tilde{c}_1(\Delta t), \tilde{c}_2(\Delta t) =$ estimates of autocorrelation functions of real Gaussian functions.
- $\tilde{c}_{12}(\Delta t) =$ estimate of crosscorrelation function of two real Gaussian functions.
- $c_{d,i}(\Delta t) =$ true autocorrelation of $\underline{g}_{d,i}^l(t_r)$ and $\underline{\underline{g}}_{d,i}^l(t_r)$.
- $\underline{c}_i^l(\Delta t), \underline{\underline{c}}_i^l(\Delta t) =$ real and imaginary parts of $C_i^l(\Delta t)$.
- $C_i(\Delta t) =$ tap-gain correlation function for the i -th path.
- $C_i(0) =$ power ratio for the i -th path.
- $C_{ia}(0), C_{ib}(0) =$ power ratios for magnetoionic components of the i -th path.
- $\Delta C_{si}(\Delta t) =$ error in the least-squares statistical fit of $C_{si}(\Delta t)$ for the i -th path.

- d = subscript denoting a deterministic channel model quantity.
- $e_i(\ell)$ = expected number of independent values in the ℓ -th subinterval of an amplitude- or phase-density histogram for the i -th path.
- $e_{i1}^1(\ell), e_{i2}^1(\ell)$ = probability of a value in the ℓ -th subinterval in the amplitude- and phase-density histograms respectively for the i -th path.
- $E(f_k, t_r)$ = error in the deterministic fit for the channel.
- $E(f_k)$ = RMS value in time of $E(f_k, t_r)$.
- $E(k)$ = abbreviated version of $E(f_k, t_r)$ for any time, t_r .
- f = frequency.
- Δf = frequency in the domains of the correlation functions.
- f_c = frequency of the carrier.
- f_k = specific frequency of measurement.
- f_m = frequency of analog-to-digital conversion.
- F, F^{-1} = direct and inverse Fourier transform operators.
- $\underline{g}_1^1(t), \underline{g}_1^2(t)$ = real and imaginary parts of $G_1^1(t)$.
- $G_1(t)$ = tap-gain function for the i -th path.
- $G_1^1(t)$ = tap-gain function for the i -th path with linear phase component removed.
- $G_1^{II}(t)$ = intermediate tap-gain function in deterministic fit in frequency-domain method of measurement for the i -th path.
- $h(\tau, t)$ = impulse response of a time-varying channel.
- $H(f, t)$ = frequency response of a time-varying channel.
- $H(f_k)$ = RMS value in time of $H(f_k, t_r)$.
- $H(k)$ = abbreviated version of $H(f_k, t_r)$ for any time, t_r .
- i = integer subscript denoting the number of a path.
- $j = \sqrt{-1}$

- k = integer subscript denoting a specific frequency of measurement ($k = 1, 2, \dots, 11$).
- ℓ = general numbering integer.
- m_a = actual number of values in a sample for each frequency, f_k .
- m_a^1 = reduced actual number of values.
- m_{ci} = number of values used in the least-squares fit for the i -th path.
- m_{ei} = effective number of independent values for the i -th path.
- $m_{i1}(\ell), m_{i2}(\ell)$ = number of values observed to fall in the ℓ -th subinterval in the amplitude- and phase-density histograms respectively for the i -th path.
- n = number of paths.
- $o_i(\ell)$ = effective number of observed values in the ℓ -th subinterval of an amplitude- or phase-density histogram for the i -th path.
- $o_{i1}^1(\ell), o_{i2}^1(\ell)$ = fractional number of values observed to fall in the ℓ -th subinterval in the amplitude- and phase-density histograms respectively for the i -th path.
- p = probability density functions.
- P = cumulative distribution functions.
- r = integer subscript denoting a specific time.
- $R(\Delta f, \Delta t)$ = channel correlation function.
- $R(0, 0)$ = power ratio for a channel.
- $\Delta R_{dt}(\Delta f), \Delta R_{dt}(\Delta t)$ = difference between the deterministic and measured channel correlation functions on the frequency and time axes.
- $\Delta R_{st}(\Delta f), \Delta R_{st}(\Delta t)$ = difference between the statistical and measured channel correlation functions on the frequency and time axes.
- $R_o^1(\Delta f, \Delta t)$ = channel correlation function of hypothetical measured channel, with equal time spreads on all modes.

- s = subscript denoting a statistical channel model quantity.
- $s(\tau, \nu)$ = channel scatter function.
- t = time.
- Δt = time in the domains of the correlation functions.
- t_1 = integration time.
- t_m = time duration of a sample.
- t_r = specific times of analog-to-digital conversion.
- T = subscript denoting tabulated chi-square values.
- $u(\tau)$ = channel time-scatter function.
- $u_m^i(\tau)$ = channel time-scatter function of hypothetical measured channel with equal time spreads on all modes.
- $v(\nu)$ = channel frequency-scatter function.
- $v_i(\nu)$ = tap-gain spectrum for the i -th path.
- $x(t)$ = channel input signal in the time domain.
- $X(f)$ = channel input signal in the frequency domain.
- $y(t)$ = channel output signal in the time domain.
- $Y(f)$ = Fourier transform of $y(t)$.
- $Z_1(k) = \exp(-j2\pi T_1 f_k)$.
- α = general amplitude variable.
- $\alpha_{(\ell-1)}, \alpha_\ell$ = bounds on ℓ -th subinterval in amplitude- and phase-density histograms.
- $|\Gamma_{i\ell}|$ = magnitude of the crosscorrelation between the normalized deterministic tap-gain functions for the i -th and ℓ -th paths.
- $\delta(\tau)$ = Dirac delta function.
- δ_1, δ_2 = errors in least-squares deterministic fit.
- δ_{3i} = error in least-squares statistical fit for the i -th path.
- ϵ_{c1} = RMS value of the distribution of $|\Delta C_{s1}(\Delta t)|$.

- $\epsilon_{i\ell}$ = RMS value of the distribution of $|\Gamma_{i\ell}|$.
 ζ_1, ζ_2 = frequency-scaling constants.
 $\kappa(\Delta t)$ = general correlation function.
 $\lambda_{i1}, \lambda_{i2}$ = number of subintervals in the amplitude- and phase-density histograms respectively for the i-th path.
 ν = frequency in the scatter domain.
 $\hat{\nu}$ = channel frequency shift.
 ν_i = tap-gain frequency shift for the i-th path.
 ν_{ia}, ν_{ib} = frequency-shifts of the two magnetoionic components of the i-th path.
 ν_{ie} = mean differential frequency shift of the two magnetoionic components of the i-th path.
 $\pi = 3.1416$
 2ρ = channel time spread.
 $2\rho_e$ = effective time spread on each mode in the measured ionospheric channel.
 2σ = channel frequency spread.
 $2\sigma_i$ = tap-gain frequency spread for the i-th path.
 $2\sigma_{ia}, 2\sigma_{ib}$ = frequency spreads of the two magnetoionic components of the i-th path.
 $2\sigma_{ie}$ = mean frequency spread of the two magnetoionic components of the i-th path.
 $\sigma_n(\alpha, m_{e1})$ = standard deviation of the ordinate of a sample cumulative distribution of a Rayleigh-distributed variable as a function of its abscissa and the effective number of independent values.
 τ = time delay.
 $\hat{\tau}$ = channel time delay.
 τ_i = tap-gain time delay for the i-th path.
 $\tau_i''(t)$ = intermediate time-varying tap-gain time delay in the deterministic fit in the frequency-domain method of measurement for the i-th path.

χ_i^2 = chi-square values of amplitude- or phase-density
histograms for i-th path.

χ_{T1}^2 = tabulated values of chi-square.

ABSTRACT

→ Specially designed ionospheric propagation measurements were made and analyzed to confirm the validity and accuracy of a proposed ionospheric communication channel model. This stationary channel model incorporates a delay line that is fed by the input (transmitted) signal. Several adjustable taps on the delay line deliver signals with delays corresponding to the relative propagation times of typical ionospheric modes. Each delayed signal is modulated in amplitude and phase by an independent baseband complex bivariate Gaussian random function of time with a zero mean value and quadrature components with equal RMS values that produce Rayleigh fading.) Each random tap-gain function, in general, has a spectrum that is the sum of two Gaussian functions of frequency with independently adjustable amplitudes, frequency shifts, and frequency spreads. The two Gaussian terms in the spectrum represent the two magnetoionic components present in ionospheric modes. The delayed and modulated signals, one for each mode, are summed to form the output (received) signal.

Ionospheric measurements were made in 12-kHz bands at two HF frequencies over a 1294-km path. Three samples of 10- to 13-min duration were analyzed for typical daytime and nighttime propagation conditions. Statistical tests confirmed the validity of the hypotheses that the tap-gain functions are independent and have bivariate Gaussian distributions and that their spectrums are the sum of two Gaussian functions of frequency. The model is shown to be accurate over a band with a width that is about one-fourth of the reciprocal of the time spread on the modes (2.5, 8.0, and 12 kHz for the three samples).

Key words: Channel model, channel simulator, ionosphere, measurements, model.

EXPERIMENTAL VERIFICATION OF AN IONOSPHERIC CHANNEL MODEL

C. C. Watterson, J. R. Juroshek, and W. D. Bensema

1. INTRODUCTION

Historically, the evaluation of existing radio communication systems and the development and evaluation of new systems or techniques has usually required experimental measurements of their performance over actual communication links. Such evaluations must be made simultaneously with two or more systems over the same path to obtain meaningful results, because the propagation or channel conditions are uncontrolled and cannot accurately be repeated at other times and/or over other paths. Because of the disadvantages of on-the-air measurements, there has been a rapidly increasing interest in the past several years in the development of channel simulators that can be used in laboratory experiments to obtain similar but more comprehensive and meaningful evaluations of communication systems.

The advantages that laboratory experiments can have over on-the-air measurements are numerous:

- (a) Accuracy: Channel conditions can be mathematically described and reproduced accurately, allowing complementary theoretical and experimental studies to be made.
- (b) Stationarity: A stationary channel simulator imposes no time limitation on an experiment; many experiments requiring a number of hours are easy to perform on a stationary channel simulator but are impractical over actual ionospheric links.
- (c) Repeatability: Because channel conditions can be accurately defined and controlled, experimental simulator measurements made on one system at one time and place can be compared

meaningfully with similar measurements made on other systems at other times and places.

(d) Availability: Channel conditions can be selected at will, avoiding the need to wait for the desired combination of conditions that is necessary in on-the-air tests.

(e) Range: Channel conditions can profitably cover a range of values that exceeds the most extreme conditions of actual ionospheric links.

(f) Cost: Laboratory measurements with a channel simulator are quicker and less costly than similar on-the-air measurements.

However, the substantial advantages of laboratory simulator experiments over on-the-air evaluations are limited unless it is known that the channel model upon which the simulator design is based is both valid and accurate. A channel simulator based on an unproven channel model can possibly be a very useful laboratory tool, but the results it yields may not be typical of ionospheric channels and must be used with caution. While many measurements of the ionosphere have been made over the years, some detailed characteristics of ionospheric channels needed to specify a valid and accurate channel model have unfortunately not been available. Consequently, the validity and accuracy of some recently developed ionospheric channel simulators can be questioned, which in turn limits their value.

Therefore, in 1965, the Institute for Telecommunication Sciences and Aeronomy (ITSA)* of the Environmental Science Services Administration (ESSA) undertook a 3-year program with the support of the Defense Communications Agency (DCA) to develop an ionospheric channel model of proven validity and accuracy, which could be used both for theoretical analyses and for the design and construction of ionospheric channel

*Now the Institute for Telecommunication Sciences (ITS).

simulators. Subsequently, the program was expanded to include the development of an atmospheric noise model of proven validity and accuracy to increase the capability of the ionospheric channel model.

The specific tasks in the program were:

- (a) To develop specialized propagation-measuring equipment, to use this equipment for measurements of the ionospheric medium at high frequencies (HF) over a typical path, to analyze the measurements to determine the validity and accuracy of a proposed ionospheric channel model (exclusive of additive noise), and to recommend specifications for channel simulators based on the model.
- (b) To make a theoretical study of the relative advantages and disadvantages of building specially designed channel simulators rather than using large general-purpose digital computers for channel simulation in experimentally evaluating communication techniques or systems.
- (c) To design and build an ionospheric channel simulator for experimental use at the ESSA Research Laboratories if, as expected, the study in (b) showed specially designed channel simulators to be preferable.
- (d) To develop special atmospheric-noise recording equipment, to make recordings of atmospheric noise for a range of conditions, to design and build an experimental atmospheric noise simulator based upon a proposed model, to compare statistical analyses of the tape-recorded atmospheric noise with similar analyses of the output of the atmospheric noise simulator to determine the validity and accuracy of the noise model, and to recommend specifications for atmospheric noise simulators based on this model.

Reports on the results obtained in each of these four tasks are being submitted to the sponsor. This report describes the results of task (a).

Task (b) has already been reported by Quincy (1968); task (c) is being reported by Watterson et al. (1969), and task (d) by Coon et al. (1969). A fifth report is being submitted by Watterson and Coon (1969) combining the recommended specifications from tasks (a) and (d) for ionospheric channel and atmospheric noise simulators.

While the results of tasks (a) and (d) will define an ionospheric channel model that includes additive atmospheric noise, the term "channel model" throughout the remainder of this report will refer to models of ionospheric channels without additive noise.

2. CHANNEL MODELS

2.1 General Models

In considering possible channel models of the ionospheric medium for communication purposes, it is convenient to think of ionospheric channels as filters with complex frequency responses that vary with time, $H(f, t)$. Because the filter responses are random, they can be viewed as a random process. From present knowledge of the ionosphere we know that the process is nonstationary in both frequency and time. However, if consideration is restricted to band-limited channels with maximum bandwidths typical of practical communication systems (say 10 kHz), the process can be viewed as nearly stationary in frequency for channels in most parts of the spectrum. (Stationarity in this report will imply ergodicity.) An accurate model of the medium can therefore be stationary in frequency if the bandwidth is suitably limited, with a resulting considerable simplification of the model.

If sample functions of the process are sufficiently restricted in time (say 15 minutes), then the majority of such sample functions can be considered nearly stationary; therefore, the model also can be made stationary in time, with considerable additional simplifications resulting. Since the number of independent band-limited measurements of the medium

that can be taken in a few minutes is sufficient to determine the statistical parameters and the accuracy of the model with reasonable confidence, the validity and accuracy of such a stationary model can be experimentally verified.

A stationary channel model, in addition to being considerably simpler to define and easier to instrument than a nonstationary model, has another considerable advantage: the theoretical or experimental results obtained from its use are independent of the duration of the analysis or measurement (assuming a duration sufficient for a good estimate). In such analyses or measurements with a stationary model, the results describe the system performance expected over the ionospheric medium during the few-minute interval that the model represents. A change in the model parameters allows it to accurately represent the channel at other times or other channels with different transmitting-receiving locations and/or different frequencies. This advantage of stationarity is evident in experiments where an hour or more of measurements is required to obtain sufficient data (for example, measurements of low average error rates in a digital systems). It is difficult to obtain meaningful measurements of this type over a nonstationary ionospheric path or a nonstationary simulator, because the channel conditions are difficult to define, but very meaningful measurements can be obtained with a stationary simulator because the channel conditions can be described relatively easily and with considerable accuracy. However, it must be realized that the confidence with which one can accept the validity of a model decreases as the duration of an experiment increases beyond the time duration of the measurements that were used to validate the model. Even though the model is less reliable for longer experiments, it still produces results that are very meaningful; i. e., they are produced under conditions that can be accurately described.

Because of the advantages that a band-limited stationary model has over a nonstationary one, we decided to select a band-limited stationary

model that seemed most suitable and to experimentally determine the validity and accuracy of this model from analyses of propagation measurements. Two types of stationary models were considered: (a) a tapped-delay-line model with equally spaced taps and (b) a tapped-delay-line model with unequally spaced taps. Block diagrams of these models are presented in figure 1. In both models, the input (transmitted) signal is fed to an ideal delay line, and undistorted delayed versions of the input signal are delivered to a number of taps. (In fig. 1 and throughout this report, the word "tap" means a delay-line connection whose output signal is used, not an unused connection on the delay line.) The signal delivered to each tap is suitably modulated in amplitude and phase by a tap-gain function, $G_i(t)$, and the resulting modulated signals are summed to form the output (received) signal.

The model with equally spaced taps, which has been analyzed by Kailath (1961), is completely general because it can be made to accurately describe any band-limited channel that is stationary or nonstationary in frequency and time. To do this, the adjacent spacings of the taps have to be made equal to the reciprocal of the bandwidth over which the model is accurate, suitable tap-gain functions have to be used to modulate the signals delivered to the taps, and the length of the delay line must be somewhat greater than the differential propagation times of the signal components over the various ray paths in the ionospheric medium.

The model with equally spaced taps could be accurately used as a stationary band-limited model for the ionospheric medium, but it has one practical disadvantage when a bandwidth of 10 kHz is desired, as in the present program. A 10-kHz bandwidth requires adjacent tap spacings of 100 μ s. Since the ionospheric medium can support propagation over several modes with differential propagation times up to 10 ms or more, and a model and simulator that handles these cases is desirable, a total of 100 active taps would be required to accurately represent such

a channel. The task of measuring the ionospheric medium, analyzing the measurements to determine the statistical characteristics of 100 complex tap-gain functions to define the channel model parameters, and subsequently designing and building equipment for synthesizing 100 tap-gain function generators, is a formidable one. While the delay-line model with equally spaced taps is mathematically attractive, it becomes very unattractive from a practical point of view, at least as an ionospheric channel model for bandwidths of 10 kHz.

Fortunately, the ionospheric medium exhibits a characteristic that makes 100 tap-gain functions unnecessary for an accurate 10-kHz model for most channels. Most of the time and over most ionospheric communication links, propagation takes place over relatively few, nearly discrete, modes of propagation: a one-hop path off the E layer (1E mode), a two-hop path off the F layer (2F mode), etc. When a short pulse is transmitted over such a link, several pulses are received, one for each mode, as illustrated by oblique ionograms. It is fairly obvious that it should be possible to make an accurate tapped-delay-line channel model with a limited number of taps (say 3 or 4), as illustrated in figure 1b, provided the tap delays are spaced according to the differential propagation times of the various modes and provided the modes are sufficiently close to being discrete. A received pulse should not be spread or stretched in time relative to the length of the transmitter pulse by more than about $1/(4B)$, where B is the bandwidth in Hertz of the channel being modeled. This restriction will be discussed in more detail later.

For the 10-kHz bandwidth of interest here, the tapped-delay-line model with equally spaced taps in figure 1a was considerably more complicated than the model in figure 1b that has a limited number of

unequally spaced taps. Therefore, the latter model was chosen for the present task. Two facts should be noted, although their investigation is beyond the scope of this report. First, the chosen model of figure 1b can be modified to alleviate the restriction that the time spread on each mode must be less than about $1/(4B)$. If the single tap for any mode with excessive time spread is replaced by a pair of suitably spaced taps, each with its own tap-gain multiplier, the allowable time spread on the mode is increased by a factor of about four. Three or more taps per mode could be used to further increase the allowable time spread. If the process were carried far enough the model would evolve into the model with equally spaced taps shown in figure 1a. Second, if the limited number of taps in the model of figure 1b were spaced equally over the total time spread of a spread-F channel, it would become the model of figure 1a for a limited bandwidth.

The channel models that have been discussed are both general models, because the characteristics of the tap-gain functions, $\{G_i(t)\}$, have not been specified. Any general model might have an infinite variety of specific models based upon it. Before proceeding to section 2.3 for a brief review of specific models that have been used by others and to section 2.4 for a description of the specific model chosen for the present task, we describe in the following section the mathematical functions used to characterize random channels throughout the remainder of the report.

2.2 Channel Characterization

2.2.1 Any Time-Varying Channel

Any time-varying channel, stationary or nonstationary, can be characterized in terms of a number of system functions that relate the output signal to the input signal (Bello, 1963). Two of these system functions are commonly used, the real time-varying impulse response, $h(\tau, t)$, and the complex time-varying frequency response, $H(f, t)$. To

show their relationship to each other, and to the input and output signals in both the time domain and the frequency domain, let the real input signal in time be $x(t)$: then the real output signal in time is obtained from the convolution

$$y(t) = \int_{-\infty}^{\infty} h(\tau, t) x(t-\tau) d\tau, \quad (1)$$

where

$$h(\tau, t) = 0 \text{ when } \tau < 0. \quad (2)$$

If $X(f)$ is the Fourier transform of $x(t)$,

$$x(t-\tau) = \int_{-\infty}^{\infty} X(f) \exp[j2\pi(t-\tau)f] df. \quad (3)$$

Substituting (3) into (1), we have

$$y(t) = \int_{-\infty}^{\infty} df X(f) \exp(j2\pi tf) \int_{-\infty}^{\infty} d\tau h(\tau, t) \exp(-j2\pi f\tau). \quad (4)$$

Now let the second integral in (4) be defined as

$$H(f, t) = \int_{-\infty}^{\infty} h(\tau, t) \exp(-j2\pi f\tau) d\tau. \quad (5)$$

Therefore, $H(f, t)$ is the Fourier transform on τ of $h(\tau, t)$. Substituting (5) in (4) gives

$$y(t) = \int_{-\infty}^{\infty} X(f) H(f, t) \exp(j2\pi tf) df. \quad (6)$$

If $Y(f)$ is defined as the Fourier transform of the output signal, $y(t)$, note that

$$Y(f) \neq X(f) H(f, t); \quad (7)$$

i. e. , the complex amplitude spectrum of the output signal is not equal to the product of the amplitude spectrum of the input signal with the time-varying frequency response of the channel, and the convolution theorem does not hold (Sherman, 1961). The product $X(f) H(f, t)$ is a "time-varying spectrum" and cannot equal the "static spectrum" $Y(f)$. However, $Y(f)$ can be obtained from $X(f)$ and $H(f, t)$ by performing the integration in (6) and then obtaining a Fourier transform of the result.

While both the real impulse response, $h(\tau, t)$, and the complex frequency response, $H(f, t)$, are commonly used to characterize a time-varying channel, we found it more convenient to use $H(f, t)$ or functions derived from it throughout the remainder of this report.

2. 2. 2 Stationary Time-Varying Channels

Since $H(f, t)$ is a random process when it represents time-varying channels, it must be described in statistical terms. Two statistical descriptions of stationary time-varying channels given by Hagfors (1961), Bello (1963), Gallager (1964), and others are the channel correlation function and the channel scatter function.

For a channel stationary in frequency and time, the channel correlation function can be defined as

$$R(\Delta f, \Delta t) = \overline{H^*(f, t) H(f + \Delta f, t + \Delta t)} \quad , \quad (8)$$

where the long bar indicates an average in the frequency-time plane, and the asterisk indicates the complex conjugate of the function. The function $R(\Delta f, \Delta t)$ is not one of frequency, f , or time, t , when $H(f, t)$ is stationary in these variables, but depends only upon the frequency and time displacements, Δf and Δt .

Since fewer independent measurements can be made over the band of interest at one time than can be made in time at any one frequency,

it is convenient to define $R(\Delta f, \Delta t)$ more explicitly as an integral in the time domain,

$$R(\Delta f, \Delta t) = \lim_{t_1 \rightarrow \infty} \frac{1}{t_1} \int_{-t_1/2}^{t_1/2} H^*(f, t) H(f + \Delta f, t + \Delta t) dt \quad (9)$$

The channel scatter function then is defined as the double Fourier transform on Δf and Δt of $R(\Delta f, \Delta t)$,

$$s(\tau, \nu) = \int_{-\infty}^{\infty} \int_{-\infty}^{\infty} R(\Delta f, \Delta t) \exp(j2\pi\tau\Delta f - j2\pi\nu\Delta t) d\Delta f d\Delta t \quad (10)$$

At this point, it is convenient to consider dimensions. A continuing signal expressed as a real function of time has the dimensions of voltage or current. When it is autocorrelated to obtain a correlation function (with unit resistance assumed), and the result is Fourier transformed to obtain a spectrum, the correlation function has the dimensions of power and the spectrum has the dimensions of power per unit frequency (power density). In the preceding equations, $H(f, t)$ is not a signal, but a dimensionless ratio of two amplitude spectrums; consequently, $R(\Delta f, \Delta t)$ is dimensionless. It is convenient, however, to think of it as a power ratio. The channel scatter function, $s(\tau, \nu)$, is also dimensionless, but it is useful to think of it as a power ratio per unit time per unit frequency. It is the ratio of the channel output power per unit time delay, τ , per unit frequency offset, ν , to the channel input power. If the channel scatter function in (10) is integrated over its domain, it is easy to show that

$$\int_{-\infty}^{\infty} \int_{-\infty}^{\infty} s(\tau, \nu) d\tau d\nu = R(0, 0) \quad (11)$$

and $R(0, 0)$ is thus the ratio of the channel output power to the channel input power.

If the ratio of the channel output power to the channel input power is set equal to one to define normalized functions, then the normalized channel correlation function is

$$\bar{R}(\Delta f, \Delta t) = R(\Delta f, \Delta t) / R(0, 0) \quad (12)$$

and the normalized channel scatter functions is

$$\bar{s}(\tau, \nu) = s(\tau, \nu) / R(0, 0) \quad (13)$$

In addition to the previous functions that have been discussed by other authors, some additional functions describing any stationary time varying channels can also be defined. Define the channel time-scatter function as

$$u(\tau) = \int_{-\infty}^{\infty} s(\tau, \nu) d\nu \quad (14)$$

When (10) is substituted in (14), the latter becomes

$$u(\tau) = \int_{-\infty}^{\infty} \int_{-\infty}^{\infty} \int_{-\infty}^{\infty} R(\Delta f, \Delta t) \exp(j2\pi\tau\Delta f - j2\pi\nu\Delta t) d\Delta f d\Delta t d\nu \quad (15)$$

Equation (15) can be integrated with respect to ν and Δt , in turn, to obtain

$$u(\tau) = \int_{-\infty}^{\infty} R(\Delta f, 0) \exp(i2\pi\tau\Delta f) d\Delta f \quad (16)$$

Then

$$u(\tau) = F_{\Delta f}^{-1} \left[R(\Delta f, 0) \right] , \quad (17)$$

where $F_{\Delta f}^{-1}$ means the inverse Fourier transform on Δf . The channel time scatter function, $u(\tau)$, has the dimension of frequency or inverse time and can be viewed as a power ratio per unit time. It is the ratio of the channel output power per unit time delay, τ , to the channel input power.

From (13) and (14), the normalized channel time-scatter function is

$$\bar{u}(\tau) = \int_{-\infty}^{\infty} \bar{s}(\tau, \nu) d\nu = u(\tau) / R(0, 0) . \quad (18)$$

Define the channel frequency-scatter function as

$$v(\nu) = \int_{-\infty}^{\infty} s(\tau, \nu) d\tau . \quad (19)$$

To evaluate (19) for any stationary time-varying channel, substitute (10) in (19) to obtain

$$v(\nu) = \int_{-\infty}^{\infty} \int_{-\infty}^{\infty} \int_{-\infty}^{\infty} R(\Delta f, \Delta t) \exp(-j2\pi\nu\Delta t + j2\pi\tau\Delta f) d\Delta t d\Delta f d\tau . \quad (20)$$

Now integrate (20) with respect to τ and Δf , in turn, to obtain

$$v(\nu) = \int_{-\infty}^{\infty} R(0, \Delta t) \exp(-j2\pi\nu\Delta t) d\Delta t ; \quad (21)$$

consequently,

$$v(\nu) = F_{\Delta t} [R(0, \Delta t)] . \quad (22)$$

The channel frequency-scatter function, $v(\nu)$, has the dimension of time or inverse frequency and can be viewed as a power ratio per unit frequency, i. e., it is the ratio of the channel output power per unit frequency offset, ν , to the channel input power.

From (13) and (19), the normalized channel frequency-scatter function is

$$\bar{v}(\nu) = \int_{-\infty}^{\infty} \bar{s}(\tau, \nu) d\tau = v(\nu)/R(0, 0) . \quad (23)$$

Now define the channel time delay as the first moment of the normalized channel time-scatter function,

$$\hat{\tau} = \int_{-\infty}^{\infty} \tau \bar{u}(\tau) d\tau , \quad (24)$$

which has the dimension of time and is a measure of the average time delay in the channel. To relate the channel time delay to the channel correlation function, substitute (17) in (18) to obtain

$$F_{\Delta f}^{-1} [R(\Delta f, 0)] = R(0, 0) \bar{u}(\tau) . \quad (25)$$

Then (25) can be written as the direct Fourier transform

$$R(\Delta f, 0) = R(0, 0) \int_{-\infty}^{\infty} \bar{u}(\tau) \exp(-j2\pi\Delta f\tau) d\tau . \quad (26)$$

Now substitute (26) in (12) with $\Delta t = 0$ and differentiate the result with respect to Δf to obtain

$$\frac{dR(\Delta f, 0)}{d\Delta f} = -j2\pi \int_{-\infty}^{\infty} \tau \bar{u}(\tau) \exp(-j2\pi\Delta f\tau) d\tau . \quad (27)$$

If (27) is evaluated at $\Delta f = 0$ and combined with (24),

$$\hat{\tau} = \frac{j}{2\pi} \left[\frac{d\bar{R}(\Delta f, 0)}{d\Delta f} \right]_{\Delta f=0} . \quad (28)$$

Now define

$$\angle R(\Delta f, 0) = \tan^{-1} \left\{ \text{Im}[\bar{R}(\Delta f, 0)] / \text{Re}[\bar{R}(\Delta f, 0)] \right\} . \quad (29)$$

It can be shown that $\text{Re}[\bar{R}(\Delta f, 0)]$ is an even function with a derivative of zero at $\Delta f = 0$, providing $\bar{u}(\tau)$, the inverse Fourier transform of $\bar{R}(\Delta f, 0)$, decreases at a rate greater than $1/|\tau|^2$ as $|\tau| \rightarrow \infty$. Under this condition, and since $\text{Im}[\bar{R}(\Delta f, 0)]$ is an odd function with a zero value at $\Delta f = 0$ and $\bar{R}(0, 0) = 1$, (29) can be differentiated with respect to Δf and evaluated at $\Delta f = 0$ to obtain

$$\left[\frac{d\angle \bar{R}(\Delta f, 0)}{d\Delta f} \right]_{\Delta f=0} = -j \left[\frac{d\bar{R}(\Delta f, 0)}{d\Delta f} \right]_{\Delta f=0} . \quad (30)$$

Substitute (30) in (28) then to obtain

$$\hat{\tau} = \frac{-1}{2\pi} \left[\frac{\partial \angle \bar{R}(0, 0)}{\partial \Delta f} \right] . \quad (31)$$

In a similar way, define the channel frequency shift as the first moment of the normalized channel frequency-scatter function,

$$\hat{\nu} = \int_{-\infty}^{\infty} \nu \bar{v}(\nu) d\nu , \quad (32)$$

which has the dimension of frequency and is a measure of the average frequency offset in the channel. Relate the channel frequency shift to

the channel correlation function, in a manner analogous to the development of equations (24) through (31), to obtain

$$\hat{\nu} = \frac{1}{2\pi} \left[\frac{\partial^2 \bar{R}(0, 0)}{\partial \Delta t^2} \right]. \quad (33)$$

Define the channel time spread as two times the square root of the second central moment of the normalized channel time-scatter function,

$$2\rho = 2 \left[\int_{-\infty}^{\infty} (\tau - \hat{\tau})^2 \bar{u}(\tau) d\tau \right]^{\frac{1}{2}}, \quad (34)$$

which has the dimension of time and is a single-number measure of the time-scatter on the channel. To relate it to the channel correlation function, differentiate (27) with respect to Δf and evaluate at $\Delta f = 0$ to obtain

$$\left[\frac{d^2 \bar{R}(\Delta f, 0)}{d\Delta f^2} \right]_{\Delta f=0} = -4\pi^2 \int_{-\infty}^{\infty} \tau^2 \bar{u}(\tau) d\tau. \quad (35)$$

Now square (34), expand the integrand to three terms, and substitute (24), (28), and (35) in the result to obtain

$$(2\rho)^2 = \frac{1}{\pi^2} \left\{ - \frac{d^2 \bar{R}(\Delta f, 0)}{d\Delta f^2} + \left[\frac{d\bar{R}(\Delta f, 0)}{d\Delta f} \right]^2 \right\}_{\Delta f=0}. \quad (36)$$

It can be shown however that the second derivative of the magnitude of $\bar{R}(\Delta f, 0)$ with respect to Δf , at $\Delta f=0$, is

$$\left[\frac{d^2 |\bar{R}(\Delta f, 0)|}{d\Delta f^2} \right]_{\Delta f=0} = \left\{ \frac{d^2 \bar{R}(\Delta f, 0)}{d\Delta f^2} - \left[\frac{d\bar{R}(\Delta f, 0)}{d\Delta f} \right]^2 \right\}_{\Delta f=0}. \quad (37)$$

We can then combine (37) with (36) to obtain

$$2\rho = \frac{1}{\pi} \left[- \frac{\partial^2 |\bar{R}(0, 0)|}{\partial \Delta f^2} \right]^{\frac{1}{2}}. \quad (38)$$

Similarly, define the channel frequency spread as two times the square root of the second central moment of the normalized channel frequency-scatter function,

$$2\sigma \equiv 2 \left[\int_{-\infty}^{\infty} (\nu - \hat{\nu})^2 \bar{\nu}(\nu) d\nu \right]^{\frac{1}{2}}, \quad (39)$$

which has the dimension of frequency and is a single-number measure of the frequency-scatter on the channel. Relate it to the channel correlation function, in a manner that is analogous to the development of equations (34) through (38), to obtain

$$2\sigma = \frac{1}{\pi} \left[- \frac{\partial^2 |\bar{R}(0, 0)|}{\partial \Delta t^2} \right]^{\frac{1}{2}}. \quad (40)$$

2.2.3 General Stationary Model

All of the preceding equations apply for any stationary time-varying channel. To describe the general stationary tapped-delay-line model with unequally spaced taps (fig. 1b), let us modify them to more explicit forms. We see that the complex time-varying frequency response of this model is

$$H(f, t) = \sum_{i=1}^n G_i(t) \exp(-j2\pi\tau_i f), \quad (41)$$

where "i" is an integer that numbers the tap or path, τ_i is the time delay on the i-th path, and "n" is the total number of paths. Each exponential function defines the time delay of a path and is a function of frequency only, since it does not change with time. Each tap-gain function, $G_i(t)$, is a complex function that is constant in frequency but varies in time; i. e., each tap-gain function varies the amplitude and phase of each spectral component of the delayed signal at its tap by the same amount continuously with time.

Equation (41) can be substituted in (9) to obtain the channel correlation function for the general stationary model of figure 1b,

$$R(\Delta f, \Delta t) = \lim_{t_1 \rightarrow \infty} \frac{1}{t_1} \int_{-t_1/2}^{t_1/2} \sum_{i=1}^n \sum_{\ell=1}^n G_i^*(t) G_\ell(t + \Delta t) \exp[j2\pi(\tau_\ell - \tau_i)f - j2\pi\tau_i\Delta f] dt. \quad (42)$$

The order of integration and summation can be changed to give

$$R(\Delta f, \Delta t) = \sum_{i=1}^n \exp(-j2\pi\tau_i\Delta f) \sum_{\ell=1}^n \exp[j2\pi(\tau_\ell - \tau_i)f] \lim_{t_1 \rightarrow \infty} \frac{1}{t_1} \int_{-t_1/2}^{t_1/2} G_\ell^*(t) G_\ell(t + \Delta t) dt. \quad (43)$$

Now assume that the crosscorrelations between all pairs of tap-gain functions are zero. For such cases, where $i \neq \ell$, the crosscorrelation integral in (43) is zero. For the terms where $i = \ell$, the exponential function preceding the integral becomes one. Then (43) becomes

$$R(\Delta f, \Delta t) = \sum_{i=1}^n \exp(-j2\pi\tau_i\Delta f) \lim_{t_1 \rightarrow \infty} \frac{1}{t_1} \int_{-t_1/2}^{t_1/2} G_i^*(t) G_i(t + \Delta t) dt. \quad (44)$$

Because of its form, the integral in (44) is conveniently defined as the tap-gain correlation function,

$$C_i(\Delta t) = \lim_{t_1 \rightarrow \infty} \frac{1}{t_1} \int_{-t_1/2}^{t_1/2} G_i^*(t) G_i(t + \Delta t) dt, \quad (45)$$

which differs from the one given by Gallager (1964). The latter function is the single Fourier transform on Δf of $R(\Delta f, \Delta t)$ and a continuous function of τ and Δt . It is applicable to a model with a large number of equally spaced taps as the number of taps approaches infinity. The definition in (45) is more useful for models with a finite number of spaced taps.

Like $R(\Delta f, \Delta t)$, $C_i(\Delta t)$ is dimensionless, but it can also be viewed as a power ratio with $C_i(0)$ the ratio of the i -th path output power to the channel input power. The normalized tap-gain correlation function is defined as

$$\bar{C}_i(\Delta t) = C_i(\Delta t)/C_i(0) . \quad (46)$$

To continue with $R(\Delta f, \Delta t)$, when (45) is substituted in (44), the channel correlation function for the general stationary model of figure 1b becomes

$$R(\Delta f, \Delta t) = \sum_{i=1}^n \exp(-j2\pi\tau_i\Delta f) C_i(\Delta t) . \quad (47)$$

The normalized channel correlation function, $\bar{R}(\Delta f, \Delta t)$, can be obtained by substituting (47) into (12).

For the general stationary model of figure 1b, define the tap-gain spectrum for the i -th path as the Fourier transform of the tap-gain correlation function for the i -th path,

$$v_i(\nu) = \int_{-\infty}^{\infty} C_i(\Delta t) \exp(-j2\pi\nu\Delta t) d\Delta t . \quad (48)$$

The function $v_i(\nu)$ has the dimension of time or inverse frequency and can be viewed as a power ratio per unit frequency. It is the ratio of the i -th path output power per unit frequency offset, ν , to the channel input power. The normalized tap-gain spectrum, corresponding to the normalized tap-gain correlation function, is

$$\bar{v}_i(\nu) = v_i(\nu)/C_i(0) . \quad (49)$$

To obtain the channel scatter function for the general stationary channel model of figure 1b, substitute (47) in (10) to obtain

$$s(\tau, \nu) = \sum_{i=1}^n \int_{-\infty}^{\infty} d\Delta f \exp[j2\pi(\tau - \tau_i)\Delta f] \int_{-\infty}^{\infty} d\Delta t C_i(\Delta t) \exp(-j2\pi\nu\Delta t) . \quad (50)$$

Equation (48) can be substituted in (50) and the remaining integration performed to obtain

$$s(\tau, \nu) = \sum_{i=1}^n \delta(\tau - \tau_i) v_i(\nu) . \quad (51)$$

The normalized channel scatter function, $\bar{s}(\tau, \nu)$, for the general stationary channel model (fig. 1b) can be obtained by substituting (51) in (13).

The channel time-scatter function for figure 1b is obtained when (47), at $\Delta t = 0$, is substituted in (16) and the integration performed to give

$$u(\tau) = \sum_{i=1}^n C_i(0) \delta(\tau - \tau_i) . \quad (52)$$

The normalized channel time-scatter function is obtained by substituting (52) in (18).

The channel frequency-scatter function for the general stationary channel model of figure 1b is obtained when, at $\Delta f = 0$, we substitute (47) in (21) and then (48) into the result:

$$v(\nu) = \sum_{i=1}^n v_i(\nu) . \quad (53)$$

Substituting (53) in (23) yields the normalized channel frequency-scatter function.

We can obtain the channel time delay for the general stationary model of figure 1b by substituting (52) in (18) and the result in (24). When the integration is performed, the resulting channel time delay is

$$\hat{\tau} = [1/R(0, 0)] \sum_{i=1}^n C_i(0) \tau_i . \quad (54)$$

To specify the channel frequency shift, define for each path the tap-gain frequency shift as the first moment of the normalized tap-gain spectrum,

$$\nu_i = \int_{-\infty}^{\infty} \nu v_i(\nu) d\nu , \quad (55)$$

which has the dimension of frequency and is a measure of the average frequency offset on the path. For each path, the tap-gain frequency shift is related to the tap-gain correlation function by

$$\nu_i = \frac{1}{2\pi} \left[\frac{d\bar{\phi} C_i(0)}{d\Delta t} \right] . \quad (56)$$

It follows that the channel frequency shift is

$$\hat{\nu} = [1/R(0, 0)] \sum_{i=1}^n C_i(0) \nu_i . \quad (57)$$

The channel time spread for the general stationary tapped-delay-line model (fig. 1b) can be written directly as two times the square root of the difference between the second moment of the normalized channel time-scatter function, (52) divided by $R(0, 0)$, and the square of its first moment, the channel time delay,

$$2\rho = 2 \left\{ [1/R(0, 0)] \left[\sum_{i=1}^n C_i(0) \tau_i^2 \right] - \hat{\tau}^2 \right\}^{\frac{1}{2}} . \quad (58)$$

To specify the channel frequency spread, define for each path the tap-gain frequency spread as two times the square root of the second central moment of the normalized tap-gain spectrum,

$$2\sigma_1 = 2 \left\{ \int_{-\infty}^{\infty} (\nu - \nu_1)^2 \bar{v}_1(\nu) d\nu \right\}^{\frac{1}{2}}, \quad (59)$$

which has the dimension of frequency and is a single-number measure of the frequency scatter on the path. For each path, we can relate the tap-gain frequency spread to the tap-gain correlation function by analogy to (39) and (40) to obtain

$$2\sigma_1 = \frac{1}{\pi} \left[\frac{-d^2 |\bar{C}_1(0)|}{d\Delta t^2} \right]^{\frac{1}{2}}. \quad (60)$$

The channel frequency spread then can be written as two times the square root of the difference between the second moment of the normalized channel frequency-scatter function and the square of its first moment,

$$2\sigma = 2 \left\{ \sum_{i=1}^n [C_i(0)/R(0,0)] (\nu_i^2 + \sigma_i^2) - \left[\sum_{i=1}^n [C_i(0)/R(0,0)] \nu_i \right]^2 \right\}^{\frac{1}{2}}. \quad (61)$$

The first summation in (61) is the second moment of the normalized channel frequency-scatter function and is the sum of the weighted second moments of the tap-gain spectrums in terms of their frequency shifts and frequency spreads. The second summation in (61) is the corresponding first moment.

2.3 Specific Models

Specific channel models that have been used by others for the design and construction of ionospheric channel simulators, with only one known exception, have been based on the general bandlimited stationary model shown in figure 1b. The single exception (Goldberg et al., 1965) used 50 taps equally spaced over a 5.0-ms delay line (see fig. 1a), where the bandlimited simulator was nonstationary. Actually, it was not a simulator, if the definition of a simulator requires that all functions be

synthesized, because tape recordings of ionospheric signals were used to supply the tap-gain functions. It could more properly be called an ionospheric reproducer or, as described by the authors, a stored ionosphere.

The other ionospheric simulators used a considerable variety of specific models. The earliest simulator (Bray et al., 1947) provided three paths with delay adjustments from zero to 2.0 ms in 30- μ s steps. One tap-gain function was a real constant; the other two were complex and provided independent linear phase modulation that produced different fixed frequency shifts in the signal over these two paths. This is illustrated in figure 2a, where the tap-gain spectrum (the Fourier transform of the tap-gain correlation function) for the second or third path, $v_i(v)$, is shown qualitatively. The linear phase modulation results in a single Dirac delta function of v whose shift from zero is adjustable, as indicated by the horizontal arrows. Since this model, as well as all others to be described in figure 2, had individually adjustable path gains, an ability to adjust the magnitude of the tap-gain spectrum is not indicated or described.

Another early simulator (Ross and Meyer, 1948) provided two paths with delay adjustments from zero to 3.0 ms in 100- μ s steps. The tap-gain function for one path was a real constant, with a resulting tap-gain spectrum consisting of a single delta function with zero shift. The second tap-gain function was a complex constant with a manually adjustable phase that, after being set, had the same tap-gain spectrum, as shown in figure 2b.

Law et al. (1957) extended the earlier work of Bray et al. (1947) to develop a three-path simulator with delay adjustments from zero to 2.0 ms in 30- μ s steps. The tap-gain function for each of the three paths consisted of two independent complex linear-phase-modulation terms;

when two paths were used, each tap-gain function had three independent linear-phase-modulation terms. The corresponding tap-gain spectrums consisted of either two or three delta functions with adjustable shifts (fig. 2c).

Freudberg (1965) developed a channel simulator having five paths with adjustable delays up to 3.0 ms. Each tap-gain function was a complex bivariate Gaussian random function with a zero mean value and independent quadrature components with equal RMS values. Consequently, each tap-gain function had a Rayleigh amplitude distribution and a uniform phase distribution. The tap-gain spectrum for any path is illustrated in figure 2d. No provision was made for frequency shifts of the spectrum. Here, as in all the illustrations in figure 2, a dashed rectangle illustrates a spread spectrum when the shape of the spectrum is undefined.

Walker (1965) developed a simulator with eight paths with delay adjustments from zero to 5.0 ms in 40- μ s steps. Each pseudo-random tap-gain function was real with a Gaussian amplitude distribution and provided amplitude modulation only (fig. 2e). No provision was made for frequency shifts of the spectrum.

In Clarke's (1965) water-tank simulator, a specular signal component was produced by reflection of the sound wave from a metal rod, and scatter components were produced by ascending air bubbles. The complex tap-gain function for the combination was a constant plus a base-band bivariate Gaussian random function with quadrature components with equal RMS values. In the tap-gain spectrum (fig. 2f), the delta function for the specular component corresponds to the constant term in the tap-gain function. The spectrum could not be shifted. While the simulator was not strictly a path of discrete delay, it presumably was approximately so. Movement of the rod behind the bubble stream was used to reduce the specular component and control the resulting

Nakagami-Rice amplitude distribution (Nakagami, 1940; Rice, 1944) of the tap-gain function. The tap-gain spectrum could be controlled to some degree by adjustment of the bubble size and, while several measurements of the tap-gain spectrum were obtained, no attempt has been made to illustrate them in figure 2f.

Zimmerman and Horwitz (1967) developed a simulator with three paths with delay adjustments from zero to 10 ms in 500- μ s steps. A choice of several complex tap-gain functions was provided: linear phase modulation corresponding to the frequency-shifted delta function in figure 2g, sinusoidal frequency modulation (not shown), a transient frequency shift (also not shown), and a constant plus a baseband bivariate Gaussian random function with a zero mean value and independent quadrature components with equal RMS values shown in figure 2g. With the exception of the spectrum for the linear phase modulation, none of the tap-gain spectrums could be shifted.

A simulator developed by Klein (1968) provided five paths with delay adjustments from zero to 21.3 ms in 20.8- μ s steps. Each complex tap-gain function contained a constant plus a baseband bivariate Gaussian random function with a zero mean value and independent quadrature components with equal RMS values. An adjustable linear phase-modulation factor was included in the tap-gain function to produce a frequency shift of the total tap-gain spectrum (fig. 2h).

2.4 Chosen Model

While the choice of the general model of figure 1b was relatively easy, the best choice of specifications for the tap-gain functions and their spectrums was less so. Over the years, many measurements of the ionosphere have indicated that ionospheric signals suffer Rayleigh fading. However, most of these measurements were made without

adequate knowledge of the number of modes or paths present. Near-Rayleigh fading of a multihop signal may be expected even if the fading of the signal on each hop is not Rayleigh. A commonly held view of a one-hop signal is that it consists of a constant-amplitude component plus a Rayleigh-fading scatter component that results in a composite Nakagami-Rice amplitude distribution. However, measurements by Balser and Smith (1962) on individual one-hop modes showed that the majority produced Rayleigh fading, and this is substantiated by measurements of Boys (1968). While there is evidence that significant constant amplitude components may exist in high rays (Balser and Smith, 1962), the low probability of receiving high rays implies that significant constant amplitude components would rarely be seen.

We believed, therefore, that the best choice for tap-gain functions in the specific channel model would be independent baseband complex bivariate Gaussian random functions with zero mean values and quadrature components with equal RMS values, so that signals on each path in the model would have independent fading with a Rayleigh amplitude distribution and a uniform phase distribution. As shown in section 5, this specification for the tap-gain functions was valid for the measured channels.

In addition to deciding that the tap-gain functions would have a Rayleigh amplitude distribution and a uniform phase distribution, the spectrums of the tap-gain functions had to be specified. Since the ionosphere can introduce frequency shifts on signals, as well as fading that results in frequency spreads, such shifts had to be included in the tap-gain spectrums. Also, two magnetoionic components of a mode can produce different frequency shifts, and the difference of the two shifts can at times be greater than the frequency spreads of the magnetoionic components (Davies, 1962). We therefore decided that the tap-gain spectrums,

in general, would need two components--one for each magnetoionic component. It was also necessary to specify the shapes of the tap-gain spectrum for the two magnetoionic components, since it is known that these shapes can have a considerable influence on the distortion characteristics of a channel. Bello and Nelin (1962) did a theoretical analysis on the performance of digital communication systems for a single-path Rayleigh-fading channel with two different tap-gain correlation functions, an exponential and a Gaussian. The corresponding tap-gain spectrums were a single-pole-filter spectrum of the form $1/(1 + \zeta_1 v^2)$ and a Gaussian spectrum of the form $\exp(-\zeta_2 v^2)$, respectively. For constants ζ_1 and ζ_2 that gave equal half-power spectrum bandwidths, they showed that the single-pole-filter spectrum gave substantially greater signal distortion and higher probability of error than did the Gaussian spectrum. This is not unexpected, since the skirts on the single-pole-filter spectrum decay much less rapidly than the skirts on the Gaussian spectrum. The selection of the correct specification for the shapes of the magnetoionic components of the tap-gain spectrums therefore was quite important. Because data were not available on the spectrum shapes of typical magnetoionic components, we decided rather arbitrarily to specify that the shape of the tap-gain spectrum for each of the two magnetoionic components would be Gaussian. If subsequent measurements and analyses showed this choice to be invalid, a more suitable second choice could be made, but as section 5. shows, our choice was a good one and did not need revision.

To be explicit, the specific channel model that we selected had independent tap-gain functions, each of which is defined by

$$G_{si}(t) = G'_{sia}(t) \exp(j2\pi\nu_{sia} t) + G'_{sib}(t) \exp(j2\pi\nu_{sib} t) , \quad (62)$$

where the "s" subscripts designate quantities for the statistical channel model (as opposed to measured or other quantities to be described later), the "i" subscripts denote the path number, and the "a" and "b" subscripts identify the magnetoionic components. $G'_{sia}(t)$ and $G'_{sib}(t)$ are sample functions of two independent complex Gaussian stationary ergodic random processes, each with zero mean values and independent quadrature components with equal RMS values. Specifically, if $G'_{sia}(t)$ is defined in terms of its real and imaginary components by

$$G'_{sia}(t) = \underline{g}'_{sia}(t) + j \underline{g}'_{sia}(t), \quad (63)$$

then \underline{g}'_{sia} and \underline{g}'_{sib} have a joint probability density function

$$P(\underline{g}'_{sia}, \underline{g}'_{sib}) = \frac{1}{\pi C_{sia}(0)} \exp \left[- \frac{\underline{g}'_{sia}{}^2 + \underline{g}'_{sib}{}^2}{C_{sia}(0)} \right], \quad (64)$$

where $C_{sia}(0)$ is the autocorrelation function of $G'_{sia}(t) \exp(j2\pi \nu_{sia} t)$ at zero displacement ($\Delta t = 0$) and specifies the ratio of the channel output power delivered by the magnetoionic component to the channel input power. With a suitable change in the "a" subscripts, (63) and (64) also apply to $G'_{sib}(t)$.

To explain the exponential factors in (62), consider $E[G'_{sia}^*(t) G'_{sia}(t + \Delta t)]$. When this autocorrelation function is computed in terms of the real and imaginary components in (63), the cross products will have zero averages because the real and imaginary components are independent. The resulting correlation function will be real and have even symmetry about $\Delta t = 0$. Its Fourier transform, the spectrum of $G'_{sia}(t)$, must then have even symmetry about $\nu = 0$. The same is true for $G'_{sib}(t)$, and the primes in (62), (63), and (64) indicate the functions have spectrums with even symmetry about $\nu = 0$. Therefore, the exponential factors in (62) were

incorporated to provide the desired frequency shifts, ν_{s1a} and ν_{s1b} , for the magnetoionic components in the tap-gain spectrum.

The tap-gain correlation function corresponding to (62) is

$$C_{s1}(\Delta t) = \left\{ \begin{aligned} &C_{s1a}(0) \exp[-2\pi^2 \sigma_{s1a}^2 (\Delta t)^2 + j2\pi \nu_{s1a} \Delta t] \\ &+ C_{s1b}(0) \exp[-2\pi^2 \sigma_{s1b}^2 (\Delta t)^2 + j2\pi \nu_{s1b} \Delta t] \end{aligned} \right\}, \quad (65)$$

and the tap-gain spectrum is

$$v_{s1}(\nu) = \left\{ \begin{aligned} &[C_{s1a}(0)/(2\pi\sigma_{s1a}^2)^{\frac{1}{2}}] \exp[-(\nu - \nu_{s1a})^2/(2\sigma_{s1a}^2)] \\ &+ [C_{s1b}(0)/(2\pi\sigma_{s1b}^2)^{\frac{1}{2}}] \exp[-(\nu - \nu_{s1b})^2/(2\sigma_{s1b}^2)] \end{aligned} \right\}, \quad (66)$$

where

$$C_{s1}(0) = C_{s1a}(0) + C_{s1b}(0), \quad (67)$$

and σ_{s1a} and σ_{s1b} are the standard deviations of the two Gaussian components of the spectrum. A graphical representation of a tap-gain spectrum is shown in figure 3a. In general, the two Gaussian components in a tap-gain spectrum have different power ratios, frequency shifts, and frequency spreads. There are times, however, when the shifts and spreads of the two magnetoionic components in an ionospheric channel are approximately equal, when the two components are effectively one. For these times, $C_{s1b}(0)$ becomes zero in (62) and (65) through (67), and the "a" subscript is dropped, causing the tap-gain spectrum to appear as in figure 3b.

Throughout the remainder of the report, the term statistical channel model designates the specific channel model defined by figure 1b and equations (62) through (67) above. The term bivariate Gaussian hypothesis refers to the assumption that each tap-gain function in this model is a

complex bivariate Gaussian random function with a zero mean value and quadrature components with equal RMS values, as defined by (62) through (64). The term independence hypothesis refers to the assumption that the tap-gain functions are independent, and the term Gaussian spectrum hypothesis refers to the assumption that each tap-gain spectrum in the model in general consists of the sum of two Gaussian functions with different power ratios, frequency shifts, and frequency spreads, as defined by (66) and (67).

3. MEASURING TECHNIQUE

3.1 Method

To experimentally confirm the validity and accuracy of the proposed statistical channel model, we needed specifically designed measurements and analyses to test:

- (a) The validity of the bivariate Gaussian hypothesis for each path in the statistical channel model,
- (b) The validity of the independence hypothesis.
- (c) The validity of the Gaussian spectrum hypothesis.
- (d) The bandwidth limitation on the statistical channel model imposed by ionospheric paths with nonzero time spreads; i. e., the accuracy of the statistical channel model.

One might attempt these tests by comparing statistical characteristics of the statistical channel model with corresponding characteristics of the measured ionospheric channel. Let the subscript "m" be used to designate quantities in the measured ionospheric channel. One might choose the parameters for each of the paths in the statistical channel (time delays, power ratios, frequency shifts, and frequency spreads) so

that $R_s(\Delta f, \Delta t)$ was a best fit to $R_m(\Delta f, \Delta t)$ and use the accuracy of the fit on the Δf axis to check (d) and on the Δt axis to check (c). The amplitude and phase distributions of $H_m(f, t)$ could be examined to see if they were Rayleigh and uniform, respectively, as a check on (a). However, this method would have serious limitations: it would not be possible to test (b) and the accuracy of the test on (c) would suffer when several paths existed because the individual tap-gain correlation functions in (47) would be masked by each other; in the test on (a), near-Rayleigh fading and uniform phase distributions for $H_m(f, t)$ might easily be obtained when several paths exist, even though one or more of the individual ionospheric paths did not exhibit Rayleigh fading and a uniform phase distribution.

It can be seen that better tests could be made if the time-varying characteristics of each ionospheric mode were available. Each $G_{m1}(t)$ could be examined to test (a) and they could be crosscorrelated to test (b). The optimum tap-gain spectrums could be obtained by fitting their inverse Fourier transforms, $C_{s1}(\Delta t)$, to $C_{m1}(\Delta t)$ to satisfy (c), and $R_s(\Delta f, 0)$ could be compared to $R_m(\Delta f, 0)$ to test (d). Unfortunately, it is not possible to do this because $\{G_{m1}(t)\}$ do not exist. Since each path in the ionospheric channel always has some nonzero time spread (even though it might be quite small), the time-varying response on each path is a function of frequency, f , as well as time, t . However, the statistical model in figure 1b has discrete paths whose tap-gain functions are independent of frequency. To fit and test each path in the statistical model by comparing it with the corresponding path in the ionospheric channel requires that the fit and comparison be made to an approximation of the ionospheric path response that is independent of frequency. This is not a serious limitation, however, if the fits are made at one frequency or over a band that is much smaller than the reciprocal of the time spread on the mode, in which the ionospheric path response is nearly constant

with frequency. The fact that the fit is restricted to some bandwidth does not restrict the subsequent testing of (c) to the same bandwidth; it can be made over any band.

If the measured response of each path in the ionosphere is approximated by a function that is constant with frequency, the set of these functions define a deterministic channel model with discrete paths. Because the paths are discrete, the deterministic channel model has the same form as the statistical channel model in figure 1b, and both are specified by (41). Since $\{G_{d1}(t)\}$ are those deterministic tap-gain functions that make $H_d(f, t)$ an accurate deterministic approximation of $H_m(f, t)$ (for a sufficiently small bandwidth), $\{G_{d1}(t)\}$ may be analyzed to test (a) and (b). For each path, the statistical channel parameters can be selected to obtain a best fit between $C_{s1}(\Delta t)$ and $C_{d1}(\Delta t)$ (or the corresponding tap-gain spectrums), and the accuracy of the fit used to test (c). The method of testing (d) can vary according to the measuring technique.

We examined three measuring techniques which might be used to obtain the data required to specify the deterministic channel and test the validity and accuracy of the statistical channel model:

(A) Time-domain measurements. An accurate reference sinusoid would be amplitude modulated to obtain coherent pulses ($\sim 50 \mu s$) with Gaussian envelopes that would be transmitted at a regular rate (~ 200 Hz) less than the reciprocal of the expected differences in the propagation times of the modes but greater than the maximum frequency shifts and spreads that might be expected on the modes. The pulses received over each mode would be separated by a time gate and the spectral component at the "carrier" (reference) frequency, f_c , would be separated with a narrowband filter (~ 20 Hz wide). The filtered CW signal would be measured against an accurate local reference to obtain $G_{d1}(t) \exp(-j2\pi f_c \tau_1)$.

Since τ_i would be known from the gate delay setting, the exponential factor could be removed to leave $G_{di}(t)$, which could be analyzed to test (a), (b), and (c). For each mode, two or more additional narrowband filters would be used to obtain similar measurements on spectral components of the gated received pulses near the edges of the pulse spectrum (~ 10 kHz wide). The resulting functions could be crosscorrelated with each other and the "carrier" function to test (d).

(B) Frequency-domain measurements. A number of CW signals with equal amplitudes and equal adjacent spacings over a 10-kHz band could be generated from a common accurate reference and transmitted. Each received CW signal would be separately filtered with a narrowband filter (~ 20 Hz wide) and compared against an accurate local reference to obtain $H_{\pi}(f_k, t)$, the time-varying frequency response of the ionospheric medium at the frequencies of the transmitted signals. The subscript "k" is an integer that numbers the transmitted signals. Now let a preliminary deterministic channel be specified by

$$H_{\pi}(f_k, t) = \sum_{i=1}^n G_{di}''(t) \exp[-j2\pi\tau_i''(t) f_k] , \quad (68)$$

where $\tau_i''(t)$ can vary with time. Equation (68) represents one equation for each frequency of measurement, f_k . The equations are nonlinear in the unknown quantities, $G_{di}''(t)$ and $\tau_i''(t)$. If $2n$ or more frequencies of measurement are used, the set can be solved simultaneously at any time, t , by Prony's method (Hildebrand, 1956). If sets of solutions are obtained repeatedly at a regular rate greater than the maximum frequency shift and frequency spread of the modes, the resulting solutions are time-sampled versions of the desired solutions. For each path, the time-varying solutions for $\tau_i''(t)$ could be averaged to obtain a constant τ_i . Then for each frequency of measurement, f_k , numerical values of

$H_m(f_k, t)$, $\{\tau_i\}$, and f_k could be used in

$$H_m(f_k, t) = \sum_{i=1}^n G_{d,i}(t) \exp(-j2\pi\tau_i f_k) \quad (69)$$

to form a set of equations, one equation for each f_k . The set of linear equations could be solved repeatedly at equally spaced times to obtain solutions for $\{G_{d,i}(t)\}$. The latter solutions for the tap-gain functions in the deterministic channel model could be analyzed to test (a), (b), and (c). For each path, $G_{d,i}(t)$ could be autocorrelated at $\Delta t = 0$ to obtain $C_{d,i}(0)$. Then $\{C_{d,i}(0)\}$ and $\{\tau_i\}$ could be used in (47) to obtain $R_d(\Delta f, 0)$. The parameters of the statistical channel model, which would be obtained in testing (c), could be used to compute $R_s(\Delta f, 0)$ which could be compared with $R_d(\Delta f, 0)$ to test (d).

(C) Hybrid time- and frequency-domain measurements. An accurate reference would be amplitude modulated to obtain coherent pulses ($\sim 50 \mu s$) with Gaussian envelopes at a regular rate (~ 200 Hz). The same reference also would be used to generate a number of CW signals of equal amplitudes with unequal adjacent frequency spacings that were integral multiples of the pulse rate. The frequencies of the CW signals would coincide with the frequencies of some of the spectral components of the pulses, but would be considerably larger in amplitude. The phase-locked pulses and CW signals would be added and transmitted. At the receiver, a multiple-notch filter would remove the strong CW signals from the pulse spectrum. The remaining slightly distorted pulse signal would be envelope detected and compared with an accurate local reference to measure $\{\tau_i\}$, the time-delays of the modes. Each of the strong CW signals would be separated in a narrowband filter (~ 20 Hz wide) and compared against the local reference to obtain $H_m(f_k, t)$ at each of the frequencies of measurement. Then $\{\tau_i\}$ and $H_m(f_k, t)$ could be used in (66) to form a

set of linear equations that could be solved simultaneously at equally spaced times to obtain solutions for $\{G_{d1}(t)\}$. The latter solutions for the tap-gain functions in the deterministic channel model and the time delays, $\{\tau_1\}$, could then be used as in method (B) to test (a), (b), and (c).

In selecting one of the three methods, (A), (B), or (C), we weighed their relative advantages and disadvantages. All three would require very accurate references at the transmitter and receiver. Since a spectrum resolution of 10^{-3} Hz or less was desired, measurements at an HF frequency of about 10^7 Hz would require reference accuracies of 1×10^{-10} or better. The equipment complexity and specifications on accuracy and stability were also comparable, and no one of the three methods was particularly advantageous in these respects. Their capabilities on measured signal-to-noise ratios however did differ significantly. Without going into the details of the calculations, we estimated that methods (B) and (C) had signal-to-noise ratio advantages over method (A) of about 8 dB and 11 dB, respectively. Methods (B) and (C) would require repeated solutions of simultaneous equations demanding additional computer time, but the added computer costs would be negligible.

When methods (B) and (C) were compared, we found that method (C) would be advantageous because half as many CW signals would be required for a given number of modes. More important, in method (C) the CW signals do not have to be equally spaced in frequency, allowing a greater number of difference frequencies between the various pairs of CW signal frequencies and allowing the channel correlation functions, $R_e(\Delta f, \Delta t)$ and $R_d(\Delta f, \Delta t)$, to be computed at more values of Δf . Also, if the smallest adjacent spacing of the unequally spaced tones is less than the reciprocal maximum differential propagation times of the modes, no ill-conditioned coefficient matrices can occur in the simultaneous solutions. In method

(B), an ill-conditioned matrix occurs when the uniform adjacent spacings of the tones are equal to an integral multiple of the reciprocal of the differential propagation times of any pair of modes.

Because we believed method (C) to be superior to methods (A) and (B), all factors considered, we selected this hybrid time- and frequency-domain method of measuring ionospheric channels.

3.2 Equipment

With the choice of the hybrid time- and frequency-domain method of making ionospheric channel measurements, selection of the pulse duration and recurrence rate and the number, frequency spacings, and phasings of the tones became necessary. Because two 12-kHz channel assignments were available, the Gaussian transmitter pulse duration was set at 53 μ s between the - 4.35-dB points on the pulse envelope, corresponding to the \pm one-sigma time values. The resulting transmitter pulse spectrum was 12 kHz wide at the - 4.35-dB values of the Gaussian spectrum. A pulse rate of 200 Hz was selected, which allowed 5.0 ms between successive pulses, more than the expected differential propagation times of the modes. While it was desirable to use as many tones as possible to maximize the detail in the measurements, the complexity of the equipment increased with the number of tones, and a practical compromise was required. Because each of the received tones had to be tape recorded at a low intermediate frequency (IF), and a 14-track analog tape recorder was available, 11 tones were used. Two of the three remaining tracks were used for reference signals and the third for the detected received pulses.

In selecting the frequencies and phases of the 11 tones, we imposed several restrictions:

- (a) The tone frequencies each had to coincide with a spectral component of the pulses; i. e., be spaced at an integral multiple of 200 Hz from the carrier frequency, f_c .
- (b) The amplitude spectrum of the 11 tones must be symmetrical about the carrier to simplify the generating process.
- (c) Adjacent spacings of the tones should be lowest near the center of the band and greatest toward the edges of the band. If poor fits of $H_d(f, t)$ to $H_m(f, t)$ occurred when all 11 tones were used, because of excessive time spread on the modes, fits at reduced bandwidths with fewer tones could be accomplished with a minimum sacrifice in the number of tones used.
- (d) Consistent with requirement (c), tone spacings should be chosen to maximize the number of different frequency spacings, when all combinations of the tones taken two at a time were considered.
- (e) The phasing of each tone relative to the central carrier tone should be restricted to plus and minus cosine functions, measured relative to the peaks of the pulses, so that intermodulation products generated in the slightly nonlinear transmitter would either be in phase or π radians out of phase with respect to the desired tones. This restriction was imposed to minimize phase distortion of the multiple-tone spectrum.
- (f) Tone and pulse phasings should be chosen, consistent with (e), to maximize the average-to-peak power ratio.

When all the above requirements were considered and an optimum selection was made, the power spectrum of the combined pulse and tone signals was that in figure 4a, where the power levels of the spectral components are shown relative to the peak power of the composite signal.

The tone frequencies relative to the central carrier tone are 0, ± 0.2 , ± 1.0 , ± 1.6 , ± 3.2 , and ± 4.8 kHz. If $k = 1, 2, 3, \dots, 11$ are the numbers designating the 11 tones from the lowest to the highest frequency, then all were plus cosine functions except tones 3 and 9, which were minus cosine functions. The pulse was also a minus cosine function with a peak power about 6 dB greater than the peak power of the composite waveform. Figure 4b is a photograph of an oscilloscope display of the total composite transmitter signal as a function of time; the transmitter pulse occurs at $t = 0$ and 5 ms.

Figure 5 is a block diagram of the transmitting equipment. A cesium-beam frequency standard with an accuracy of about 1×10^{-11} drove a specially built reference chassis that divided the 1-MHz reference frequency to develop three accurate pulse trains with recurrence rates of 0.2, 0.2, and 1.6 kHz. The first of the two 0.2-kHz pulse trains drove two bandpass filters centered at 0.2 and 1.0 kHz, each of which separated a spectral component at its center frequency. Each filter delivered a cosine function with adjustable amplitude and phase. The 1.6-kHz pulse train was used to generate adjustable cosine functions at 1.6, 3.2, and 4.8 kHz in a similar manner. The second 0.2-kHz pulse train drove a baseband seven-pole filter that delivered negative near-Gaussian pulses of adjustable amplitude at a 0.2-kHz rate. The timing of the first 0.2-kHz and the 1.6-kHz pulse trains were delayed from that of the second 0.2-kHz pulse train by an adjustable amount, so that the baseband Gaussian pulse could be synchronized with the concurrent peaking of the five baseband cosine functions. The pulse signal and four of the five baseband cosine signals were summed with a DC signal for the carrier tone at one input of an operational amplifier. The 1.6-kHz cosine function drove the other input, which provided summing with a phase reversal. The summed baseband signals then drove a multiplier (double-balanced

modulator), which was also driven by a signal at the RF carrier frequency. The cesium-beam standard drove a frequency synthesizer that delivered either of the two required carrier frequencies. The product of the baseband and carrier signals was the desired composite RF signal.

After initial adjustment of the pulse timing and the tone amplitudes, no additional calibrations of this type were necessary. Periodic calibrations of the tone phasings was done by switching on successively larger numbers of tones. For each combination, a phase adjustment was made to the last tone added to obtain the required time symmetry in the envelope of the composite RF signal as a function of time. It is estimated that the error components in each tone were at least 30 dB below the magnitudes of the tones.

The composite output signal from the multiplier drove two cascaded untuned linear distributed amplifiers. These in turn were followed by a two-stage 500-W linear amplifier and a high-power (FRT-22) linear transmitter. However, the expected 50-kW peak power was not available during the ionospheric channel measurements because of a defective component in the final amplifier that could not be replaced in time for the measurements. The peak power of the signal delivered to the antenna during the measurements was about 5 kW.

The antennas at the transmitting and receiving sites were identical, except that the transmitting antenna could handle greater power. Both were sloping-V antennas whose specifications were selected to obtain a main lobe with a vertical angular width as large as practical for the two frequencies of operation, to obtain all modes of propagation that the medium could sustain. The theoretical vertical patterns near the two frequencies of operation are plotted in figure 6, with typical elevation angles for several modes.

Figure 7 is a block diagram of the receiving system designed and built for the present task. In the RF chassis, the composite received signal was passed through a three-pole maximally flat-amplitude band-pass LC filter with a 3-dB bandwidth of 200 kHz. The LC filter was followed by a wideband amplifier with a 23-dB gain and a crystal filter having a near-Gaussian frequency response (and impulse response) with a bandwidth of 20 kHz. A rubidium frequency standard having an accuracy of about 1×10^{-11} drove a frequency synthesizer that delivered an accurate first-local-oscillator signal to the balanced mixer in the RF chassis, converting the RF signal to an IF signal with a carrier frequency of 100.080 kHz.

The 100-kHz first IF signal followed two paths. In the first path through the pulse chassis, an 11-notch filter suppressed the 11 strong tones to deliver slightly distorted received pulses. The distortion appeared as spurious pulses at various time delays with amplitudes about 25 dB below the true pulses and did not cause any significant difficulty. The pulses were then filtered in a five-pole LC bandpass filter with a near-Gaussian response and a 12-kHz bandwidth between the -4.35-dB points. The resulting filtered near-Gaussian pulses, which had been stretched to about 75- μ s duration by the filtering, were amplified and detected. The detected pulses were fed to an oscilloscope with a much shorter calibration pulse, where an intensity presentation was recorded on continuously moving 35-mm film. The detected pulses with the calibrating pulses were also fed to a second oscilloscope, not shown in figure 7, for a conventional amplitude vs. time display that was used to obtain periodic measurements of the pulse delays.

The second path followed by the 100-kHz first-IF signal was through the second-mixer chassis. The composite signal was passed through a low-pass filter with a 300-kHz cutoff frequency, which suppressed the

already reduced first-local-oscillator signal. The unmodified composite signal was then added to a second-local-oscillator signal that consisted of a number of equal-amplitude sinusoids with frequencies that were integral multiples of 0.2 kHz. To generate the spectrum, a 1-MHz signal from the rubidium frequency standard was passed through a continuously adjustable phase shifter to a chain of dividers in the reference chassis which delivered short pulses at an accurate recurrence rate of 0.2 kHz. The timing of this receiver reference waveform could be adjusted relative to the transmitter timing by adjustment of the phase shifter. The spectrum of the 0.2-kHz pulse train consisted of discrete components at integral multiples of 0.2 kHz from zero to more than 1 MHz. This local oscillator spectrum was added to the composite signal spectrum and the sum passed through a two-pole maximally flat-amplitude filter with a 16-kHz bandwidth centered on 100 kHz. The filter output was amplified and fed to 11 parallel second-mixer channels. Since the composite received signal was heterodyned in the first mixer so that the carrier tone ($k = 6$) had a frequency of 100.080 kHz and the local oscillator spectrum components had frequencies that were integral multiples of 0.2 kHz, each of the 11 tones in the composite LF signal was located 80 Hz higher than a component of the local oscillator spectrum. Each of the 11 signal tone-local oscillator component pairs, with their 80-Hz spacings, were separated from the total spectrum by a single bandpass crystal filter with a bandwidth of about 150 Hz. A single filter was used for each signal tone-local oscillator pair to minimize the differential phase shifts caused by changing filter temperatures. Had separate signal tone-local oscillator filters been used, considerably tighter filter specifications would have been required. Each crystal filter suppressed unwanted components by more than 60 dB. Each signal tone-local oscillator pair was fed to a second mixer that multiplied the pair. Each 80-Hz difference

component was separated with a two-pole maximally flat-amplitude bandpass filter with a 35-Hz 3-dB bandwidth centered at 80 Hz. Each of the 11 resulting 80-Hz second-IF tones was then amplified and delivered to 11 channels of a 14-channel tape recorder for FM recording at 7.5 in./sec.

For final detection of the 11 recorded tones when the tape was played back, 80-Hz "sine" and "cosine" square waves were also generated from the rubidium frequency standard in the reference chassis. The 80-Hz "sine" and "cosine" square waves were added to form a composite reference signal that was FM recorded on two of the 14 channels of the tape recorder. Since the tape recorder had two record heads, one for odd-numbered tracks and one for even-numbered, the composite reference signal was recorded near the center of the tape on both an odd-numbered track and an even-numbered track. On playback, to minimize wow-and-flutter distortion, the odd-numbered reference signal was used for detecting tones from the odd-numbered tracks and the even-numbered reference signal for detecting tones from the even-numbered tracks. The rather low second IF of 80 Hz was chosen with this requirement in mind.

Upon playback, "sine" and "cosine" reference square waves were reconstructed from each of the two composite reference signals. Each of the 11 played-back tones was fed to two switching detectors via a very broad bandpass filter (3-dB points at 20 and 300 Hz), which eliminated the higher frequency noise from the tape recorder. The switching detectors were driven by the appropriate "sine" and "cosine" square waves. The output signal from each switching detector passed through a three-pole maximally flat-amplitude low-pass active RC filter with a 7.7-Hz 3-dB cutoff frequency. For each tone, the two baseband output signals from the active filters were the real and imaginary components of $H_m(f_k, t)$.

The 80-Hz IF signals delivered by the second-mixer chassis also were fed to 11 parallel channels in the amplitude-monitor chassis. Each of the 80-Hz signal tones was amplified and half-wave rectified. The magnitude of each rectified signal, averaged over a fraction of a second, was monitored by a separate panel meter. Each rectified signal tone also drove a single-pole low-pass RC filter with selectable time constants of 100 and 1000 sec. A single high-impedance electrometer was used during the ionospheric channel measurements to measure and chart-record the long-term (1000 sec) average of the magnitude of one signal tone to obtain a visual record of slow channel-gain changes. Periodically, the electrometer was used to measure similar quantities for all 11 tones for a written record. One of the 11 signal tones was also envelope detected and passed through a three-pole, low-pass LC filter with a 10-Hz cutoff frequency to a chart recorder to obtain a visual record of the short-term fading conditions on the ionospheric channel.

The 0.2-kHz second-local-oscillator pulse train was also used to synchronize the oscilloscopes and to trigger a 2-ns pulse generator (not shown in fig. 7). Since the 2-ns pulses occurred at the 0.2-kHz reference rate, they contained spectral components at integral multiples of 0.2 kHz over the entire HF spectrum. This signal was fed to the receiver input at a suitable level to periodically calibrate the receiving system. Calibration adjustments included the amplitudes of the first- and second-local-oscillator signals, the amplitude of each first-IF signal tone, the amplitude and phase of each second-IF signal tone, the tape recorder, and the amplitude and phase of each of the 22 low-pass post-detection filters. For each tone, the level of the error component was about - 55 dB relative to the magnitude of the signal tone at the time of calibration and was found to hold over long periods (many days) to better than - 45 dB. When tests were originally made to determine the wow-and-flutter error

introduced by the tape recorder, the error components were at a - 45-dB level relative to the tones at the time of the recording. We subsequently found that with repeated playback of the tape, stretching and permanent deformation of the tape caused the error components to increase to nearly - 30 dB. Had a digital tape recorder been available for use at the receiving site at the time of the ionospheric channel measurements, the 11 second-IF signal tones could have been fed directly from the second-mixer chassis to the detector chassis, to eliminate the analog tape recorder. The 22 baseband output signals could then have been converted to digital form and recorded at the time of the measurements to maintain a - 45-dB error level. However, the - 30-dB limitation imposed by the analog tape recorder did not significantly limit the accuracy of the channel measurements, as will be seen later, since the errors in the fits of $H_d(f, t)$ to $H_m(f, t)$ were nearly always higher than the receiver errors because of the nonzero time spreads on the ionospheric modes.

Before making ionospheric channel measurements with the specially designed transmitting-receiving system, we tested the accuracy of the entire system (excluding the higher level linear amplifiers in the transmitter) in the laboratory. Two discrete nonfading paths with different propagation times were simulated by adding the receiver calibrating signal to the low-level transmitter output signal to form a simulated two-path received signal. An analog recording of the second-IF tones was made and subsequently fed through the detector chassis whose 22 baseband output signals were converted to digital form and tape-recorded in a computer-compatible format. The digital tape was then processed in the same way as subsequent measurements of the ionospheric channel. From the results of these analyses and a prior knowledge of the simulated channel, we could determine the overall accuracy of the measuring system. Overall errors were below a level of - 30 dB relative to the true values.

3.3 Measurements

Following the laboratory test on the accuracy of the transmitting-receiving system, the transmitting system was installed at the ESSA field site at Long Branch, Illinois ($40^{\circ}13'N$, $90^{\circ}01'W$). Tests were made with the receiving system at the transmitting site to insure that the complete transmitting system, including the high-level linear amplifiers and antenna, was operating satisfactorily. Nonlinearity in the higher level amplifiers did not measurably degrade the performance of the system. The receiving system was then installed at the ESSA field site at Table Mountain, about 10 miles north of Boulder, Colorado ($40^{\circ}08'N$, $105^{\circ}14'W$), which provided a great-circle distance of 1,294 km between the transmitting and receiving sites.

Following a brief period of familiarization, the transmitting-receiving system was operated on the two assigned frequencies of 5.864 MHz and 9.259 MHz. The lower frequency was used at night and the higher frequency during the day. In both cases, the operating frequency was sufficiently below the predicted maximum usable frequency to make it probable that both one- and two-hop modes would be seen.

The transmitting-receiving system was operated continuously during the three periods shown in table 1. During each period, both the transmitter and receiver were calibrated about once every hour. Between calibration periods and times required for tape rewinding, tape recordings of the ionospheric channel measurements were made; the total recording times are shown in table 1. Over 7 hours of recorded measurements were obtained at night on 5.864 MHz and nearly 10 hours in daytime on 9.259 MHz.

Table 1. Summary of Measurements

Date 1967	Frequency MHz	Hours MST	Record Time
7 November	9.259	12:10-19:07	5:09
9-10 November	5.864	22:05-08:50	7:18
30 November	9.259	07:25-15:40	4:43

The continuous strip-film photographs of the oscilloscope intensity display of the received pulses, chart recordings of tone amplitudes, and written data taken at the time of the measurements were analyzed to determine what portions of the data appeared most suitable for analysis. Twelve intervals were chosen that seemed most nearly stationary in terms of fading rates, modal time delays, and average powers in the modes. The analog tape recordings for these intervals were fed to the receiver detector chassis (fig. 7). The resulting 22 baseband analog output signals were then converted to digital sequences by the Ionospheric Telecommunication Laboratory's analog-to-digital (A-D) converter and tape recorded in a digital format suitable for the ESSA CDC-3800 computer. The sequence rate was either 3.125 or 6.25 Hz and was well above the Nyquist rate in all cases. Portions of three of these converted intervals, from both day and night measurements, were subsequently analyzed with computer programs prepared for this purpose.

In the remainder of the report, the portions of the intervals that were analyzed will be called samples, and will be designated I1, I2, and I3. In the analyses, values of the modal time delays for each sample were constant and were obtained from the pulse measurements of the ionospheric channel.

4. ANALYTICAL METHODS

Since the A-D conversion process changed $H_{\pi}(f_k, t)$ from a set of continuous functions in time to a set of sequences in time, it is desirable to change the notation. In each of the samples, I1, I2, and I3, let

t_{π} = time duration of the sample, and

m_a = actual number of values of $H_{\pi}(f_k, t)$ that are obtained
in the A-D conversion for each f_k .

Then the values of time, t_r , for which values in the sequence have been obtained are

$$t_r = r t_{\pi} / m_a, \quad r = 1, 2, 3, \dots, m_a. \quad (70)$$

It is convenient to divide the analyses of each sample into three parts:

- (a) The deterministic fit, in which the frequency response of the deterministic channel, $H_d(f_k, t_r)$, was fitted by least squares to the frequency response of the measured ionospheric channel, $H_{\pi}(f_k, t_r)$, repeatedly for successive values of t_r , to obtain solutions for the optimum tap-gain functions, $\{G_{d1}(t_r)\}$, in the deterministic channel. We also examined the accuracy of this fit.
- (b) The statistical fit, in which each tap-gain correlation function for the statistical channel model, $C_{s1}(\Delta t)$, was fitted by least squares to the corresponding tap-gain function for the deterministic channel, $C_{d1}(\Delta t)$, to obtain solutions for the optimum parameters in the statistical channel model. To test (d) on page 30, we then examined the resulting accuracy with which the statistical channel model fit the measured ionospheric channel.

(c) The hypothesis tests, in which the amplitude and phase distributions of the deterministic tap-gain functions, $\{G_{d1}(t_r)\}$, were submitted to suitable statistical tests to determine the validities of the bivariate Gaussian hypothesis and the independence hypothesis. The error in the fit of $C_{s1}(\Delta t)$ to $C_{d1}(\Delta t)$ was also tested to determine the validity of the Gaussian spectrum hypothesis. These tests satisfied (a), (b), and (c) on page 30.

The methods used in these three parts of the analyses are described below.

4.1 Deterministic Fit

The deterministic fit of $H_d(f_k, t_r)$ to $H_m(f_k, t_r)$ in frequency at each time, t_r , was done by least squares as described in appendix A. In general, not all the 11 frequencies of measurement, f_k , were used; better fits could be obtained over a limited central portion of the frequency band than over the entire band, and the bandwidth over which a good fit could be achieved depended upon the time spread on each of the modes in the ionospheric channel. For each time, t_r , the fit provided numerical solutions for "n" values of $G_{d1}(t_r)$, one for each path "i"; all the successive sets of solutions provided "n" sequences in time, $\{G_{d1}(t_r)\}$ - one sequence for each path "i" for values of $0 \leq t_r \leq t_p$.

The solutions for $\{G_{d1}(t_r)\}$ were used to compute the frequency response of the deterministic channel from a minor modification of (41),

$$H_d(f_k, t_r) = \sum_{i=1}^n G_{d1}(t_r) \exp(-j2\pi T_1 f_k) . \quad (71)$$

The accuracy with which the deterministic channel was fit to the measured ionospheric channel was then determined in two ways. In the first method, an error function was defined by and computed from

$$E(f_k, t_r) = H_d(f_k, t_r) - H_m(f_k, t_r) . \quad (72)$$

For each frequency, f_k , we computed the ratio of the RMS value of $|E(f_k, t_r)|$ in time to the corresponding RMS value of $|H_m(f_k, t_r)|$ in time from

$$\frac{E(f_k)}{H_m(f_k)} = \frac{\left[\frac{1}{m_a} \sum_{r=1}^{m_a} E^*(f_k, t_r) E(f_k, t_r) \right]^{\frac{1}{2}}}{\left[\frac{1}{m_a} \sum_{r=1}^{m_a} H_m^*(f_k, t_r) H_m(f_k, t_r) \right]^{\frac{1}{2}}} , \quad (73)$$

which served as a time average of the accuracy of the deterministic fit with frequency.

In the second method for determining the accuracy of the fit, we compared the channel correlation functions for the ionospheric and deterministic channels. An estimate of the channel correlation function for the ionospheric channel, along the frequency and time axes, Δf and Δt , were obtained from modifications of (9),

$$R_m(\Delta f, 0) = \frac{1}{m_a} \sum_{r=1}^{m_a} H_m^*(f_k, t_r) H_m(f_k + \Delta f, t_r) , \quad (74)$$

where

$$\Delta f = (f_l - f_k) , \quad l = k, (k + 1), \dots, 11 , \quad (75)$$

and

$$R_m(0, \Delta t) = \frac{1}{m'_a} \sum_{r=1}^{m'_a} H_m^*(f_s, t_r) H_m(f_s, t_r + \Delta t) , \quad (76)$$

where

$$m_a' \equiv m_a [1 - (\Delta t/t_m)] , \quad (77)$$

$$\Delta t = \text{integral multiple of } t_m/m_a .$$

The corresponding normalized functions were obtained from modifications of (12),

$$\bar{R}_m(\Delta f, 0) = R_m(\Delta f, 0)/R_m(0, 0) \quad (78)$$

and

$$\bar{R}_m(0, \Delta t) = R_m(0, \Delta t)/R_m(0, 0) . \quad (79)$$

Equations (74) through (79), with subscripts "d" replacing subscripts "m", were also used to compute similar values for $\bar{R}_d(\Delta f, 0)$ and $\bar{R}_d(0, \Delta t)$. Then the definitions

$$|\Delta \bar{R}_{df}(\Delta f)| = |\bar{R}_d(\Delta f, 0) - \bar{R}_m(\Delta f, 0)| \quad (80)$$

and

$$|\Delta \bar{R}_{dt}(\Delta t)| = |\bar{R}_d(0, \Delta t) - \bar{R}_m(0, \Delta t)| , \quad (81)$$

were used to compute a measure of the accuracy of the fit. The frequency pairs used in (80) are tabulated in table 2 below.

Table 2. Frequencies Used to Compute $R(\Delta f, 0)$

Frequency Separation Δf , kHz	Frequency Numbers k	Frequency Separation Δf , kHz	Frequency Numbers k
0	6, 6	3.0	2, 5
0.2	5, 6	3.2	2, 6
0.4	5, 7	3.4	2, 7
0.6	3, 4	3.8	1, 4
0.8	4, 5	4.2	2, 8
1.0	4, 6	4.6	1, 5
1.2	4, 7	4.8	1, 6
			(continued)

Table 2 (continued)

Frequency Separation Δf , kHz	Frequency Numbers k	Frequency Separation Δf , kHz	Frequency Numbers k
1.4	3, 5	5.0	1, 7
1.6	3, 6	5.8	1, 8
1.8	3, 7	6.4	1, 9
2.0	4, 8	8.0	1, 10
2.2	2, 4	9.6	1, 11
2.6	3, 8		

4.2 Statistical Fit

Using the computed values for $\{G_{d1}(t_r)\}$, we computed estimates of the tap-gain correlation functions for the deterministic channel from

$$C_{d1}(\Delta t) = \frac{1}{m_a'} \sum_{r=1}^{m_a'} G_{d1}^*(t_r) G_{d1}(t_r + \Delta t). \quad (82)$$

The normalized tap-gain functions then were obtained from (46),

$$\bar{C}_{d1}(\Delta t) = C_{d1}(\Delta t)/C_{d1}(0). \quad (83)$$

Similarly, the normalized tap-gain correlation function for each path in the statistical channel model is

$$\bar{C}_{s1}(\Delta t) = C_{s1}(\Delta t)/C_{s1}(0), \quad (84)$$

where $C_{s1}(\Delta t)$ is specified by (65).

We fit the statistical channel to the deterministic channel by first equating path power ratios, i. e., by specifying for each path that

$$C_{s1}(0) = C_{d1}(0). \quad (85)$$

Then $\bar{C}_{s1}(\Delta t)$ was fit to $\bar{C}_{d1}(\Delta t)$ for each path by least squares, as described

in appendix B, to obtain numerical values for $C_{s1a}(0)$, $C_{s1b}(0)$, $C_{s1}(0)$, ν_{s1a} , ν_{s1b} , σ_{s1a} , and σ_{s1b} . Equations (54), (57), (58), and (61) were then used to compute the statistical channel quantities $\hat{\tau}_s$, $\hat{\nu}_s$, $\hat{\rho}_s$, and $2\sigma_s$. A measure of the accuracy of the statistical fit for each path was computed from

$$|\Delta \bar{C}_{s1}(\Delta t)| = |\bar{C}_{s1}(\Delta t) - \bar{C}_{d1}(\Delta t)|. \quad (86)$$

To obtain a measure of the accuracy of the fit between the statistical channel and the measured ionospheric channel, the channel correlation function for the statistical channel was computed on the basis of the optimum numerical parameters. When the tap-gain correlation functions for the statistical channel model in (65) are substituted in (47), the latter becomes the channel correlation function for the statistical channel,

$$R_s(\Delta f, \Delta t) = \sum_{i=1}^n \left[C_{s1a}(0) \exp(-j2\pi\tau_{i1}\Delta f - 2\pi^2\sigma_{s1a}^2\Delta t^2 + j2\pi\nu_{s1a}\Delta t) + C_{s1b}(0) \exp(-j2\pi\tau_{i1}\Delta f - 2\pi^2\sigma_{s1b}^2\Delta t^2 + j2\pi\nu_{s1b}\Delta t) \right]. \quad (87)$$

For paths where the two magnetoionic components are merged into one component, $C_{s1b}(0)$ becomes zero, and the "a" subscripts are dropped in (87). The normalized channel correlation function for the statistical channel model from (12) becomes

$$\bar{R}_s(\Delta f, \Delta t) = R_s(\Delta f, \Delta t)/R_s(0, 0). \quad (88)$$

The optimum numerical parameters for the statistical channel obtained from the least-squares fits of $\bar{C}_{s1}(\Delta t)$ to $\bar{C}_{d1}(\Delta t)$ were used to compute (88) along the Δf and Δt axes. We then compared the results, $\bar{R}_s(\Delta f, 0)$ and $\bar{R}_s(0, \Delta t)$, with the corresponding functions for the measured ionospheric channel, $\bar{R}_m(\Delta f, 0)$ and $\bar{R}_m(0, \Delta t)$, using

$$|\Delta \bar{R}_{st}(\Delta f)| = |\bar{R}_s(\Delta f, 0) - \bar{R}_n(\Delta f, 0)| \quad (89)$$

and

$$|\Delta \bar{R}_{st}(\Delta t)| = |\bar{R}_s(0, \Delta t) - \bar{R}_n(0, \Delta t)| \quad (90)$$

Equations (89) and (90) provided a final measure of the accuracy of the fit of the statistical channel model to the measured ionospheric channel.

Recalling from (52) that the channel time-scatter function, $u(\tau)$, for both the deterministic and statistical channel models is the sum of "n" delta functions with different delays, and from (17) that $R(\Delta f, 0)$ is the Fourier transform of $u(\tau)$ for any stationary time-varying channel, we see that $R_d(\Delta f, 0)$ and $R_s(\Delta f, 0)$ are both the sum of "n" vectors of constant amplitude rotating at different rates with increasing Δf . Equation (87) at $\Delta t = 0$ states this specifically for $R_s(\Delta f, 0)$. Consequently, $R_d(\Delta f, 0)$ and $R_s(\Delta f, 0)$ both oscillate indefinitely with increasing Δf and do not damp out. On the other hand, each mode in the ionospheric channel will always have at least a small amount of time spread; thus, while $R_n(\Delta f, 0)$ will also oscillate with increasing Δf , because the differential propagation times of the modes are large compared to the individual time spreads on the modes, the oscillation will damp out, and $|R_n(\Delta f, 0)|$ will approach zero with increasing Δf because of the nonzero time spreads. As a result, the differences specified by (80) and (89) will be almost entirely caused by the differences in the damping. Therefore, it is possible to use either of these differences to estimate the time spreads on the ionospheric modes. If we assume that each ionospheric mode has the same Gaussian time spread, $2\rho_e$, the channel time-scatter function for the ionospheric channel in this temporary representation can be defined by

$$u_n^i(\tau) \equiv \sum_{i=1}^n C_{s,i}(0) (2\pi\rho_e^2)^{-\frac{1}{2}} \exp[-(\tau - \tau_i)^2 / (2\rho_e^2)] \quad (91)$$

Equation (91) can be Fourier transformed to obtain

$$R_m^i(\Delta f, 0) \sum_{i=1}^n C_{si}(0) \exp(-2\pi^2 \rho_e^2 \Delta f^2 - j2\pi\tau_i \Delta f), \quad (92)$$

and when (47) at $\Delta t = 0$ is substituted in (92), the result can be normalized to give

$$\bar{R}_m^i(\Delta f, 0) = \bar{R}_s(\Delta f, 0) \exp(-2\pi^2 \rho_e^2 \Delta f^2). \quad (93)$$

Now let

$$|\bar{R}_s(\Delta f, 0) - \bar{R}_m^i(\Delta f, 0)| = |\bar{R}_s(\Delta f, 0) - \bar{R}_m(\Delta f, 0)|. \quad (94)$$

When (93) is substituted in (94), the latter can be solved to obtain

$$2\rho_e = [1/(\pi\Delta f)] [-2 \ln(1 - |\bar{R}_s(\Delta f, 0) - \bar{R}_m(\Delta f, 0)| / |\bar{R}_s(\Delta f, 0)|)]^{-\frac{1}{2}}. \quad (95)$$

Equation (95) was used in the analyses as an estimate of the time spread on the modes in the ionospheric channels.

For convenient presentation of the results of our measurements and analyses in section 5, we rated the magnitudes of the differences of the correlation functions as specified by (80), (81), (86), (89), and (90) in qualitative terms. A somewhat arbitrary assignment of these qualitative ratings vs. the magnitude of the difference (error) is listed in table 3 below.

Table 3. Ratings of Correlation Errors

Size of Error	Rating
Error ≤ 0.05	Excellent
$0.05 < \text{Error} \leq 0.10$	Good
$0.10 < \text{Error} \leq 0.20$	Adequate
Error > 0.20	Poor

4.3 Hypothesis Tests

In the statistical channel model, we hypothesized that each of the tap-gain functions, $G_{s1}(t)$, should be an independent baseband bivariate Gaussian random function with a zero mean value and quadrature components with equal RMS values (the bivariate Gaussian hypothesis), that the tap-gain functions should be independent (the independence hypothesis), and that each tap-gain spectrum, $v_1(\nu)$, should in general consist of the sum of two Gaussian functions of frequency (the Gaussian spectrum hypothesis). The statistical tests that were performed on the data to accept or reject the hypotheses are described below.

For the bivariate Gaussian hypothesis to be valid, each deterministic tap-gain function, $G_{d1}(t_r)$, within the limitations imposed by the finite sample size, should have a Rayleigh amplitude distribution and a uniform phase distribution. While it is conceptually possible to have functions with Rayleigh amplitude distributions and uniform phase distributions that are not bivariate Gaussian, the probability of such functions in any natural physical process is extremely small. If a natural process exhibits a Rayleigh amplitude distribution and a uniform phase distribution, it may be considered almost certain that the process is bivariate Gaussian. Therefore, to test the validity of the bivariate Gaussian hypothesis, we performed suitable tests on each $G_{d1}(t_r)$ in each sample to determine if it had a Rayleigh amplitude distribution and a uniform phase distribution.

For each path, an amplitude-density histogram was directly computed from $|G_{d1}(t_r)|$. For a reason given in appendix C, $\exp(j2\pi\nu_{s1}t)$, the factor in $\mathcal{G}_{d1}(t_r)$ corresponding to the frequency shift ν_{s1} , was removed, and the resulting modified function, $\mathcal{G}_{d1}'(t_r)$, was used to compute the phase-density histogram.

To compute the amplitude-density histograms, the domain $0 \leq |G_{d1}(t_r)| < \infty$ was divided into a suitable number of subintervals of various sizes that were numbered 1, 2, 3, ..., ℓ , ..., λ_{11} , and

$$o_{11}^1(\ell) = m_{11}(\ell)/m_a \quad (96)$$

was computed, where $m_{11}(\ell)$ was the number of values of $|G_{d1}(t_r)|$ observed to fall in the ℓ -th subinterval, and m_a was the total number of values of $G_{d1}(t_r)$ in the sample.

Similarly, for each phase-density histogram, the domain $0 \leq \angle G_{d1}(t_r) < 2\pi$ was divided into a suitable number of subintervals of equal size and numbered 1, 2, 3, ..., ℓ , ..., λ_{12} , and

$$o_{12}^1(\ell) = m_{12}(\ell)/m_a \quad (97)$$

was computed, where $m_{12}(\ell)$ was the number of values of $\angle G_{d1}(t_r)$ observed to fall in the ℓ -th subinterval.

To test the bivariate Gaussian hypothesis, we compared the values computed in (96) and (97) with the expected values for a valid hypothesis, which are the values for the statistical channel model. The Rayleigh amplitude-density function for each tap-gain function in the statistical channel model can be written

$$p(|G_{s1}|) = [2|G_{s1}|/C_{s1}(0)] \exp[-|G_{s1}|^2/C_{s1}(0)] \quad (98)$$

$C_{s1}(0)$ was set equal to the numerical value for $C_{d1}(0)$, and the probability in each subinterval of an amplitude density histogram for the statistical model was computed from

$$e_{11}^1(\ell) = \int_{\alpha_{(\ell-1)}}^{\alpha_{\ell}} p(|G_{s1}|) d|G_s|, \quad (99)$$

where

$\alpha_{(l-1)}, \alpha_l$ = bounds on the l -th subinterval.

The probability in each subinterval of a phase-density histogram was computed from

$$e_{12}^l(l) = 1/\lambda_{12} \quad (100)$$

Since each histogram had a number of subintervals, it was desirable to use a hypothesis test that simultaneously evaluated the differences between the computed and the expected values in all subintervals in each distribution. The chi-square test (Bendat and Piersol, 1966) was chosen, by which the statistic

$$\chi_1^2 = \sum_{l=1}^{\lambda_1} [o_1(l) - e_1(l)]^2 / e_1(l) \quad (101)$$

is computed, where

$o_1(l)$ = the number of independent values of $|G_{d1}(t_r)|$ or $\angle G_{d1}(t_r)$ that fall in the l -th subinterval.

$e_1(l)$ = the expected number of independent values in the l -th subinterval.

Since successive values of each $G_{d1}(t_r)$ were highly correlated, it was necessary to estimate m_{e1} , the effective number of independent values of each $G_{d1}(t_r)$ in a sample. This number was different for each path and always considerably smaller than the actual number of values, m_a . The method by which m_{e1} was estimated for each path is described in appendix C.

Then, for both the amplitude- and phase-density histograms,

$$o_1(l) = m_{e1} o_1^l(l), \quad o_1(l) > 5 \quad (102)$$

The restriction on (102) was imposed to insure accuracy in the chi-square test and was met for each distribution by suitable selection of the number and sizes of the subintervals. Similarly,

$$e_i(\ell) = m_{e_i} e_i^1(\ell) . \quad (103)$$

Then (101) becomes

$$\chi_i^2 = m_{e_i} \sum_{\ell=1}^{\lambda_i} [o_i^1(\ell) - e_i^1(\ell)]^2 / e_i^1(\ell) . \quad (104)$$

For each path, (104) was used to compute two values, χ_{i1}^2 for the amplitude distribution and χ_{i2}^2 for the phase distribution. In both cases, the number of degrees of freedom was equal to the number of subintervals, λ_{i1} or λ_{i2} , minus the number of different independent linear restrictions imposed upon the observations. Both were reduced by one because the computed probability for the last subinterval is determined when the probabilities in the first $\lambda_i - 1$ subintervals are determined. For the amplitude distributions, the number of degrees of freedom was reduced by an additional one because $C_{e_i}(0)$ was set equal to $C_{d_i}(0)$; consequently, the number of degrees of freedom used were $\lambda_{i1} - 2$ for the amplitude distributions and $\lambda_{i2} - 1$ for the phase distributions.

For each path, a table of chi-square distributions was used to obtain χ_{i1}^2 and χ_{i2}^2 , the tabulated values of chi-square at a significance level of 0.1 for the appropriate numbers of degrees of freedom for the amplitude and phase distributions, respectively. Normalized values of χ_{i1}^2 and χ_{i2}^2 were obtained from

$$\bar{\chi}_i^2 = \chi_i^2 / \chi_{i1}^2 . \quad (105)$$

A value of $\bar{\chi}_i^2 \leq 1$ was used as a criterion of acceptance of the bivariate Gaussian hypothesis for that particular distribution.

To test the independence hypothesis, it was necessary to determine whether each tap-gain function, $G_{d1}(t_r)$, was independent of all other tap-gain functions in the sample. This we did by taking all possible combinations of normalized tap-gain functions, two at a time, and obtaining an estimate of the magnitude of their crosscorrelation from

$$|\Gamma_{i\ell}| = \left| \frac{1}{m_a} \sum_{r=1}^{m_a} \bar{G}_{d1}^*(t_r) \bar{G}_{d\ell}(t_r) \right|, \quad \begin{matrix} i = 1, 2, \dots, (n-1), \\ \ell = (i+1), (i+2), \dots, n. \end{matrix} \quad (106)$$

If the modes in the ionospheric channel were independent, the estimate from (106) would still be greater than zero because of the finite number of values in the sample. For independent bivariate Gaussian tap-gain functions, it is shown in appendix D that $|\Gamma_{i\ell}|$ would have a Rayleigh distribution for a large number of samples, and that a conservative estimate of the RMS value of this distribution would be

$$\epsilon_{i\ell} \approx 1/\sqrt{m_{e i\ell}}, \quad (107)$$

where $m_{e i\ell}$ is the larger of $m_{e i}$ and $m_{e \ell}$, the effective number of independent values for paths "i" and "l" as derived in appendix C. Since $|\Gamma_{i\ell}|$ would be expected to exceed $1.5 \epsilon_{i\ell}$ for 10 percent of a large number of samples,

$$|\bar{\Gamma}_{i\ell}| = |\Gamma_{i\ell}| / (1.5 \epsilon_{i\ell}) \quad (108)$$

was computed for each of the combinations of path pairs. If the tap-gain functions had previously been accepted as bivariate Gaussian functions, a value of $|\bar{\Gamma}_{i\ell}| \leq 1$ was used as a criterion of acceptance that the tap-gain functions were uncorrelated and consequently independent.

In the computed amplitude and phase distributions for each path that are presented for each sample in section 5, the amplitude distributions are presented as cumulative distributions plotted on nonlinear "Rayleigh"

paper. In these plots, an ideal Rayleigh cumulative distribution is a straight line with a unit slope. It is interesting to show the distribution that the points computed from $|G_{d1}(t_r)|$ would be expected to have about the Rayleigh line for an infinite number of samples. Strictly speaking, because of the finite number of values in the samples, this would be a binomial distribution, but the binomial distribution can be approximated by a Gaussian distribution if the restriction imposed on (102) holds. Curves of the standard deviation of the Gaussian spread of the computed points, $\sigma_g(\alpha, m_{e1})$, as a function of the amplitude level, α , and the effective number of independent values, m_{e1} , are plotted in figure 8 over the portions of the domain for which the Gaussian approximation holds. The plus and minus one-sigma bounds on the cumulative distribution for $m_{e1} = 300$ are also plotted. As $\alpha \rightarrow 0$ or as $\alpha \rightarrow \infty$, the spread of the computed points on the Rayleigh paper also increases, particularly as $\alpha \rightarrow 0$.

To test the validity of the Gaussian spectrum hypothesis, a statistical test was performed on (86). Since the tap-gain spectrums in both the deterministic and statistical channels are Fourier transforms of the corresponding tap-gain correlation functions and $C_{d1}(\Delta t)$ is obtained indirectly from measurements of the ionospheric channel, (86) is a measure of the accuracy with which each tap-gain spectrum in the statistical channel fits the corresponding estimate of the spectrum in the ionospheric channel. However, even if the path spectrums in the ionospheric channel were composed of two truly Gaussian components, as was assumed in the statistical channel model, a nonzero difference would be expected in (86) because of the finite number of values in the sample. The distribution that (86) would have for a large number of samples, assuming the bivariate Gaussian and the Gaussian spectrum hypotheses were both true, was derived in appendix D. The approximate RMS value of this distribution is

$$\epsilon_{c1} \approx 1/\sqrt{m_{e1}} , \quad (109)$$

which applies for all Δt . For each path, we compared (86) with (109) to decide if the Gaussian spectrum hypothesis in the statistical channel model was valid, under the restriction that the bivariate Gaussian hypothesis was also shown to be valid for the path.

5. RESULTS

5.1 Sample II

The first sample of data, II, was taken from daytime measurements on 9.259 MHz on November 30, 1967, from 10:15 to 10:28 MST. During this 13-min interval, the ionosphere supported three modes, a 1E mode, a 1F mode, and a 2F mode. The time delays on the modes or paths relative to the arbitrary 200-Hz receiver reference were 40, 290, and 1139 μ s. The power ratios for the three paths relative to the power ratio of the channel, as determined from the analyses, were - 1.2, - 7.2, and - 13.5 dB, respectively. These data, as well as other pertinent results obtained in the analyses of sample II, which are discussed below, are tabulated in table 4.

In the deterministic fit of $H_d(f_k, t_r)$ to $H_m(f_k, t_r)$, the fit was made at seven central frequencies ($k = 3, 4, 5, 6, 7, 8$, and 9 in fig. 4a). Values of $H_m(f_k, t_r)$ for the two outer tones on each side of the band ($k = 1, 2, 10$, and 11) were not used in the fit, but the solutions for $\{G_{d1}(t_r)\}$ were used to compute $H_d(f_k, t_r)$ at all 11 frequencies, so that the error in the fit could be examined at all 11 frequencies.

The RMS error in the fit, as defined by (72) and (73), is presented by the dashed lines in figure 9. The errors at the seven frequencies used in the deterministic fit are shown as unfilled circles; the filled

Table 4. Summary of Sample 11 Results

Frequency	9.259 MHz
Date	November 30, 1967
Time	10:15 - 10:28 MST; $t_m = 780$ s
Number of paths	$n = 3$
Measurement rate	$f_m = 3.125$ Hz
Actual number of values	$m_a = 2437$
Channel time delay	$\hat{T}_s = 137$ μ s
Channel time spread	$2\rho_s = 478$ μ s
Channel frequency shift	$\hat{\nu}_s = 0.0013$ Hz
Channel frequency spread	$2\sigma_s = 0.123$ Hz
Estimate of path time spreads	$2\rho_e = 20$ μ s

Path Values

Path	Time Delay	Rel. Power Ratio	Freq. Shift	Freq. Spread	Eff. Number Values	Correl. Spread	Normalized Chi-square Values
i	T_i μ s	$\frac{C_{s1}(0)}{R_s(0,0)}$ dB	ν_{s1} Hz	$2\sigma_{s1}$ Hz	m_{s1}	ϵ_{c1}	$\bar{\chi}_{11}^2, \bar{\chi}_{12}^2$
1a	40	- 4.1	0.0022	0.0073			
1b	40	- 4.3	0.0170	0.0318			
1	40	- 1.2	0.0094	0.0272	30.3	0.181	0.04, 0.47
2	290	- 7.2	0.0089	0.144	198.5	0.071	0.24, 0.25
3	1139	- 13.5	-0.167	0.340	469.4	0.046	0.14, 0.26

circles are values of the error at the four frequencies not used in the deterministic fit. As expected, the error levels at the latter four frequencies are higher than at the seven central frequencies. Since the errors that were introduced by the measuring system were known to be below - 30 dB, the errors plotted in figure 9 are almost entirely caused

by the limitations of the deterministic channel model; i. e., the discrete paths in the deterministic channel model only approximate the nonzero time spreads of the ionospheric modes.

Had fewer than seven central tones been used in the fit (say five, for $k = 4, 5, 6, 7$, and 8), the average of the errors at these frequencies would have been lower than the seven-tone average in figure 9, but this result would have been obtained at the price of a higher average error for the outer tones not used in the fit. On the other hand, had all 11 tones been used, the average error for the four outer tones ($k = 1, 2, 10$, and 11) would have been lower than in figure 9, but the price for this would have been an average error higher than that of figure 9 for the seven central frequencies. The choice of the number of frequencies used in the deterministic fit is, therefore, a compromise. The choice of seven central tones for the deterministic fit of sample II was believed to be about optimum.

We examined the error in the deterministic fit also by comparing $\bar{R}_d(\Delta f, 0)$ with $\bar{R}_m(\Delta f, 0)$ and $\bar{R}_d(0, \Delta t)$ with $\bar{R}_m(0, \Delta t)$, in the manner described by equations (80) and (81). Figure 10 is a plot of the amplitude and phase components of $\bar{R}_m(\Delta f, 0)$ and $\bar{R}_d(\Delta f, 0)$, as well as the magnitude of their difference. Computed values were obtained at the 25 values listed in table 2 and are indicated by the junctions of the line segments in figure 10. Lines were used in the plots because the separation of adjacent computed points in frequency at larger values of Δf was too great for a meaningful curve. Smoothing the error curve in figure 10 and using the ratings of table 3, we see that the deterministic fit in frequency is excellent for a bandwidth up to 3.0 kHz, good to about 6.0 kHz, and adequate to about 12 kHz.

The periods of the cyclic variations in both the amplitude and phase plots in figure 10 are determined by the differential time delays of the

paths. As the time delays in table 4 show, the two stronger paths, $i = 1$ and $i = 2$, have a differential delay of $250 \mu\text{s}$, whose reciprocal of 4.0 kHz agrees with the period of the strongest oscillation in figure 10. The time difference of the next strongest pair of modes, $i = 1$ and $i = 3$, is $1099 \mu\text{s}$, whose reciprocal of 0.91 kHz is also seen in figure 10.

Figure 11 shows $\bar{R}_x(0, \Delta t)$ and $\bar{R}_d(0, \Delta t)$ plotted with the magnitude of their difference; the error is excellent, averaging about 0.01. The results are considerably better than in figure 10 because the error in figure 11 is in no way limited by the deterministic channel model; all the deterministic tap-gain functions can be nonstationary and have whatever tap-gain correlation functions and tap-gain spectrums are required to obtain an excellent fit. The fit in figure 11 lacks perfection because of the least-squares method of obtaining the deterministic fit, and the error is a direct result of the RMS error in figure 9 at $k = 6$. On the other hand, as mentioned above, the discrepancy in figure 10 is almost entirely caused by the approximation of the time-spread ionospheric modes by discrete paths in the deterministic model.

In figure 11, as well as in subsequent figures, computed correlation functions of time, $\bar{R}_x(0, \Delta t)$, $\bar{R}_d(0, \Delta t)$, and $\bar{C}_{d1}(\Delta t)$, never completely go to zero as Δt increases. Even though the functions that are numerically correlated have true zero correlations for large values of Δt , the computed correlation functions are based upon a finite amount of data and, consequently, have nonzero residuals. Therefore, in figure 11 and each subsequent time-correlation plot, the computed function is plotted approximately over that portion of the domain where the function exceeds the residual magnitude and has significance.

Figure 12 presents plots of the tap-gain correlation functions for the deterministic channel and the statistical channel for path $i = 1$, as well as the magnitude of their difference. Figures 13 and 14 are similar

plots for paths $i = 2$ and $i = 3$. In each case, the parameters in the statistical channel model were determined from a least-squares fit of $\bar{C}_{s1}(\Delta t)$ to $\bar{C}_{d1}(\Delta t)$ at the indicated data points in the error plots of figures 12, 13, and 14. In figure 12, for path $i = 1$, two magnetoionic components were used in the statistical channel model. In figures 13 and 14, for $i = 2$ and $i = 3$, only a single Gaussian spectrum component was used in the statistical channel model, since the deterministic tap-gain correlation functions were both near-Gaussian in shape. From the error curves in the three figures, we see that the fits were good.

The time delays, frequency shifts, and frequency spreads that were obtained for each path in the statistical channel, as well as the similar channel values, are listed in table 4. The resulting tap-gain spectrums for each of the three paths in the statistical channel are presented in figure 15, after they had been scaled to make the channel power ratio, $R_s(0, 0)$, equal to one. Because of the logarithmic ordinate, the Gaussian tap-gain spectrums appear as parabolic curves. The frequency spread on the first 1E mode, 0.0272 Hz, was much less than the 0.144-Hz spread on the second 1F mode and the 0.340-Hz spread on the third 2F mode, corresponding to its lower fade rate and longer correlation time. The third 2F mode has a larger frequency spread than the second 1F mode as one would expect because of the double reflection. For vertical incidence, it is known that the frequency spread on a two-hop mode will be greater than the frequency spread on a one-hop mode from the same layer and reflection point by a factor of $\sqrt{2}$ (Essex and Hibberd, 1967). However, when the one- and two-hop modes have different oblique incidences and reflection points with large geographical separation, as in the present case, a different ratio of frequency spreads would generally result. Even for fixed angles of incidence, the ratio of the frequency spreads would be expected to vary considerably with geography and time,

but one would usually expect the two-hop path to exhibit a greater frequency spread than a one-hop path in the oblique case. In sample 11, the ratio of the 2F frequency spread to the 1F frequency spread was 2.36.

A direct measure of the accuracy of the fit of the statistical channel to the measured ionospheric channel was made by comparing $\bar{R}_s(\Delta f, 0)$ with $\bar{R}_m(\Delta f, 0)$ and $\bar{R}_s(0, \Delta t)$ with $\bar{R}_m(0, \Delta t)$. Plots of $\bar{R}_s(\Delta f, 0)$ and $\bar{R}_m(\Delta f, 0)$ are presented in figure 16 with the magnitude of their difference. The accuracy of the fit of the statistical channel in figure 16 is essentially the same as the corresponding fit of the deterministic channel in figure 10; based on smoothed error values, the fit in figure 16, as in figure 10, is excellent to about 3.0 kHz, good to about 6.0 kHz, and adequate to about 12 kHz. This is not surprising, since the deterministic and statistical channel have identical delays and power ratios on each discrete path and, consequently, have identical channel time-scatter functions. Since $\bar{R}(\Delta f, 0)$ is the Fourier transform of the channel time-scatter function, $u(\tau)$, $\bar{R}_d(\Delta f, 0)$ and $\bar{R}_s(\Delta f, 0)$ are nominally the same. The differences between figures 16 and 10 are caused by $\bar{R}_d(\Delta f, 0)$ being computed by crosscorrelating $H_d(f_k, t_r)$ according to (74) with "d" subscripts and $\bar{R}_s(\Delta f, 0)$ being computed from the statistical channel time-scatter function via (87) and (88). The RMS values in time of $|H_d(f_k, t_r)|$ vary slightly with "k" because of the finite sample size, making $\bar{R}_d(\Delta f, 0)$ differ from $\bar{R}_s(\Delta f, 0)$, which is based indirectly on all values of "k". Since figures 10 and 16 are nominally the same, figure 10 is actually redundant.

Based on averages of values from figure 16 in (95), a rough estimate of the effective time spread on the ionospheric modes, $2\rho_o$, was 20 μ s. If

$$B = 1/[4(2\rho_o)] \quad (110)$$

is used as an estimate of the bandwidth over which the fit is adequate,

B = 12.5 kHz results, which agrees with the previous adequate qualitative rating.

Plots of $\bar{R}_s(0, \Delta t)$ and $\bar{R}_d(0, \Delta t)$ are presented in figure 17 with the magnitude of their difference. Unlike $\bar{R}_d(\Delta f, 0)$ and $\bar{R}_s(\Delta f, 0)$, which are nominally identical, $\bar{R}_d(0, \Delta t)$ and $\bar{R}_s(0, \Delta t)$ would be expected to differ considerably. A comparison of figure 17 with figure 11 confirms this; the error in figure 17 for $\bar{R}_s(0, \Delta t)$ is considerably larger than the error for $\bar{R}_d(0, \Delta t)$ in figure 11. It is greater because the tap-gain spectrums in the statistical channel are restricted to either one or two Gaussian functions, while the corresponding tap-gain spectrums in the deterministic channel model are unrestricted. Although the error in the statistical fit in figure 17 is considerably greater than the error in the deterministic fit in figure 11, the error averages about 0.06 in the statistical fit, which is good. When figures 16 and 17 are considered together as a measure of the accuracy of the fit of the statistical channel to the measured ionospheric channel, the fit can be rated good for bandwidths up to about 6 kHz and adequate up to 12 kHz.

Amplitude- and phase-density histograms for each of the tap-gain functions in the deterministic channel, $G_{d1}(t_r)$, were computed and used in chi-square tests of the bivariate Gaussian hypothesis. Figure 18 is a plot of the cumulative distributions of $\{|G_{d1}(t_r)|\}$, whose computed values are shown by the circles. The solid lines are the corresponding distributions for the statistical channel. Also shown, but not used in the chi-square tests, are the cumulative distributions of $|H_m(f_k, t_r)|$ for all 11 values of f_k , and the corresponding distribution for the statistical channel. All plots in figure 18 are for $R(0, 0) = 1$, a channel power ratio of one. As we see, the computed data points for $P(|G_{d1}|)$ for each path diverge from the ideal Rayleigh lines for both high and low probabilities, but particularly for the low probabilities, as expected from the theoretical curves in figure 8.

Figure 19 shows plots of the distributions of $\mathcal{G}_{d1}^i(t_r)$ for each path with the corresponding uniform distributions for the statistical channel model. Also shown, but not used in the chi-square tests, was the distribution of $\mathcal{H}_m^i(f_k, t_r)$ for all 11 values of f_k , and the corresponding uniform distribution for the statistical channel. For path $i = 1$, $p(\mathcal{G}_{d1}^1)$ differs from $p(\mathcal{G}_{s1}^1)$ by rather large values because of the small effective number of independent values, $m_{e1} = 30$ (table 4). For the second and third paths, the differences are less because of the larger effective number of independent values. For all three paths, the effective number of independent values was considerably less than the actual number obtained in the A-D conversion, 2437. The resulting normalized values of chi-square for each of the $2n = 6$ distributions are tabulated in table 4 for a significance level of 0.1. Since none of the normalized chi-square values was excessive (> 1), we concluded that the bivariate Gaussian hypothesis was valid for all 3 paths.

To test the independence hypothesis, we computed the magnitude of the crosscorrelations between the various deterministic tap-gain functions according to (108). These values are listed in table 5. Since all three combinations of path pairs had normalized crosscorrelation values less than one, we concluded the tap-gain functions, $\{\mathcal{G}_{di}(t_r)\}$, were uncorrelated and because they had been accepted as bivariate Gaussian, independent.

Table 5. Sample II Crosscorrelations

Path Pair	Crosscorrelation
i, l	$ \bar{\Gamma}_{il} $
1, 2	0.65
1, 3	0.59
2, 3	0.68

To test the Gaussian spectrum hypothesis, (109) was used to compute the approximate RMS value of $|C_{s1}(\Delta t) - C_{d1}(\Delta t)|$ for each path, ϵ_{c1} . For paths $i = 1, 2$, and 3 , these values were 0.181 , 0.071 , and 0.046 , respectively, as listed in table 4. Since the error curves in figures 12, 13, and 14 were less than these RMS values over all or most of the three domains, we concluded the Gaussian spectrum hypothesis was valid for all paths in sample 11.

5.2 Sample 12

The second sample of data, 12, was taken from daytime measurements on 9.259 MHz on November 30, 1967, from 11:10 to 11:20 MST, approximately 1 hour later than 11. During this 10-min interval, the ionosphere supported four modes, a 1E mode, a 1F mode, an M mode, and a 2F mode. (An M mode consists of a downward reflection from an F layer, an upward reflection from an E layer, and a second downward reflection from the F layer.) The time delays on the modes or paths relative to the arbitrary 200-Hz receiver reference were 40, 290, 590, and 1126 μ s. The power ratios for the four paths relative to the power ratio of the channel were - 1.7, - 5.9, - 17.6, and - 12.6 dB, respectively. These data as well as other pertinent results obtained in the analyses of sample 12 are tabulated in table 6.

The deterministic fit of $H_d(f_k, t_r)$ to $H_n(f_k, t_r)$ was made at seven central frequencies ($k = 3, 4, 5, 6, 7, 8$, and 9). The RMS error in the fit is presented in figure 9 and is roughly the same as for sample 11; the error is less at the seven central frequencies that were used in the fit than at the four outer frequencies that were not used in the fit. Again, the limitation in the accuracy of the fit was almost entirely due to the limitations of the deterministic channel model; i.e., the discrete paths in the deterministic channel model only approximate the nonzero time spreads of the ionospheric modes.

Table 6. Summary of Sample I2 Results

Frequency	9.259 MHz
Date	November 30, 1967
Time	11:10 - 11:20 MST; $t_m = 600$ s
Number of paths	$n = 4$
Measurement rate	$f_m = 6.25$ Hz
Actual number of values	$m_a = 3750$
Channel time delay	$\hat{\tau}_s = 173$ μ s
Channel time spread	$2\rho_s = 520$ μ s
Channel frequency shift	$\hat{\nu}_s = 0.0171$ Hz
Channel frequency spread	$2\sigma_s = 0.140$ Hz
Estimate of path time spreads	$2\rho_{s_i} = 30$ μ s

Path Values

Path	Time Delay	Rel. Power Ratio	Freq. Shift	Freq. Spread	Eff. Number Values	Correl. Spread	Normalized Chi-square Values
i	τ_i	$\frac{C_{s_i}(0)}{R_s(0,0)}$	ν_{s_i}	$2\sigma_{s_i}$	m_{s_i}	ϵ_{c_i}	$\bar{\chi}_{11}^2, \bar{\chi}_{12}^2$
	μ s	dB	Hz	Hz			
1a	40	- 4.1	-0.0008	0.0064			
1b	40	- 5.5	0.0127	0.0084			
1	40	- 1.7	0.0071	0.0153	15.0	0.258	0.06, 0.03
2	290	- 5.9	0.0159	0.180	191.4	0.072	0.12, 0.23
3	590	- 17.6	0.108	0.334	354.7	0.053	0.48, 0.16
4	1126	- 12.6	0.118	0.336	356.8	0.053	0.42, 0.18

Although of no importance in achieving the goals of the present task, the amplitude and phase distributions of the error in the deterministic fit, $E(f_k, t_r)$, were computed and examined as a matter of curiosity. The amplitude distributions were computed for each of the 11 frequencies, but, for clarity, only seven are presented in figure 20a. All 11 frequencies

were used to compute the phase-density histograms in figure 20b. No chi-square tests were performed on the distributions, but rough estimates showed that the plots were sufficiently close to the ideal Rayleigh and uniform distributions, considering the effective number of independent values, to conclude that $E(f_k, t_r)$ at each frequency is a bivariate-Gaussian function with a zero mean value and quadrature components with equal power ratios.

In the regular analyses, we also examined the error in the deterministic fit by comparing $\bar{R}_d(\Delta f, 0)$ with $\bar{R}_m(\Delta f, 0)$ and $\bar{R}_d(0, \Delta t)$ with $\bar{R}_m(0, \Delta t)$. Figure 21 is a plot of $\bar{R}_d(\Delta f, 0)$ and $\bar{R}_m(\Delta f, 0)$ and the magnitude of their difference. Smoothing the error curve, we see that the deterministic fit in frequency is excellent for a bandwidth up to 2.0 kHz, good to about 4.0 kHz, and adequate to about 8.0 kHz. The bandwidth over which sample 12 had an adequate deterministic fit, consequently, was about 2/3 of the bandwidth obtained for sample 11. The periods of the two strongest cyclic variations in figure 21 are the same as for sample 11; they should be since the differential delays of the three strongest modes are essentially the same.

Figure 22 shows $\bar{R}_d(0, \Delta t)$ and $\bar{R}_m(0, \Delta t)$ with the magnitude of their difference. The error averages about 0.01, which is excellent. As with sample 11, it is not perfect because of the small RMS least-squares error in the deterministic fit at $k = 6$ in figure 9.

Figure 23 presents plots of the tap-gain correlation functions for the deterministic channel and the statistical channel for path $i = 1$ and the magnitude of their difference. Figures 24, 25, and 26 are similar plots for paths $i = 2$ to 4, respectively. In figure 23 for the 1E mode, path $i = 1$, two magnetoionic components were used in the statistical channel to obtain the least-squares fit of $\bar{C}_{s1}(\Delta t)$ to $\bar{C}_{d1}(\Delta t)$. The error curve shows that while the fit is good over most of the domain, it is not as good between 3 and 25 sec, probably because the effective number of

independent values was only 15, corresponding to the long correlation time. As shown in figures 25, 25, and 26, only a single Gaussian-spectrum component was used in the least-squares fit for the second, third, and fourth paths, $i = 2, 3$, and 4. The error curves in all three cases showed good fits.

The optimum time delays, frequency shifts, and frequency spreads for each path in the statistical channel, as well as similar channel values, are listed in table 6. The resulting tap-gain spectrums for each of the four paths in the statistical channel are presented in figure 27, which shows that the 1E mode had a considerably smaller spread than the F modes, as was the case for sample 11. It is interesting to note that the ratio of the frequency spread on the 2F mode to the frequency spread on the 1F mode is 1.86, and that the ratio of the frequency spreads on the 2F mode to the M mode is 1.01; i.e., they are essentially the same. This may be typical, as the F-layer reflection points for the M mode are geographically close to the F-layer reflection points for the 2F mode, and the E-layer reflection in the M mode contributes negligible spread compared with the F-layer reflections.

A direct measure of the accuracy of the fit of the statistical channel to the measured ionospheric channel for sample 12 was made by comparing $\bar{R}_s(\Delta f, 0)$ with $\bar{R}_m(\Delta f, 0)$ and $\bar{R}_s(0, \Delta t)$ with $\bar{R}_m(0, \Delta t)$. Plots of $\bar{R}_s(\Delta f, 0)$ and $\bar{R}_m(\Delta f, 0)$ and the magnitude of their difference are presented in figure 28, where the accuracy of the fit of the statistical channel is approximately the same as the corresponding fit of the deterministic channel in figure 21, as we would expect. Based on smoothed error values, the statistical fit is excellent to about 2.0 kHz, good to about 4.0 kHz, and adequate to about 8.0 kHz, as it was with the deterministic fit. From averages of values from figure 28 in (95), a rough estimate of the effective time spread on the ionospheric modes, $2\rho_s$, was 30 μ s. When this value is

used in (110), $B = 8.3$ kHz results, which agrees with the above adequate qualitative rating.

Plots of $\bar{R}_d(0, \Delta t)$ and $\bar{R}_n(0, \Delta t)$ for sample I2 are presented in figure 29 with the magnitude of their difference. Unlike $\bar{R}_d(0, \Delta t)$, which is nearly identical to $\bar{R}_n(0, \Delta t)$, $\bar{R}_s(0, \Delta t)$ differs significantly from $\bar{R}_n(0, \Delta t)$ because the tap-gain spectrums in the statistical channel model are restricted to Gaussian functions. Even so, the error curve in figure 29 shows the fit to be adequate over the entire domain and good over most of the domain. However, from (47) at $\Delta f = 0$,

$$R(0, \Delta t) = \sum_{i=1}^n C_i(\Delta t) . \quad (111)$$

Therefore, the small effective number of independent values in the strongest first path, which limited the accuracy of the fit of $\bar{C}_{d1}(\Delta t)$ to $\bar{C}_{d1}(\Delta t)$, also limited the accuracy of the fit of $\bar{R}_s(0, \Delta t)$ to $\bar{R}_n(0, \Delta t)$; the largest error in figure 23 between 3 and 25 sec corresponds to the largest error in figure 29 over the same interval. When figures 28 and 29 are considered together as a measure of the accuracy of the fit of the statistical channel to the measured ionospheric channel, the fit can be rated adequate up to bandwidths of about 9 kHz. However, had the duration of sample I2 been longer, with a corresponding larger effective number of independent values for path $i = 1$ and the channel, the errors in figure 23 and 29 very probably would have been smaller, allowing a good rating for bandwidths up to 4.5 kHz.

Amplitude- and phase-density histograms for each of the tap-gain functions in the deterministic channel, $G_{d1}(t_r)$, were computed and used in chi-square tests of the bivariate Gaussian hypothesis. Figure 30 presents plots of the cumulative distribution of $|G_{d1}(t_r)|$ and figure 31

of the phase-density histograms for $\nabla G_{d1}(t_r)$ for each of the four paths, as well as the lines that represent the corresponding distributions for the statistical channel. The corresponding amplitude and phase distributions of the measured ionospheric channel response, $H_m(f_k, t_r)$, for 11 frequencies, are also presented in the two figures but were not used in the chi-square tests. All amplitude distribution plots in figure 30 were scaled for a channel power ratio $R(0, 0) = 1$. The effective number of independent values for each path, m_{e1} , were 15.0, 191, 355, and 357 for $i = 1$ to 4 respectively (see table 6). For a significance level of 0.1, the resulting normalized values of chi-square for each of the $2n = 8$ distributions are tabulated in table 6. Since all of the computed normalized chi-square values were less than one, we concluded that the bivariate Gaussian hypothesis was valid for all paths.

To test the independence hypothesis, we computed the magnitude of the normalized crosscorrelations between the various deterministic tap-gain functions. The values are listed in table 7. The crosscorrelations for path combinations (1, 3), (1, 4), (2, 4), and (3, 4) were sufficiently large to indicate crosscorrelations, but it appears fairly certain that these indications are false, except possibly for (3, 4), for the following reason: we know that a "cross-talk" condition exists in the multitone method that was used for making ionospheric channel measurements and subsequently obtaining solutions for $\{G_{d1}(t_r)\}$. When any ionospheric mode has a nonzero time spread, the resulting least-squares fit of $H_d(f_k, t_r)$ to $H_m(f_k, t_r)$ will be less than perfect ($|E(f_k, t_r)|$ will be greater than zero), because the deterministic channel model has discrete paths, and errors will appear in the solution for each tap-gain function, $G_{d1}(t_r)$. If we assume that a nonzero time spread occurs on only one of the ionospheric modes, the error in each tap-gain solution at any instant of time will be proportional to the magnitude of that mode, as well as

Table 7. Sample I2 Crosscorrelations

Path Pair	Crosscorrelation
i, l	$ \bar{r}_{il} $
1, 2	1.11
1, 3	3.74
1, 4	2.88
2, 3	0.83
2, 4	1.62
3, 4	5.59

dependent upon the time spread on the mode. Consequently, the error component in each tap-gain solution will vary in time according to the magnitude of the mode with the nonzero time spread; i. e., the error components in the tap-gain solutions for the zero-spread modes will be very highly correlated with the tap-gain function for the mode with the nonzero time spread. If more than one ionospheric mode has a nonzero time spread, components of each tap-gain function will appear in the solutions for the other tap-gain functions to an extent dependent upon the relative strengths of the modes. As a result of this cross-talk, tap-gain solutions for weak modes contain the largest fractional amounts of undesired cross-talk from other paths, and the strongest cross-talk would be from the strongest paths. Since the three highest crosscorrelations in table 7 for sample I2 were between the strongest mode and the two weakest modes, (1, 3) and (1, 4), and between the two weakest modes (3, 4), it appears fairly certain that the high correlation values are caused by the high correlations between the relatively strong common cross-talk components. This probably occurred in sample I2 but not in sample I1 because of the presence of the very weak M mode ($i = 3$) in sample I2, which was not

present in I1, and because the time spread on the modes was greater in sample I2. One might argue that the highest crosscorrelation for path combination (3, 4) may not be entirely fictitious, that the M and 2F modes involved have F-layer reflection points that are not widely separated geographically and that they truly may be correlated to some extent. Unfortunately, the cross-talk effect in the multitone method of obtaining deterministic tap-gain solutions can prevent an accurate determination of the path crosscorrelations when a weak mode is involved, as in this sample. Therefore, because it appeared very probable that the high crosscorrelations in table 7 were caused by cross-talk, we concluded that it was not possible to say whether the assumption of independence between the tap-gain functions was valid or not for this sample.

To test the Gaussian spectrum hypothesis, (109) was used to compute the approximate RMS value of $|\bar{C}_{s1}(\Delta t) - \bar{C}_{d1}(\Delta t)|$ for each path, ϵ_{c1} . For paths $i = 1, 2, 3$, and 4, these values were 0.258, 0.072, 0.053, and 0.053, respectively, as listed in table 6. Since the error curves in figures 23, 24, 25, and 26 were less than these RMS values over all four domains, we concluded the Gaussian spectrum hypothesis was valid for all paths in sample I2.

In concluding the discussion of the sample I2 results, we may note that had fewer tones been used in the deterministic fit (say $k = 4, 5, 6, 7$, and 8 over a 2.0-kHz band, rather than $k = 3, 4, 5, 6, 7, 8$, and 9 over a 3.2-kHz band), the magnitude of the error in the deterministic fit, $|E(f_k, t_r)|$, would have been less at these frequencies. The resulting cross-talk in the deterministic tap-gain functions would have been less, making the crosscorrelation results more reliable. In general, the smaller the bandwidth of the fit, the smaller the error of the fit. There is, however, a lower acceptable limit to the bandwidth occupied by the tones used in a deterministic fit: the minimum bandwidth should not be

much less than half of the reciprocal of the smallest of the differential propagation times between adjacent modes. For sample I2, this would be 2.0 kHz as specified by half of the reciprocal of the 250- μ s differential time delay between paths $i = 1$ and $i = 2$. If this condition is violated too severely, the measurements lack sufficient time resolution to resolve the two closely spaced paths. As a result, additive noise or other errors of measurement will introduce sizable errors in the tap-gain functions for the two closely spaced paths, but the error in one tap-gain function will be the negative of the error in the other so that the time-varying frequency responses for each of the two paths, $G_{d1}(t_r) \exp(-j2\pi f t_r)$, will when summed provide an accurate time-varying frequency response for the pair of paths. Since the other tap-gain functions are still accurate, an accurate channel response, $H_d(f_k, t_r)$, is obtained. Even so, the two closely spaced paths will have tap-gain functions with large highly correlated errors, and statistical analyses of each of them, such as $C_{d1}(\Delta t)$, will have correspondingly large errors, making the results unacceptable.

5.3 Sample I3

The third sample of data, I3, was taken from nighttime measurements on 5.864 MHz on November 10, 1967, from 04:17 to 04:30 MST. During this 13-min interval, the ionosphere supported three modes whose identification is not certain. The time delays of the modes or paths relative to the arbitrary 200-Hz receiver reference were 445, 750, and 1088 μ s. The power ratios for the three paths relative to the power ratio for the channel were - 1.63, - 7.65, and - 8.47 dB, respectively. These data, as well as other pertinent results obtained in the analyses of sample I3, are tabulated in table 8.

Table 8. Summary of Sample I3A Results

Frequency	5.864 MHz
Date	November 10, 1967
Time	04:17 - 04:30 MST; $t_m = 780$ s
Number of paths	$n = 3$
Measurement rate	$f_m = 3.125$ Hz
Actual number of values	$m_a = 2437$
Channel time delay	$\hat{\tau}_s = 589$ μ s
Channel time spread	$2\rho_s = 464$ μ s
Channel frequency shift	$\hat{\nu}_s = 0.110$ Hz
Channel frequency spread	$2\sigma_s = 0.0666$ Hz
Estimate of path time spreads	$2\rho_e = 100$ μ s

Path Values

Path	Time Delay	Rel. Power Ratio	Freq. Shift	Freq. Spread	Eff. Number Values	Correl. Spread	Normalized Chi-square Values
i	τ_i μ s	$\frac{C_{si}(0)}{R_s(0,0)}$ dB	ν_{si} Hz	$2\sigma_{si}$ Hz	m_{ei}	ϵ_{ci}	$\bar{\chi}_{i1}^2, \bar{\chi}_{i2}^2$
1a	445	- 3.8	.0764	.0360	88.3	.107	0.39, 0.08
1b	445	- 5.7	.134	.0320			
1	445	- 1.6	.0989	.0658			
2a	750	-10.8	.121	.0104	30.5	.181	0.47, 0.08
2b	750	-10.6	.141	.0130			
2	750	- 7.7	.131	.0229			
3a	1088	-12.9	.121	.0149	45.4	.148	0.68, 0.11
3b	1088	-10.4	.151	.0206			
3	1088	- 8.5	.140	.0335			

Two deterministic fits of $H_d(f_k, t_r)$ to $H_m(f_k, t_r)$ were made from sample I3 measurements and differed in the number of frequencies that were used in the least-squares fits. The results obtained from these two fits were designated I3A and I3B, respectively. In the first deterministic

fit, I3A, seven central frequencies ($k = 3, 4, 5, 6, 7, 8$, and 9) were used; the RMS error is presented in figure 9. It can be seen that this fit is not as good as those obtained for the same seven frequencies in samples I1 and I2. Since, as with the previous samples, the limitation in the accuracy of the fit is almost entirely due to the discrete-path approximation in the deterministic channel model, the poorer fit indicates that the time spread on the nighttime modes in sample I3 was greater than the time spread on the daytime modes in samples I1 and I2.

We also examined the error in the I3A deterministic fit by comparing $\bar{R}_d(\Delta f, 0)$ with $\bar{R}_m(\Delta f, 0)$ and $\bar{R}_d(0, \Delta t)$ with $\bar{R}_m(0, \Delta t)$. Figure 32 is a plot of $\bar{R}_d(\Delta f, 0)$ and $\bar{R}_m(\Delta f, 0)$ and the magnitude of their difference. We see from the curves that $\bar{R}_m(\Delta f, 0)$ decays more rapidly and the error increases faster with increasing Δf than do the corresponding curves in figures 10 and 21 for the daytime measurements, because of the greater time spread on the modes. If the error curve in figure 32 is smoothed, the deterministic fit for sample I3A can be rated good to about 1.2 kHz and adequate to about 2.4 kHz. The major oscillation in figure 32 has a period of about 3.3 kHz, which agrees with the reciprocal of the difference of the time delays of the first and second paths, 305 μ s. The 643- μ s differential propagation time between the first and third modes produces the oscillation with a period of 1.55 kHz in figure 32.

Figure 33 shows $\bar{R}_d(0, \Delta t)$ and $\bar{R}_m(0, \Delta t)$ for sample I3A with the magnitude of their difference. The error in the fit is not nearly as good as the corresponding results for samples I1 and I2 in figures 11 and 22, because of the greater error in the deterministic fit at $k = 6$ in figure 9.

Figure 34 presents plots of the tap-gain correlation functions in the deterministic channel and the statistical channel for path $i = 1$ in sample I3A and the magnitude of their difference. Figures 35 and 36 are similar plots for paths $i = 2$ and $i = 3$. For each of the three paths, two magneto-ionic components were used in the statistical channel to obtain the

least-squares fit of $\bar{C}_{s1}(\Delta t)$ to $\bar{C}_{d1}(\Delta t)$. Figures 34 and 35 show that the fits for paths one and two are excellent. The error for the third path in figure 36 is rather large between 3 and 10 s; it is very probably caused by cross-talk from the strong first path that has a correlation time in figure 34 of about 10 s.

The optimum time delays, frequency shifts, and frequency spreads for each path in the statistical channel, as well as similar channel values, are listed in table 8 for sample I3A. The resulting tap-gain spectrums for each of the three paths in the statistical channel are presented in figure 37. For each path the power ratios and frequency spreads on the two magnetoionic components are approximately the same and that their differential frequency shifts are somewhat greater than their frequency spreads.

A direct measure of the accuracy of the fit of the statistical channel to the measured ionospheric channel for sample I3A was made by comparing $\bar{R}_s(\Delta f, 0)$ with $\bar{R}_m(\Delta f, 0)$ and $\bar{R}_s(0, \Delta t)$ with $\bar{R}_m(0, \Delta t)$. Plots of $\bar{R}_s(\Delta f, 0)$ and $\bar{R}_m(\Delta f, 0)$ with the magnitude of their difference are presented in figure 38. The accuracy of the fit of the statistical channel in figure 38 is very nearly the same as the corresponding fit of the deterministic channel in figure 32, as one would expect; based on smoothed error values, the statistical fit is good to about 1.2 kHz and adequate to about 2.4 kHz, as it was in the deterministic fit. From averages of values from figure 38 in (95), a rough estimate of the time spread on the ionospheric modes was 100 μ s. When this value is used in (110), $B = 2.5$ kHz results, which agrees with the above adequate qualitative rating.

Plots of $\bar{R}_d(0, \Delta t)$ and $\bar{R}_m(0, \Delta t)$ are shown in figure 39 with the magnitude of their difference. In previous samples, I1 and I2, $\bar{R}_s(0, \Delta t)$ fit $\bar{R}_m(0, \Delta t)$ less accurately than $\bar{R}_d(0, \Delta t)$ fit $\bar{R}_m(0, \Delta t)$, because the tap-gain spectrums in the statistical channel were restricted to Gaussian functions,

while the deterministic tap-gain spectrums were unrestricted. In sample I3A, however, the larger time spreads on the modes resulted in greater error in the fit of $\bar{R}_d(0, \Delta t)$ to $\bar{R}_m(0, \Delta t)$ (see fig. 33). Thus, the fit of $\bar{R}_s(0, \Delta t)$ to $\bar{R}_m(0, \Delta t)$ in figure 39 is not poorer than figure 33; it is somewhat better. When figures 38 and 39 are both considered as a measure of the accuracy of the fit of the statistical channel to the measured ionospheric channel, the fit can be rated as good up to 1.2 kHz and adequate up to 2.4 kHz. It is considerably more limited in bandwidth than samples I1 and I2 because of the greater time spread on the ionospheric modes.

Amplitude- and phase-density histograms for each of the tap-gain functions in the deterministic channel, $G_{di}(t_r)$, were computed and used in chi-square tests of the bivariate Gaussian hypothesis for sample I3A. Figure 40 presents plots of the cumulative distribution of $|G_{di}(t_r)|$ and figure 41 of the phase-density histograms for $\angle G_{di}(t_r)$ for each of the three paths, as well as lines for the corresponding distributions for the statistical channel. The corresponding amplitude and phase distributions of the measured ionospheric channel response, $H_m(f_k, t_r)$, for all 11 frequencies, are also presented in the two figures but were not used in the chi-square tests. All amplitude distribution plots in figure 40 were scaled for a channel power ratio $R(0, 0) = 1$. The effective number of independent values used for each path in the chi-square calculations were 88.3, 30.5, and 45.4 for $i = 1$ to 3, respectively (see table 8). For a significance level of 0.1, all the resulting normalized values of chi-square for each of the $2n = 6$ distributions (also tabulated in table 8) were less than one. We therefore concluded that the bivariate Gaussian hypothesis was valid for all paths.

To test the independence hypothesis for sample I3A, the magnitude of the normalized crosscorrelations among the various deterministic tap-gain functions were computed and are listed in table 9. The probability

of one or more of the three being greater than one is 0.27 when the paths are truly independent. In addition, the normalized crosscorrelation for path combination (2, 3) was between the two weakest paths and, even though neither of these paths was extremely weak, the time spread on the modes was very large and it appeared fairly certain that the high correlation was partly the result of cross-talk. We therefore concluded that the modes in sample I3A were uncorrelated and, because they were shown to be bivariate Gaussian random functions, also independent.

Table 9. Sample I3A Crosscorrelations

Path Pair	Crosscorrelation
i, l	$ \bar{\Gamma}_{il} $
1, 2	0.95
1, 3	0.97
2, 3	1.39

To test the Gaussian spectrum hypothesis, (109) was used to compute the approximate RMS values of $|\bar{C}_{ei}(\Delta t) - \bar{C}_{df}(\Delta t)|$ for each path e_{ci} . For paths $i = 1, 2$, and 3 , these values were 0.107 , 0.181 , and 0.148 , respectively, as listed in table 8. Since the error curves for the first two paths in figures 34 and 35 were less than these RMS values and the error curve for the third path in figure 36 exceeded the RMS value only slightly between 3 and 10 sec, we concluded the Gaussian spectrum hypothesis was valid for all three paths in sample I3A.

Because the deterministic fit of $H_d(f_k, t_r)$ to $H_e(f_k, t_r)$ in sample I3A resulted in relatively large RMS errors, as shown in figure 9, a second fit based on fewer frequencies was made to verify that the error would

be reduced and that the fit of $\bar{R}_d(0, \Delta t)$ to $\bar{R}_m(0, \Delta t)$ would be much better. Five central frequencies ($k = 4, 5, 6, 7$, and 8) were used for the second least-squares fit of $H_d(f_k, t_r)$ to $H_m(f_k, t_r)$. The resulting RMS error at the various frequencies is shown in figure 9 as plot I3B. The error at the central five tones used in the fit in I3B is much lower than the error obtained in the seven-tone fit, I3A, as expected. Although not included in this report, computations and plots were also made of $\bar{R}_d(\Delta f, 0)$ with $\bar{R}_m(\Delta f, 0)$ and $\bar{R}_d(0, \Delta t)$ with $\bar{R}_m(0, \Delta t)$ for I3B. The magnitude of the difference between $\bar{R}_d(\Delta f, 0)$ and $\bar{R}_m(\Delta f, 0)$ was considerably smaller below $\Delta f = 2.5$ kHz for I3B than for I3A in figure 32, and somewhat smaller above this frequency. The magnitude of the difference between $\bar{R}_d(0, \Delta t)$ and $\bar{R}_m(0, \Delta t)$ was an order of magnitude less for I3B than for I3A in figure 33; as with I1 and I2, this error averaged about 0.01 over the domain. A time limitation prevented additional analyses on sample I3B; however, had such analyses been done, the comparison of the statistical channel with the measured ionospheric channel probably would have resulted in somewhat lower errors than were obtained for I3A in figures 38 and 39.

6. CONCLUSIONS

An experimental study of the validity and accuracy of a proposed stationary ionospheric communication channel model has been described. Reasons for selecting the proposed channel model have been discussed and methods presented of mathematically characterizing time-varying channels in general and the proposed channel model in particular.

The proposed channel model incorporates a delay line fed by the input (transmitted) signal. Undistorted delayed versions of the input signal are delivered at a limited number of adjustable taps on the delay

line, with delays corresponding to the relative propagation times of typical ionospheric modes. Each delayed signal is multiplied by an independent baseband complex bivariate Gaussian random function with a zero mean value and quadrature components having equal RMS values that produce Rayleigh fading. In general, each random tap-gain function has a spectrum that is the sum of two Gaussian functions with different adjustable magnitudes, frequency shifts, and frequency spreads. The two Gaussian spectrum components represent the two magnetoionic components present in ionospheric modes. A single Gaussian spectrum can be used when the magnetoionic components have essentially equal frequency shifts and frequency spreads. The delayed and multiplied signals are summed to form the output (received) signal.

Various experimental techniques were considered, and a description was given of the method and specially designed equipment for obtaining ionospheric channel measurements over a 1294-km midlatitude path at two high frequencies. Measurements from three periods or samples of 10- to 13-min duration were analyzed to determine the validity and accuracy of the stationary channel model under typical daytime and nighttime propagation conditions. The purpose of the analyses was to determine the validity of (a) the bivariate Gaussian hypothesis, (b) the hypothesis of independence between the tap-gain functions, and (c) the Gaussian spectrum hypothesis for the tap-gain spectrums; and to determine the accuracy and bandwidth limitation that is imposed on the channel model by nonzero time spreads on the ionospheric modes, which are approximated by the discrete paths in the channel model. Based on the statistical tests, we concluded that the bivariate Gaussian, independence, and Gaussian spectrum hypotheses were valid, confirming the validity of the proposed ionospheric channel model. We also showed in all three samples that the bandwidth over which the channel model is reasonably

accurate is about one-fourth of the reciprocal of the effective time spread on the ionospheric modes.

For the samples analyzed, tap-gain functions with single-Gaussian spectrums could accurately model daytime 1F, M, and 2F modes and such modes had frequency shifts (positive or negative) up to 0.2 Hz with two-sigma frequency spreads from 0.1 to 0.4 Hz. In both daytime samples, the 1E mode required tap-gain functions with double-Gaussian spectrums for the frequency-separated magnetoionic components, where the frequency shifts on the magnetoionic components ranged up to 0.02 Hz and the two-sigma frequency spreads fell between 0.005 and 0.05 Hz. All modes in the one sample of nighttime measurements required tap-gain functions with double-Gaussian spectrums, where the shifts on the magnetoionic components ranged up to 0.2 Hz, and the two-sigma frequency spreads were between 0.01 and 0.1 Hz. The estimated effective time spreads on the modes during the daytime were about 25 μ s, which limited the channel model to a bandwidth of about 10 kHz. For the nighttime sample, the effective modal time spreads were about 100 μ s, which limited the channel model bandwidth to about 2.5 kHz.

A set of recommended specifications for ionospheric channel simulators based on this model is presented in appendix E.

7. ACKNOWLEDGMENTS

The authors are greatly indebted to L. J. Demmer and C. H. Johnson for their help in constructing and testing the propagation-measuring equipment and to D. H. Layton and L. J. Demmer for their assistance in the propagation measurements. We also appreciate the many helpful criticisms provided by R. G. Gallager, E. L. Crow, W. M. Beery, and T. deHaas during their reviews of the report and are grateful for the support and encouragement provided by W. H. Dix and E. Weinberger of the Defense Communications Agency.

8. REFERENCES

- Balser, M., and W. B. Smith (1962), Some statistical properties of pulsed oblique HF ionospheric transmissions, *Radio Sci.* 66D, No. 6, 721-730.
- Bello, P. A., and B. D. Nelin (1962), The influence of fading spectrum on the binary error probabilities of incoherent and differentially coherent matched filter receivers, *IRE Trans. Comm. Systems* CS-10, No. 2, 160-168.
- Bello, P. A. (1963), Characterization of randomly time-variant linear channels, *IEEE Trans. Comm. Systems* CS-11, No. 4, 360-393.
- Bendat, J. S., and A. G. Piersol (1966), Measurement and analysis of random data, 146-150, 192-195, 264-267 (John Wiley & Sons, Inc., New York, N. Y.).
- Boys, J. T. (1968), Statistical variations in the apparent specular component of ionospherically reflected radio waves, *Radio Sci.* 3, No. 10, 984-990.
- Bray, W. J., H. G. Lillicrap, and F. C. Owen (1947), The fading machine and its use for the investigation of the effects of frequency-selective fading, *J. Inst. Elec. Eng. (London)* 94, Pt. IIIA, 283-297.
- Clarke, K. K. (1965), Random channel simulation and instrumentation, *Conf. Record, First IEEE Ann. Comm. Conv.*, Boulder, Colorado, 623-629.
- Coon, R. M., E. C. Bolton, and W. D. Bensema (1969), A simulator for HF atmospheric radio noise, *ESSA Tech. Rept. ERL 128-ITS 90*. (U.S. Government Printing Office, Washington, D.C.)
- Crout, P. D. (1941), A short method for evaluating determinants and solving systems of linear equations with real or complex coefficients, *Trans. AIEE* 60, 1235-1240.
- Davies, K. (1962), The measurement of ionospheric drifts by means of a Doppler shift technique, *J. Geophys. Res.* 67, No. 12, 4909-4913.
- DCA (1963), DCS engineering-installation standards manual, sec. 3.2.2.2, Defense Communications Agency, Washington, D.C.

- Essex, E. A., and F. H. Hibberd (1967), Auto-correlation of the fading of multiple echoes from the ionosphere, J. Atmosph. Terr. Phys. 29, 1025-1027.
- Freudberg, R. (1965), Laboratory simulator for frequency selective fading, Conf. Record, First IEEE Ann. Comm. Conv., Boulder, Colorado, 609-614.
- Gallager, R. G. (1964), Characterization and measurement of time- and frequency-spread channels, Tech. Rept. 352, Lincoln Laboratory, M. I. T., 1-34.
- Goldberg, B., R. L. Heyd, and D. Pochmerski (1965), Stored ionosphere, Conf. Record, First IEEE Ann. Comm. Conv., Boulder, Colorado, 619-622.
- Hagfors, T. (1961), Some properties of radio waves reflected from the moon and their relation to the lunar surface, J. Geophys. Res. 66, 777-785.
- Hildebrand, F. B. (1956), Introduction to numerical analysis, 378-382 (McGraw-Hill Book Co., New York).
- Kailath, T. (1961), Channel characterization: time-variant dispersive channels, Lectures on Communication Systems Theory, ed.: E. J. Baghdady, 95-123 (McGraw-Hill Book Co., New York).
- Klein, M. S. (1968), Synthetic HF environment, Final Rept., Contract No. F20602-67-C-0162, Rome Air Development Center, Rome, N. Y., 1-27.
- Law, H. B., F. J. Lee, R. C. Looser, and F. A. W. Levett (1957), An improved fading machine, Proc. IEE 104, Part B, 117-147.
- Nakagami, M. (1940), Study on the resultant amplitude of many vibrations whose phases and amplitudes are random, Nippon Elec. Commun. Eng. (Japan) 22, 69-92.
- Quincy, E. A. (1968), Channel simulation - digital vs. analog, ESSA Tech. Rept. ERL 70-ITS 60, 1-24 (U.S. Government Printing Office, Washington, D. C.).

- Rice, S. O. (1944), Mathematical analysis of random noise, Bell System Tech. J. 23, 282-332; also same journal (1945) 24, 46-156.
- Ross, A. H., and H. F. Meyer (1948), Design and application of a multipath simulator, Eng. Rept. No. E-1025, Signal Corps Engineering Laboratories, Fort Monmouth, N. J., 1-19.
- Sherman, H. (1961), Channel characterization: rapid multiplicative perturbations, Lectures on Communication Systems Theory, ed.: E. J. Baghdady, 71-73 (McGraw-Hill Book Co., New York).
- Siddiqui, M. M. (1964), Statistical inference for Rayleigh distributions, Radio Sci. 68D, No. 9, 1005-1010.
- Walker, W. F. (1965), A simple baseband fading multipath channel simulator, Conf. Record, First IEEE Ann. Comm. Conv., Boulder, Colorado, 615-617. (Also pub. in 1966 in Radio Sci. 1, No. 7, 763-767.)
- Watterson, C. C., G. G. Ax, L. J. Demmer, and C. H. Johnson (1969), An ionospheric channel simulator, ESSA Tech. Memo. ERLTM-ITS 198.
- Watterson, C. C., and R. M. Coon (1969), Recommended specifications for ionospheric channel and atmospheric noise simulators, ESSA Tech. Rept. ERL 127-ITS 89. (U. S. Government Printing Office, Washington, D. C.)
- Zimmerman, M. S., and J. H. Horwitz (1967), A flexible transmission channel simulator, Digest, 1967 IEEE Int. Conf. on Communication, Minneapolis, Minn., 73.

APPENDIX A

Least-Squares Deterministic Fit

The least-squares method that was used to deterministically fit $H_d(f_k, t_r)$ to $H_m(f_k, t_r)$ was applied repeatedly at a regular rate at times t_r , as defined by (70). Therefore, for the present analysis, let the time notation be dropped and for any time, t_r , let

$$H_m(k) = H_m(f_k, t_r) , \quad (112)$$

$$H_d(k) = H_d(f_k, t_r) , \quad (113)$$

$$E(k) = E(f_k, t_r) , \quad (114)$$

$$G_{d1} = G_{d1}(t_r) , \quad (115)$$

$$Z_1(k) = \exp(-j2\pi t_1 f_k) . \quad (116)$$

Using these definitions in (71) and (72), we have

$$E(k) = \sum_{i=1}^n G_{d1} Z_1(k) - H_m(k) . \quad (117)$$

Now define

$$\delta_1 = \sum_k \operatorname{Re}^2 E(k) , \quad (118)$$

$$\delta_2 = \sum_k \operatorname{Im}^2 E(k) , \quad (119)$$

where the summations over "k" mean summations over the frequencies used in the fit - not necessarily all 11 frequencies.

To obtain a fit in an unconventional way, let δ_1 be differentiated with respect to $\text{Re} G_{d\ell}$, let δ_2 be differentiated with respect to $\text{Im} G_{d\ell}$ and set the results equal to zero to obtain

$$\begin{aligned} \sum_{i=1}^n \text{Re } G_{di} \sum_k \text{Re } Z_i(k) \text{Re } Z_\ell(k) \\ - \sum_{i=1}^n \text{Im } G_{di} \sum_k \text{Im } Z_i(k) \text{Re } Z_\ell(k) = \sum_k \text{Re } H_\pi(k) \text{Re } Z_\ell(k), \end{aligned} \quad (120)$$

$$\ell = 1, 2, \dots, n,$$

and

$$\begin{aligned} \sum_{i=1}^n \text{Re } G_{di} \sum_k \text{Im } Z_i(k) \text{Re } Z_\ell(k) \\ + \sum_{i=1}^n \text{Im } G_{di} \sum_k \text{Re } Z_i(k) \text{Re } Z_\ell(k) = \sum_k \text{Im } H_\pi(k) \text{Re } Z_\ell(k), \end{aligned} \quad (121)$$

$$\ell = 1, 2, \dots, n.$$

Then (120) and (121) are each sets of "n" equations, one for each value of " ℓ " in each set. Together they are a set of $2n$ linear equations in $2n$ unknown quantities, the "n" values of $\text{Re } G_{di}$ and the "n" values of $\text{Im } G_{di}$. For each time, t_r , the $2n$ equations were solved simultaneously on the basis of the Crout algorithm (Crout, 1941) and the solutions were combined to form the "n" values of $G_{di}(t_r)$.

The above least-squares method is not conventional, since the derivatives of $\sum_k |E(k)|^2$ were not taken with respect to $\text{Re } G_{di}$ and

Im G_{41} to form $2n$ equations for simultaneous solution, but it resulted in considerably simpler equations, and computer tests of the method showed the fits to be comparable to those obtained by the more involved conventional method.

APPENDIX B

Least-Squares Statistical Fit

For each path in each sample, a least-squares fit of $C_{s1}(\Delta t)$ to $C_{d1}(\Delta t)$ was made in the following manner. Let

$$\delta_{s1} \equiv \sum_{l=1}^{m_{c1}} |\bar{C}_{s1}(lct_m/m_a) - \bar{C}_{d1}(lct_m/m_a)|^2, \quad (122)$$

where

c = integer controlling abscissa spacing of values, and
 m_{c1} = number of values used in the least-squares fit,

and where, from (65), (84), and (67),

$$\bar{C}_{s1}(\Delta t) = \left\{ \begin{aligned} & [C_{s1a}(0)/C_{s1}(0)] \exp(-2\pi^2 \sigma_{s1a}^2 \Delta t^2 + j2\pi \nu_{s1a} \Delta t) \\ & + [1 - C_{s1a}(0)/C_{s1}(0)] \exp(-2\pi^2 \sigma_{s1b}^2 \Delta t^2 + j2\pi \nu_{s1b} \Delta t) \end{aligned} \right\} \quad (123)$$

and

$$C_{s1b}(0)/C_{s1}(0) = [1 - C_{s1a}(0)/C_{s1}(0)] . \quad (124)$$

Optimum values of ν_{s1a} , ν_{s1b} , σ_{s1a} , σ_{s1b} , and $C_{s1a}(0)/C_{s1}(0)$ were then defined as those values that would minimize (122). However, if (123) is substituted in (122) and the result is differentiated with respect to the five unknowns, ν_{s1a} , ν_{s1b} , σ_{s1a} , σ_{s1b} , and $C_{s1a}(0)/C_{s1}(0)$, with the derivatives being set equal to zero in each case, the resulting five simultaneous equations are nonlinear and do not lend themselves to analytic solutions. A program was therefore written for a time-sharing computer that computed numerical values of δ_{s1} given numerical values of the five unknowns and computed values of $C_{d1}(\Delta t)$. Typical values of $15 < m_c < 20$ were used with the integer "c" chosen to use values of $C_{d1}(\Delta t)$ over the significant portion of its domain. (The values of Δt that were used in

the least-squares computations are plotted as data points in the various figures that present plots of $C_{d1}(\Delta t)$ and $C_{s1}(\Delta t)$. Initial values of the five unknowns that approximated the optimum values were obtained by examining the amplitude and phase plots of $C_{d1}(\Delta t)$; approximate values of the frequency shifts, ν_{s1a} and ν_{s1b} , were obtained from $C_{d1}(\Delta t)$, and the approximate values of σ_{s1a} , σ_{s1b} , and $C_{s1a}(0)/C_{s1}(0)$ were obtained from $|C_{d1}(\Delta t)|$. Starting with the initial approximations, solutions for δ_{s1} were obtained for a number of equally spaced values of ν_{s1a} that bracketed the initial approximation. Keeping that value of ν_{s1a} that provided a minimum value of δ_{s1} , the procedure was repeated for each of the other four unknown values. The entire process was then repeated several times until sufficiently accurate estimates of the optimum values of the five unknowns had been obtained. From (124), $C_{s1b}(0)/C_{s1}(0)$ was then obtained; since $C_{s1}(0)$ was known from (85), numerical values for $C_{s1a}(0)$ and $C_{s1b}(0)$ followed.

Where only one magnetoionic component was used for a path in the statistical model, the number of unknowns was reduced to two, and the process was quicker. Even for five unknowns, however, accurate estimates could be obtained rather quickly. Since relatively few sets of solutions were required, no attempts were made to prepare a more involved computer program that could iteratively obtain the same results.

APPENDIX C

Effective Number of Independent Values

Because successive values of each deterministic tap-gain function, $G_{di}(t_r)$, were highly correlated in each of the three samples, it was necessary to compute an effective number of independent values. For each path, the effective number of independent values was used in the chi-square tests of the bivariate Gaussian hypothesis, crosscorrelation tests of the independence hypothesis, and a test of the Gaussian spectrum hypothesis.

For any path with a normalized tap-gain correlation function, $\bar{C}_{di}(\Delta t)$, the effective number of independent values, m_{ei} , would equal the actual number, m_a , if successive values were spaced by an amount greater than the time required for the correlation function to fall essentially to zero. As the adjacent time spacing of the values is decreased, however, causing the correlation between successive values to increase above zero, the effective number of independent values becomes less than the actual number of values. As the adjacent spacing is reduced to a fraction of the decay time of the correlation function, the effective number of independent values approaches a constant limit. For any fixed measurement time, t_m , this limit is inversely proportional to the decay time of the tap-gain correlation function and, therefore, directly proportional to the effective bandwidth of the tap-gain spectrum. One can define B_{ei} , the effective bandwidth of the tap-gain spectrum for the i -th path, in terms of m_{ei} with

$$m_{ei} = 2B_{ei}t_m \quad (125)$$

The factor of two is included to make B_{ei} correspond to the conventional method of defining bandwidth in terms of the width of the positive half of

the spectrum. Now it is necessary to specify B_{e1} in terms of the normalized tap-gain spectrum parameters.

Siddiqui (1964) considered the problem of the effective number of independent values for random functions and used an equation that he considered a reasonably good estimate of the effective number of values. With the notation used here, this equation is

$$m_{e1} = m_a \left[\sum_{l=-\infty}^{\infty} \bar{\kappa}^2(l/f_m) \right]^{-1}, \quad (126)$$

where $\bar{\kappa}(\Delta t)$ is the normalized real correlation function of a random function, and $1/f_m$ is the time spacing of successive values. To apply this equation to the present case, let each normalized tap-gain correlation function in the statistical channel, $\bar{C}_{s1}(\Delta t)$, be used as an approximation of the corresponding tap-gain correlation function in the deterministic channel, $\bar{C}_{d1}(\Delta t)$. To keep the analysis simple, let the normalized tap-gain spectrum, $v_{s1}(\nu)$, be restricted to a function with even symmetry about $\nu = 0$. This implies that $v_{s1}(\nu)$ has a frequency shift of zero and that its two Gaussian magneto-ionic components have equal power ratios, frequency shifts of the same magnitude but opposite sign, and equal frequency spreads. Specifically, the restrictions are

$$v_{s1} = 0, \quad (127)$$

$$C_{s1a}(0) = C_{s1b}(0), \quad (128)$$

$$v_{s1a} = -v_{s1b}, \quad (129)$$

$$\sigma_{s1a} = \sigma_{s1b}. \quad (130)$$

From (65) and (84), it follows that

$$\bar{C}_{s1}'(\Delta t) = \exp(-2\pi^2 \sigma_{s1a}^2 \Delta t^2) \cos(2\pi v_{s1a} \Delta t), \quad (131)$$

where the prime indicates that restrictions (127) through (130) apply. Because of these restrictions, the tap-gain correlation function in (131) is real. Now let it replace $\bar{\kappa}(\Delta t)$ in (126) and let the numerator and denominator both be multiplied by $(t_m/m_a) = (1/f_m)$ to give

$$m_{e1} = t_m \left[\sum_{\ell=-\infty}^{\infty} \bar{C}_{s1}'^2(\ell t_m/m_a) t_m/m_a \right]^{-1}. \quad (132)$$

In computing each $\bar{C}_{s1}'(\Delta t)$, successive values of $G_{s1}(t_r)$ had spacings that were a small fraction of the decay time of $\bar{C}_{s1}'(\Delta t)$. Consequently, since $\bar{C}_{s1}'(\Delta t)$ is being used as an approximation of $\bar{C}_{s1}(\Delta t)$, the summation in (132) can be replaced by an integral with good accuracy to give

$$m_{e1} = t_m \left[\int_{-\infty}^{\infty} \exp(-4\pi^2 \sigma_{s1a}^2 \Delta t^2) \cos^2(2\pi v_{s1a} \Delta t) d\Delta t \right]^{-1}. \quad (133)$$

Equation (133) can be integrated to obtain

$$m_{e1} = (4\sqrt{\pi} \sigma_{s1a} t_m) [1 + \exp(-v_{s1a}^2/\sigma_{s1a}^2)]^{-1}. \quad (134)$$

Note from (125) and (134) that

$$B_{e1} = (2\sqrt{\pi} \sigma_{s1a}) [1 + \exp(-v_{s1a}^2/\sigma_{s1a}^2)]^{-1}. \quad (135)$$

As seen from (135), B_{e1} varies from $\sqrt{\pi} \sigma_{s1a}$ when the two magnetoionic components have spectrums that are completely overlapped to $2\sqrt{\pi} \sigma_{s1a}$ when their frequency shifts are large compared to their frequency spreads. Equation (135) can also be derived by using the tap-gain spectrum corresponding to (131) in the definition for equivalent statistical bandwidth given by Bendat and Piersol (1966) in their equation 6.40c.

Had restriction (127) not been imposed, the normalized correlation function in (131) would have had an additional factor of $\exp(j2\pi \nu_{s1} \Delta t)$, causing $\bar{C}_{s1}'(\Delta t)$ to be complex with a linear phase component. In this case, $|C_{s1}'(\Delta t)|$ could have been substituted in (126) to obtain the same results in (134). Since the presence or absence of a frequency shift, ν_{s1} , in a tap-gain spectrum does not change the amplitude distribution of the tap-gain function, (134) is a reasonable estimate to use in the chi-square tests on the amplitude-density histograms for each deterministic tap-gain function (even though condition (127) is not met), provided restrictions (128) through (130) hold. However, it is not reasonable to apply (134) to chi-square tests of the phase-density histograms unless restriction (127) is also met. If the tap-gain spectrum, $\nu_{s1}(\nu)$, has a sizable frequency shift, this will have been brought about by a correspondingly large linear phase component in the tap-gain correlation function, $\bar{C}_{s1}(\Delta t)$, as specified by (56). Because $\bar{C}_{s1}(\Delta t)$ is a reasonably accurate approximation of $\bar{C}_{d1}(\Delta t)$, the phase component of the deterministic tap-gain function, $G_{d1}(t_r)$, also has an appreciable linear component. This will cause $G_{d1}(t_r)$ to move over a 2π interval more rapidly than it would without the linear phase component, causing the effective number of values to be greater. Therefore, restriction (127) was imposed in order that m_{s1} might also be used as a reasonable estimate of the number of independent values in the chi-square tests of the phase-density histograms of the deterministic tap-gain functions. Because $G_{d1}(t_r)$ always had a linear phase component, and quite often a sizable one, $G_{d1}(t_r)$ had to be modified to meet the restriction in (127). Specifically,

$$G_{d1}'(t_r) = G_{d1}(t_r) \exp(-j2\pi \nu_{s1} t_r) \quad (136)$$

was computed to obtain a modified deterministic tap-gain function whose spectrum had essentially zero frequency shift. The phase-density histograms were then computed from $G_{d1}'(t_r)$.

While restriction (127) was satisfied in the computation of $G'_{d1}(t_r)$, restrictions (128) through (130) remain unsatisfied. For those paths requiring only a single Gaussian component in the tap-gain spectrum, $v_{s1}(v)$, restrictions (128) through (130) did not apply. For the remaining paths, where two magnetoionic components were used in the statistical fit of $\bar{C}_{s1}(\Delta t)$ to $\bar{C}_{d1}(\Delta t)$, the power ratios and frequency spreads were usually comparable, making (130) approximately true after the removal of v_{s1} via (136). Therefore,

$$v_{sie} = [(v_{s1} - v_{s1a})(v_{s1b} - v_{s1})]^{\frac{1}{2}} \quad (137)$$

and

$$\sigma_{sie} = (\sigma_{s1a} \sigma_{s1b})^{\frac{1}{2}} \quad (138)$$

were used as averages to replace v_{s1a} and σ_{s1a} , respectively, in (134) to obtain

$$m_{e1} = (4\sqrt{\pi} \sigma_{sie} t_m) [1 + \exp(-v_{sie}^2 / \sigma_{sie}^2)]^{-1} . \quad (139)$$

Equation (139) was used as an estimate of the effective number of independent values in the chi-square tests of the bivariate Gaussian hypothesis, crosscorrelation tests of the independence hypothesis, and tests of the Gaussian spectrum hypothesis.

APPENDIX D

Tests of Correlation Estimates

To test the validity of the Gaussian spectrum hypothesis for each tap-gain spectrum, a rough measure was obtained of the distribution that $|\bar{C}_{s1}(\Delta t) - \bar{C}_{d1}(\Delta t)|$ would have for a large number of samples under the same ionospheric channel conditions when the hypothesis was true. Also, to test the validity of the hypothesis that the tap-gain functions were independent, an analysis was made to determine the distribution that $|\Gamma_{12}|$ would have for a large number of independent bivariate Gaussian tap-gain functions. Derivations for these two distributions are presented below.

To derive the distribution that $|\bar{C}_{s1}(\Delta t) - \bar{C}_{d1}(\Delta t)|$ would have for a large number of samples, it is necessary to assume that the bivariate Gaussian hypothesis has been shown to be valid and also to derive the distribution in terms of independent quadrature components in the tap-gain functions. However, the quadrature components of a bivariate Gaussian tap-gain function are not independent unless the tap-gain spectrum has even symmetry about $\nu = 0$. As discussed in appendix C, this condition can be approximated quite well for any path when the magneto-ionic components have approximately equal power ratios and frequency spreads if the linear phase component in the deterministic tap-gain function is removed according to (136). Equation (136) can be rewritten as

$$G_{d1}(t_r) = G'_{d1}(t_r) \exp(j2\pi\nu_{s1}t_r), \quad (140)$$

where the quadrature components of $G'_{d1}(t_r)$ are effectively independent. Substitute (140) in (82) to obtain

$$C_{d1}(\Delta t) = \exp(j2\pi v_{s1}\Delta t) \frac{1}{m_a'} \sum_{r=1}^{m_a'} G_{d1}^{I*}(t_r) G_{d1}^I(t_r + \Delta t) . \quad (141)$$

If $C_{d1}(\Delta t)$ is defined as the autocorrelation of $G_{d1}^I(t_r)$ according to (82), then (141) becomes

$$C_{d1}(\Delta t) = \exp(j2\pi v_{s1}\Delta t) C_{d1}^I(\Delta t) . \quad (142)$$

To describe the tap-gain and correlation functions in terms of their real and imaginary (quadrature) components, define

$$G_{d1}^I(t_r) = \underline{g}_{d1}^I(t_r) + j \underline{\underline{g}}_{d1}^I(t_r) \quad (143)$$

and

$$C_{d1}^I(\Delta t) = \underline{c}_{d1}^I(\Delta t) + j \underline{\underline{c}}_{d1}^I(\Delta t) , \quad (144)$$

where the single and double bars under the functions indicate real and imaginary components, respectively.

Using normalized values as defined by (80), substitute (143) in (141), perform the multiplication, and equate the real and imaginary parts of the resulting summation to their counterparts in (144) to obtain

$$\underline{\underline{c}}_{d1}^I(\Delta t) = \frac{1}{m_a'} \sum_{r=1}^{m_a'} [\underline{\bar{g}}_{d1}^I(t_r) \underline{\bar{g}}_{d1}^I(t_r + \Delta t) + \underline{\underline{\bar{g}}}_{d1}^I(t_r) \underline{\underline{\bar{g}}}_{d1}^I(t_r + \Delta t)] \quad (145)$$

and

$$\underline{\underline{c}}_{d1}^I(\Delta t) = \frac{1}{m_a'} \sum_{r=1}^{m_a'} [\underline{\bar{g}}_{d1}^I(t_r) \underline{\underline{\bar{g}}}_{d1}^I(t_r + \Delta t) - \underline{\underline{\bar{g}}}_{d1}^I(t_r) \underline{\bar{g}}_{d1}^I(t_r + \Delta t)] , \quad (146)$$

where the bars above the functions indicate normalized values.

Under the condition that $\bar{G}_{d1}(t_r)$ has been shown to be a bivariate Gaussian random function, each of the components $\bar{g}_{d1}^I(t_r)$ and $\bar{g}_{d1}^{II}(t_r)$ are independent real Gaussian functions with zero mean values, RMS values of $1/\sqrt{2}$, and identical spectrums. Each of the two summations in (145) and the two summations in (146) are estimates of autocorrelations or crosscorrelations of the independent quadrature components of $\bar{G}_{d1}(t_r)$. While each term in each summation has a non-Gaussian distribution, this is not true for the summation. The effective number of independent values in each summation, m_{e1} from appendix C, is sufficiently large to allow the central limit theorem to apply and each summation has a distribution that is very nearly Gaussian. The variances of the summations can be conservatively approximated from (Bendat and Piersol, 1966)

$$\text{Var} [\tilde{c}_1(\Delta t)] \approx \frac{1}{2\tilde{B}t_m} [c_1^2(0) + c_1^2(\Delta t)] \quad (147)$$

and

$$\text{Var}[\tilde{c}_{12}(\Delta t)] \approx \frac{1}{2\tilde{B}t_m} [c_1(0) c_2(0) + c_{12}^2(\Delta t)] , \quad (148)$$

where $\tilde{c}_1(\Delta t)$ is an estimate of an autocorrelation function and $c_1(\Delta t)$ is the true correlation function. Similarly, $\tilde{c}_{12}(\Delta t)$ is an estimate of a crosscorrelation function and $c_{12}(\Delta t)$ is the true crosscorrelation function. Both functions that are correlated have spectrums with a common bandwidth, \tilde{B} .

Apply (147) to the two summations in (145), each of which is an estimate of an autocorrelation function. Recalling that $\bar{g}_{d1}^I(t_r)$ and $\bar{g}_{d1}^{II}(t_r)$ each have RMS values of $1/\sqrt{2}$, their true autocorrelations at $\Delta t = 0$ are $1/2$ and $c_1^2(0) = 1/4$ for each estimate. Since $\bar{g}_{d1}^I(t_r)$ and $\bar{g}_{d1}^{II}(t_r)$ have identical power ratios and spectrums, let their common true autocorrelation function be $\bar{c}_{d1}^I(\Delta t)$, so that $c_1(\Delta t) = \bar{c}_{d1}^I(\Delta t)$ for each estimate.

Also, since $\underline{\underline{g}}_{d1}^1(t_r)$ and $\underline{\underline{g}}_{d1}^2(t_r)$ are independent, each of the two estimates in (145) will be independent and their variances can be added directly to obtain the variance of $\underline{\underline{c}}_{d1}^1(\Delta t)$:

$$\text{Var} [\underline{\underline{c}}_{d1}^1(\Delta t)] \approx \frac{1}{2\tilde{B}t_n} \left[\frac{1}{2} + 2 \underline{\underline{c}}_{d1}^{12}(\Delta t) \right] \quad (149)$$

In (149), $\underline{\underline{c}}_{d1}^1(\Delta t)$ will be one-half at $\Delta t = 0$ and approach zero as Δt becomes sufficiently large; i. e. ,

$$\text{Var} [\underline{\underline{c}}_{d1}^1(\Delta t)] \approx \begin{cases} 1/(2\tilde{B}t_n) , & \Delta t = 0 \\ 1/(4\tilde{B}t_n) , & \Delta t = \text{sufficiently large.} \end{cases} \quad (150)$$

Now apply (148) to the two estimates of the crosscorrelations in (146). Because $\underline{\underline{g}}_{d1}^1(t_r)$ and $\underline{\underline{g}}_{d1}^2(t_r)$ are independent, their true crosscorrelations are zero and $c_{12}(\Delta t)$ in (148) is zero for each estimate; $c_1(0)$ and $c_2(0)$ are each $1/2$, making their product $1/4$ for each estimate. Then the variance of each of the two estimates in (146) is $1/8\tilde{B}t_n$. In general, however, these estimates for any sample are not independent; at $\Delta t = 0$, they will be completely dependent and cancel, making the variance of $\underline{\underline{c}}_{d1}^1(0)$ equal to zero. As Δt increases, the two estimates in (146) acquire an increasing degree of independence and when Δt becomes great enough to make $\underline{\underline{c}}_{d1}^1(\Delta t)$ decrease and remain close enough to zero, the two estimates are effectively independent and their variances can be summed. Then

$$\text{Var} [\underline{\underline{c}}_{d1}^1(\Delta t)] \approx \begin{cases} 0 , & \Delta t = 0 \\ 1/(4\tilde{B}t_n) , & \Delta t \text{ sufficiently large} \end{cases} \quad (151)$$

Since the estimates of $\underline{\underline{c}}_{d1}^1(\Delta t)$ and $\underline{\underline{c}}_{d1}^2(\Delta t)$ will each have Gaussian distributions for a large number of samples, a zero crosscorrelation between the estimates will mean that the estimates are independent.

The crosscorrelation between the estimates is obtained by multiplying (145) and (146) and taking a statistical average:

$$\overline{\underline{\underline{g}}_{d1}'(\Delta t) \underline{\underline{g}}_{d1}'(\Delta t)} = \frac{1}{m_a'^2} \sum_{\ell=1}^{m_a'} \sum_{r=1}^{m_a'} \left[\begin{aligned} & \underline{\underline{g}}_{d1}'(t_r) \underline{\underline{g}}_{d1}'(t_r + \Delta t) \underline{\underline{g}}_{d1}'(t_\ell) \underline{\underline{g}}_{d1}'(t_\ell + \Delta t) \\ & + \underline{\underline{g}}_{d1}'(t_r) \underline{\underline{g}}_{d1}'(t_r + \Delta t) \underline{\underline{g}}_{d1}'(t_\ell + \Delta t) \underline{\underline{g}}_{d1}'(t_\ell) \\ & - \underline{\underline{g}}_{d1}'(t_r) \underline{\underline{g}}_{d1}'(t_r + \Delta t) \underline{\underline{g}}_{d1}'(t_\ell + \Delta t) \underline{\underline{g}}_{d1}'(t_\ell) \\ & - \underline{\underline{g}}_{d1}'(t_r) \underline{\underline{g}}_{d1}'(t_r + \Delta t) \underline{\underline{g}}_{d1}'(t_\ell) \underline{\underline{g}}_{d1}'(t_\ell + \Delta t) \end{aligned} \right] \quad (152)$$

The order of the averaging and summing can be changed so that an average bar appears over each term in each double summation. In each of these terms, there are three $\underline{\underline{g}}_{d1}'$ factors and one $\underline{\underline{g}}_{d1}'$ factor, or vice-versa. Since $\underline{\underline{g}}_{d1}'$ and $\underline{\underline{g}}_{d1}'$ are independent random variables, the average of the product in each term can be written as the product of two averages to obtain

$$\overline{\underline{\underline{g}}_{d1}'(\Delta t) \underline{\underline{g}}_{d1}'(\Delta t)} = \frac{1}{m_a'^2} \sum_{\ell=1}^{m_a'} \sum_{r=1}^{m_a'} \left[\begin{aligned} & \overline{\underline{\underline{g}}_{d1}'(t_r) \underline{\underline{g}}_{d1}'(t_r + \Delta t) \underline{\underline{g}}_{d1}'(t_\ell) \underline{\underline{g}}_{d1}'(t_\ell + \Delta t)} \\ & + \overline{\underline{\underline{g}}_{d1}'(t_r) \underline{\underline{g}}_{d1}'(t_r + \Delta t) \underline{\underline{g}}_{d1}'(t_\ell + \Delta t) \underline{\underline{g}}_{d1}'(t_\ell)} \\ & - \overline{\underline{\underline{g}}_{d1}'(t_r) \underline{\underline{g}}_{d1}'(t_r + \Delta t) \underline{\underline{g}}_{d1}'(t_\ell + \Delta t) \underline{\underline{g}}_{d1}'(t_\ell)} \\ & - \overline{\underline{\underline{g}}_{d1}'(t_r) \underline{\underline{g}}_{d1}'(t_r + \Delta t) \underline{\underline{g}}_{d1}'(t_\ell) \underline{\underline{g}}_{d1}'(t_\ell + \Delta t)} \end{aligned} \right] \quad (153)$$

But the average or mean values of $\underline{\underline{g}}_{d1}'$ and $\underline{\underline{g}}_{d1}'$ are both zero, so

$$\overline{\underline{\underline{g}}_{d1}'(\Delta t) \underline{\underline{g}}_{d1}'(\Delta t)} = 0 \quad (154)$$

and the estimates of $\bar{c}_{d1}'(\Delta t)$ and $\bar{c}_{d1}'(\Delta t)$ are independent. Since these estimates have Gaussian distributions, $\bar{C}_{d1}'(\Delta t)$ will have a bivariate Gaussian distribution with independent quadrature components about its true value for any Δt , although the variances of the real and imaginary components will, in general, be unequal. If $\bar{C}_{s1}'(\Delta t)$ is defined by (142) with "s" subscripts replacing the "d" subscripts, and $\bar{C}_{s1}'(\Delta t)$ is the true correlation function for the tap-gain function, $\bar{G}_{d1}'(t_r)$, then the same unequal bivariate Gaussian distribution with its mean value removed applies to $\bar{C}_{s1}'(\Delta t) - \bar{C}_{d1}'(\Delta t)$. Because of the exponential factor in (142), each estimate of $\bar{C}_{d1}'(\Delta t)$ must be multiplied by the exponential factor to obtain a corresponding estimate of $\bar{C}_{d1}(\Delta t)$. The bivariate Gaussian distribution with independent unequal quadrature components that applies for $\bar{C}_{s1}'(\Delta t) - \bar{C}_{d1}'(\Delta t)$ will, therefore, when multiplied by $\exp(j2\pi\nu_{s1}\Delta t)$ be suitably rotated and will specify the distribution of $\bar{C}_{s1}(\Delta t) - \bar{C}_{d1}(\Delta t)$. At $\Delta t = 0$, the distribution will be real and Gaussian with a variance and mean-square value of $1/2\tilde{B}t_m$. As Δt increases enough to make $\bar{C}_{s1}(\Delta t)$ approach and remain near zero, $|\bar{C}_{s1}(\Delta t) - \bar{C}_{d1}(\Delta t)|$ will have a Rayleigh distribution for a large number of samples (because of the equality of (150) and (151) for large Δt), with a mean-square value of $1/2\tilde{B}t_m$. While the mean-square value for intermediate values of Δt cannot be specified without knowing the dependence between the two estimates in (146), it appears likely that it cannot differ greatly from $1/2\tilde{B}t_m$. Therefore, using (125),

$$\epsilon_{ci} \approx (2B_{e1}t_m)^{-\frac{1}{2}} = 1/\sqrt{m_{e1}} \quad (155)$$

was used as the approximate RMS value of $|\bar{C}_{s1}(\Delta t) - \bar{C}_{d1}(\Delta t)|$ for a large number of samples for all values of Δt , where B_{e1} is the effective bandwidth for the tap-gain spectrum and m_{e1} is the effective number of independent values for the i -th path, as derived in appendix C.

It can be argued correctly that ϵ_{c1} is a measure of the RMS value of the magnitude of the difference between $\bar{C}_{d1}(\Delta t)$ and the true tap-gain correlation function, rather than the RMS value of $|\bar{C}_{s1}(\Delta t) - \bar{C}_{d1}(\Delta t)|$; i. e., $\bar{C}_{s1}(\Delta t)$ is not the true tap-gain correlation function, but only an estimate of it. But it is not possible to obtain the true tap-gain correlation function, so $\bar{C}_{s1}(\Delta t)$ was used in its place. While this undoubtedly degraded the reliability of the Gaussian spectrum hypothesis tests, the tests were still felt to be of value.

To derive the distribution that $|\Gamma_{i\ell}|$ in (106) would have for a large number of samples when the tap-gain functions are bivariate Gaussian and independent, substitute (143) in (140) and the result in (106) without the magnitude bars for both paths "i" and "l". Perform the multiplication to obtain

$$\Gamma_{i\ell} = \frac{1}{m_a^i} \sum_{r=1}^{m_a^i} \left\{ \begin{aligned} &[\bar{g}_{d1}^i(t_r) \bar{g}_{d\ell}^i(t_r) + \bar{g}_{s1}^i(t_r) \bar{g}_{s\ell}^i(t_r)] \\ &+ j[\bar{g}_{d1}^i(t_r) \bar{g}_{s\ell}^i(t_r) - \bar{g}_{s1}^i(t_r) \bar{g}_{d\ell}^i(t_r)] \end{aligned} \right\} \exp j2\pi(\nu_{s\ell} - \nu_{s1})t_r. \quad (156)$$

For the moment, let it be assumed that the frequency shifts on the two paths, ν_{s1} and $\nu_{s\ell}$, are equal to make the exponential factor equal to one. For a true hypothesis of independence, all four components of the tap-gain functions, $\bar{g}_{d1}^i(t_r)$, $\bar{g}_{s1}^i(t_r)$, $\bar{g}_{d\ell}^i(t_r)$, and $\bar{g}_{s\ell}^i(t_r)$, are independent and have RMS values of $1/\sqrt{2}$. Each of the four summations is an independent estimate of the indicated crosscorrelations. The bandwidths for the tap-gain spectrums for the two paths are generally different, however, so let $B_{e1\ell}$ be the larger of the effective bandwidths for the i-th and l-th paths, B_{e1} and $B_{e\ell}$, as derived in appendix C. Using $B_{e1\ell}$ for \tilde{B} in (148), the latter can be used to show that the variances of the four estimates in (156) are each $1/8B_{e1\ell}t_n$. Since all four estimates are independent, the variances of the two real estimates and the variances of the two imaginary estimates can be added to obtain $1/4B_{e1\ell}t_n$ for the variances

of the real and imaginary parts of (156). Since they are also independent and each is the variance of a Gaussian distribution, $|\Gamma_{i\ell}|$ in (106) will have a Rayleigh distribution with an RMS value of

$$\epsilon_{i\ell} \approx (2B_{e i\ell} t_m)^{-\frac{1}{2}} = 1/\sqrt{m_{e i\ell}}. \quad (157)$$

Because $B_{e i\ell}$, the larger of $B_{e i}$ and $B_{e \ell}$, was used for \tilde{B} in (148) to obtain (157), any error introduced by this approximation would tend to make $|\Gamma_{i\ell}|$ smaller than its true value and increase the probability of rejecting a correct hypothesis of independence (i. e., make the test more difficult). For this reason, (157) was felt to be a safe approximation.

In computing the estimate $\Gamma_{i\ell}$ for any pair of paths, one can view (156) as a single summation where each term is a complex number. When $\nu_{s\ell} = \nu_{s i}$, as in the derivation of (157), the amplitude and phase of successive terms in the summation differ by an amount that is dependent upon $B_{e i\ell}$; i. e., the larger $B_{e i\ell}$, the greater the magnitude of the difference between successive terms in the summation and the greater the effective number of independent values in the estimate of the crosscorrelation. For the general case, when $\nu_{s\ell} \neq \nu_{s i}$, the exponential factor in (156) causes the magnitude of the phase difference between successive terms to be greater on the average than in the special case when $\nu_{s\ell} = \nu_{s i}$. This causes the effective number of independent values to increase, thereby making the RMS value of $|\Gamma_{i\ell}|$ smaller. However, if

$$|\nu_{s\ell} - \nu_{s i}| \ll B_{e i\ell}, \quad (158)$$

the fractional increase in the average magnitude of the difference between phase values for successive terms in (156) is correspondingly small. This produces a very small increase in the effective number of independent values in the summation and a similarly small error in the RMS value of $|\Gamma_{i\ell}|$ as specified by (157). In all three samples of data

that were analyzed in the present experiment, the magnitude of the differential frequency shift, $|\nu_{s\ell} - \nu_{s1}|$, was less than half of $B_{e\ell}$ for all path combinations. Since this did not increase the effective number of independent values in (156) by any substantial amount, (157) was used as a reasonable approximation of the RMS value of $|\Gamma_{\ell}|$ in all tests of the independence of the deterministic tap-gain functions.

APPENDIX E

Recommended Simulator Specifications

Since the proposed stationary ionospheric channel model has been shown to be valid and accurate, it can be used as the basis for the design of laboratory ionospheric channel simulators. Such a simulator has been designed and built in the present program (Watterson et al., 1969). The use of a valid stationary channel simulator in laboratory experiments has several advantages (sec. 1) over similar experiments over actual propagation paths: accuracy, stationarity, repeatability, availability, range, and cost. However, for experiments to be repeatable when more than one channel simulator is used, both should not only be based on the same channel model, but both should be able to reproduce the same numerical channel parameters. Therefore, we are presenting a set of ionospheric channel simulator specifications, based on the validated model of this report, that might be considered for use by others in the design, construction, and use of ionospheric channel simulators. These specifications are not being recommended with the implication that improved ionospheric channel models are not possible or that improved models should not actively be sought, but only as a suggested guide for simulator design based on the present model.

The following recommended specifications for a stationary band-limited ionospheric channel simulator are based on the model illustrated in the block diagram in figure 1b. Let the taps be numbered 1, 2, ... i, ... n, and let τ_i be the time delay of the i-th tap. Then it can be seen that the complex time-varying frequency response of the channel model is

$$H_s(f, t) = \sum_{i=1}^n G_{s1}(t) \exp(-j2\pi\tau_i f), \quad (159)$$

where $G_{s1}(t)$ is the complex tap-gain function for the i-th path.

For each path, the tap-gain correlation function is

$$C_{si}(\Delta t) = \lim_{t_1 \rightarrow \infty} \frac{1}{t_1} \int_{-t_1/2}^{t_1/2} G_{si}^*(t) G_{si}(t + \Delta t) dt, \quad (160)$$

where the asterisk indicates the complex conjugate and $C_{si}(0)$ is the ratio of the signal power delivered over the i -th path at the model output to the signal power input to the model.

For each path, the tap-gain spectrum is the Fourier transform of the tap-gain correlation function,

$$v_{si}(\nu) = \int_{-\infty}^{\infty} C_{si}(\Delta t) \exp(-j2\pi\nu\Delta t) d\Delta t. \quad (161)$$

The function $v_i(\nu)$ has the dimension of time or inverse frequency and is the ratio of the i -th path output power per unit frequency offset, ν , to the channel input power.

The description of the channel model can be completed by specifying the characteristics of the tap-gain functions and the tap-gain spectrums. These are included in the following list of numerical specifications that are recommended for channel simulators that are based on the channel model:

- (1) Range of delay, τ_i : 10 ms minimum in 20- μ s steps. The differential delay between any pair of paths shall not differ from the nominal value by more than 1 percent.
- (2) Number of paths, n : Three minimum.
- (3) Tap-gain functions, $G_{si}(t)$: Each tap-gain function nominally shall be an independent complex bivariate Gaussian random function with a zero mean value and quadrature components with equal RMS values. Each tap-gain function is defined by

$$G_{s1}(t) = G'_{s1a}(t) \exp(j2\pi\nu_{s1a}t) + G'_{s1b}(t) \exp(j2\pi\nu_{s1b}t), \quad (162)$$

where the "a" and "b" subscripts identify the two magnetoionic components that in general are present in each mode or path. $G'_{s1a}(t)$ and $G'_{s1b}(t)$ are sample functions of two independent complex bivariate Gaussian stationary ergodic random processes, each with zero mean values and independent quadrature components with equal RMS values. Specifically, if $G'_{s1a}(t)$ is defined in terms of its real and imaginary components by

$$G'_{s1a}(t) = \underline{g}_{s1a}(t) + j \underline{\underline{g}}_{s1a}(t), \quad (163)$$

then \underline{g}_{s1a} and $\underline{\underline{g}}_{s1a}$ have a joint probability density function

$$p(\underline{g}_{s1a}, \underline{\underline{g}}_{s1a}) = \frac{1}{\pi C_{s1a}(0)} \exp \left[-\frac{\underline{g}_{s1a}^2 + \underline{\underline{g}}_{s1a}^2}{C_{s1a}(0)} \right], \quad (164)$$

where $C_{s1a}(0)$ is the autocorrelation function of $G'_{s1a}(t) \exp(j2\pi\nu_{s1a}t)$ at zero displacement ($\Delta t = 0$) and specifies the ratio of the channel output power delivered by the magnetoionic component to the channel input power. With a suitable change in the "a" subscripts, (163) and (164) also apply to $G'_{s1b}(t)$.

To explain the exponential factors in (162), consider $E[G'_{s1a}^*(t) G'_{s1a}(t + \Delta t)]$. When this autocorrelation function is computed in terms of the real and imaginary components in (163), the cross products will have zero averages because the real and imaginary components are independent. The resulting correlation function will be real and have even symmetry about $\Delta t = 0$. Its Fourier transform, the spectrum of $G'_{s1a}(t)$, must then have even symmetry about $\nu = 0$. The same is true for

$G'_{s1b}(t)$, and the primes in (162) through (164) indicate the functions have spectrums with even symmetry about $\nu = 0$. Therefore, the exponential factors in (162) were included to provide the desired frequency shifts, ν_{s1a} and ν_{s1b} , for the magnetoionic components in the tap-gain spectrum.

Each tap-gain spectrum, $v_{s1}(\nu)$, nominally shall consist in general of the sum of two Gaussian functions of frequency, one for each magnetoionic component, as specified by

$$v_{s1}(\nu) = \left[C_{s1a}(0) / (2\pi\sigma_{s1a}^2)^{\frac{1}{2}} \right] \exp\left[-(\nu - \nu_{s1a})^2 / (2\sigma_{s1a}^2) \right] + \left[C_{s1b}(0) / (2\pi\sigma_{s1b}^2)^{\frac{1}{2}} \right] \exp\left[-(\nu - \nu_{s1b})^2 / (2\sigma_{s1b}^2) \right] \quad (165)$$

where

$$C_{s1}(0) = C_{s1a}(0) + C_{s1b}(0) \quad (166)$$

and the frequency spread on each component is determined by $2\sigma_{s1a}$ and $2\sigma_{s1b}$. Equation (165) is illustrated in figure 3a.

The tap-gain functions and tap-gain spectrums shall have characteristics and independently adjustable parameters that meet the following specifications:

- (a) Power ratios, $C_{s1a}(0)$ and $C_{s1b}(0)$: 0 to - 60 dB in 1-dB steps, with errors less than ± 2 percent of the magnitude of the dB level or ± 0.25 dB, whichever is larger.
- (b) Frequency shifts, ν_{s1a} and ν_{s1b} : 0, ± 0.01 , ± 0.02 , ± 0.05 , ± 0.1 , ± 0.2 , ± 0.5 , ± 1 , ± 2 , ± 5 , ± 10 , ± 20 , ± 50 , ± 100 , ± 200 , and ± 500 Hz with errors less than ± 2 percent.
- (c) Frequency spreads, $2\sigma_{s1a}$ and $2\sigma_{s1b}$: 0.01, 0.02, 0.05, 0.1, 0.2, 0.5, 1, 2, 5, 10, 20, 50, 100, 200, and

500 Hz with errors less than ± 2 percent.

(d) Spectrum shape: For each magnetoionic component, the tap-gain spectrum shall not differ from the ideal Gaussian at any frequency by more than 1 percent of the maximum value.

(e) Distributions: The amplitude-density function for each quadrature component of $G'_{s1a}(t)$ and $G'_{s1b}(t)$ shall not differ from the ideal Gaussian distribution at any level up to three times the standard deviation by more than 1 percent of the maximum (zero-level) value or by more than the ideal density function itself at higher levels.

(f) Crosscorrelations: The four crosscorrelations between the quadrature components of $G'_{s1a}(t)$ and $G'_{s1b}(t)$ shall be less than 2 percent of $C_{s1a}(0)$ and $C_{s1b}(0)$ when the latter are equal.

(4) Frequency response: The simulator shall have a nominal bandwidth of 12 kHz. Any 3-kHz sub-band filtering incorporated to simulate transmitter and receiver RF-IF filtering shall meet DCA amplitude and time delay response specifications for HF systems (DCA, 1963).

(5) Additive noise: The average power of undesired additive noise shall be - 55 dB or lower relative to the average signal power in the same band.

(6) Nonlinear distortion: The average power of undesired nonlinear distortion components shall be - 40 dB or lower relative to the average signal power.

In selecting the specific numerical values of delay, frequency shift, and frequency spread for the specifications above, the ranges of values

were made large enough to cover those typically encountered in the ionospheric medium. For the frequency shifts and frequency spreads, the upper ends of the ranges were extended somewhat beyond the values typically found in the ionosphere because the added simulator cost is negligible and the extreme values might be useful in some simulator experiments. A range of time delays greater than 10 ms was not chosen because it was felt that the possible advantages would not be worth the added simulator cost for most applications. While the 20- μ s adjacent delay spacing is smaller than would usually be required, it is easy to achieve and could be of value in simulating paths with significant time spread. The 1, 2, 5 pattern in the frequency shifts and frequency spreads was chosen because adjacent values have approximately the same separation on a logarithmic scale and their ratios are conveniently obtained in digital dividers. The tolerances on the various specifications were made as large as possible without incurring significant degradation in simulator performance.

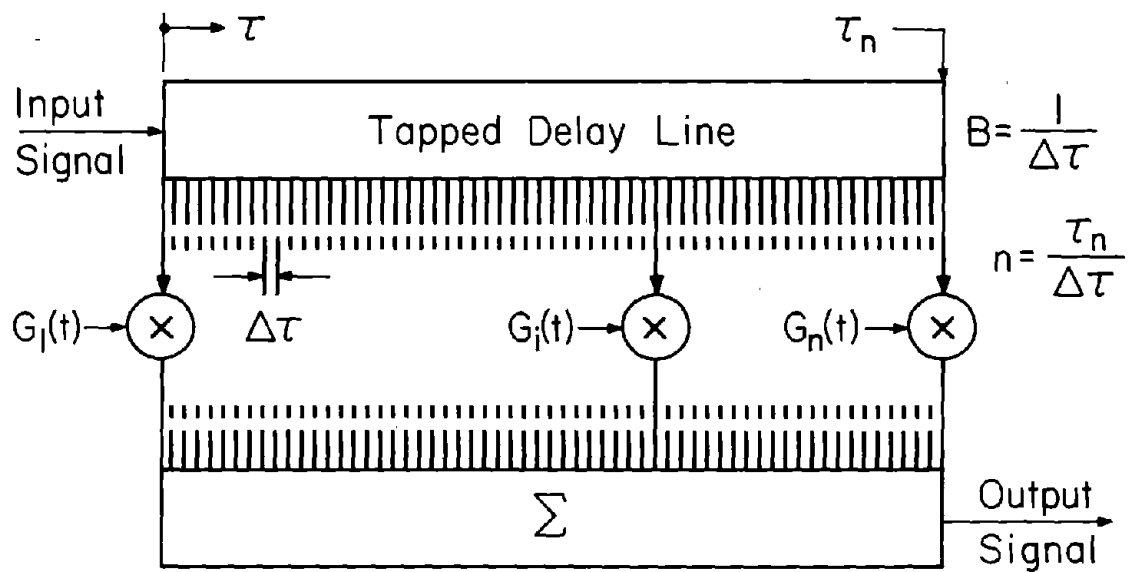
In general, the frequency shifts and frequency spreads of the two magnetoionic components are unequal. However, for some ionospheric modes, the shifts and spreads are sufficiently close to being equal that the tap-gain spectrum can be represented by a single Gaussian function. In this case, $C_{s1b}(0)$ becomes zero (i. e., ≤ -60 dB) in (162), (165), and (166), causing the tap-gain spectrum to appear as in figure 3b.

In the ionospheric channel model of this report, and in the above specifications based on it, the specification that the tap-gain functions are bivariate Gaussian with zero mean values implies that no constant-amplitude component is present. However, specular components with or without frequency shifts might reasonably be incorporated in a channel simulator based on the validated model for two reasons:

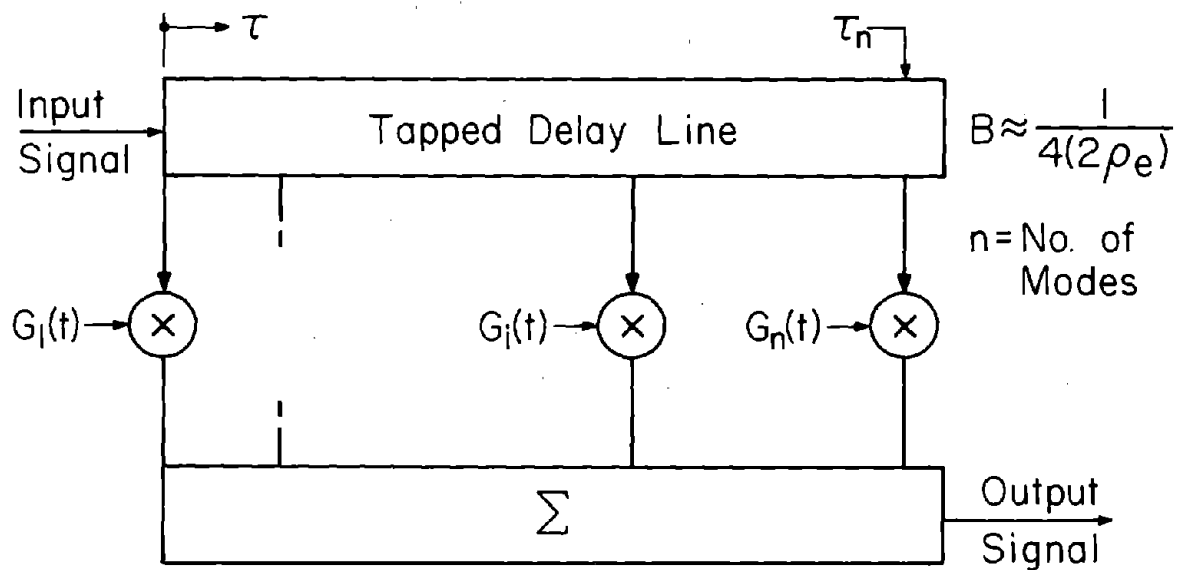
(a) While the measured ionospheric channels that were used to validate the channel model had no detectable specular components and very possibly no skywave ionospheric channels have specular components (Boys, 1968), short ionospheric links undoubtedly have a specular component in the ground-wave.

(b) Specular components that appear in tap-gain spectrums as Dirac delta functions with selectable frequency shift can be incorporated with negligible additional cost in simulators that are based on the validated model.

For these reasons, it is suggested that specular components might be included in any channel simulator based on the validated model, but it is recommended that they be excluded in any simulation of HF ionospheric skywave paths.



(a) Equally Spaced Taps



(b) Unequally Spaced Taps

Figure 1. Block diagrams of channel models.

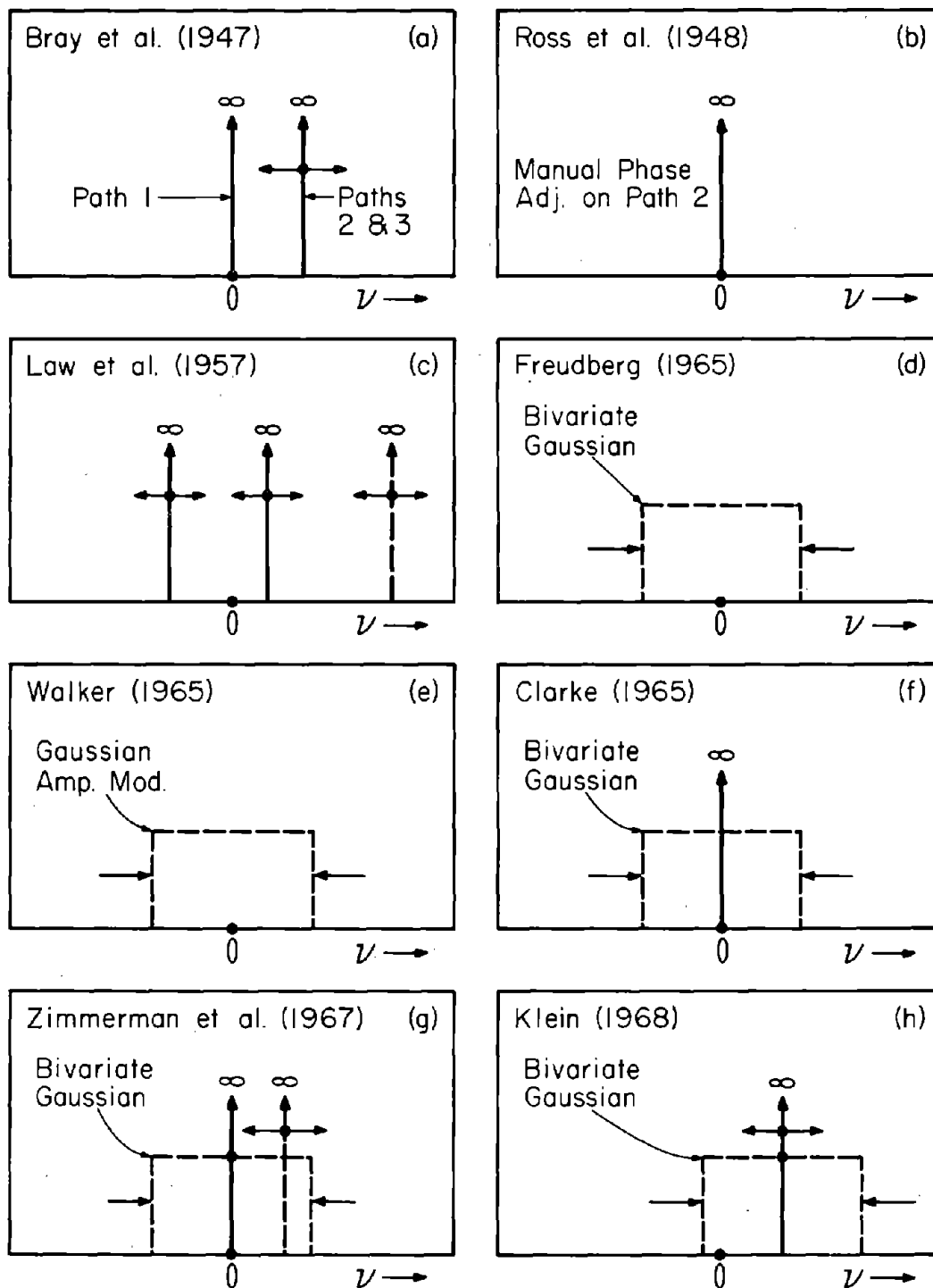


Figure 2. Tap-gain spectrums used by others.

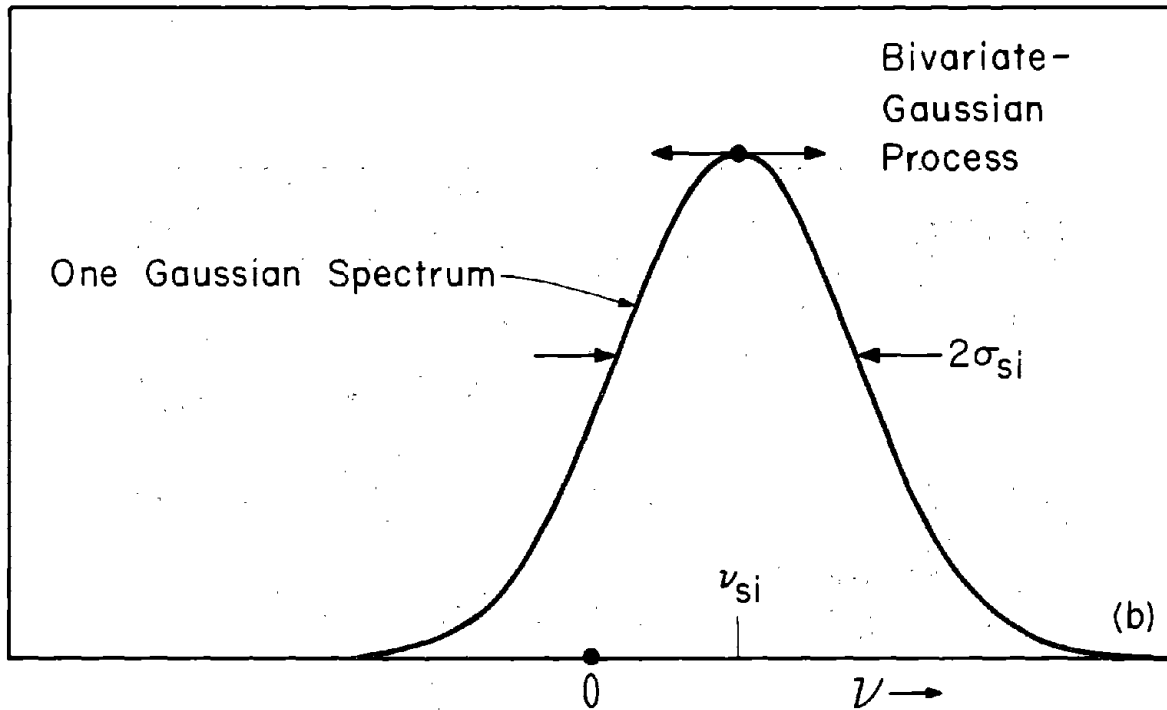
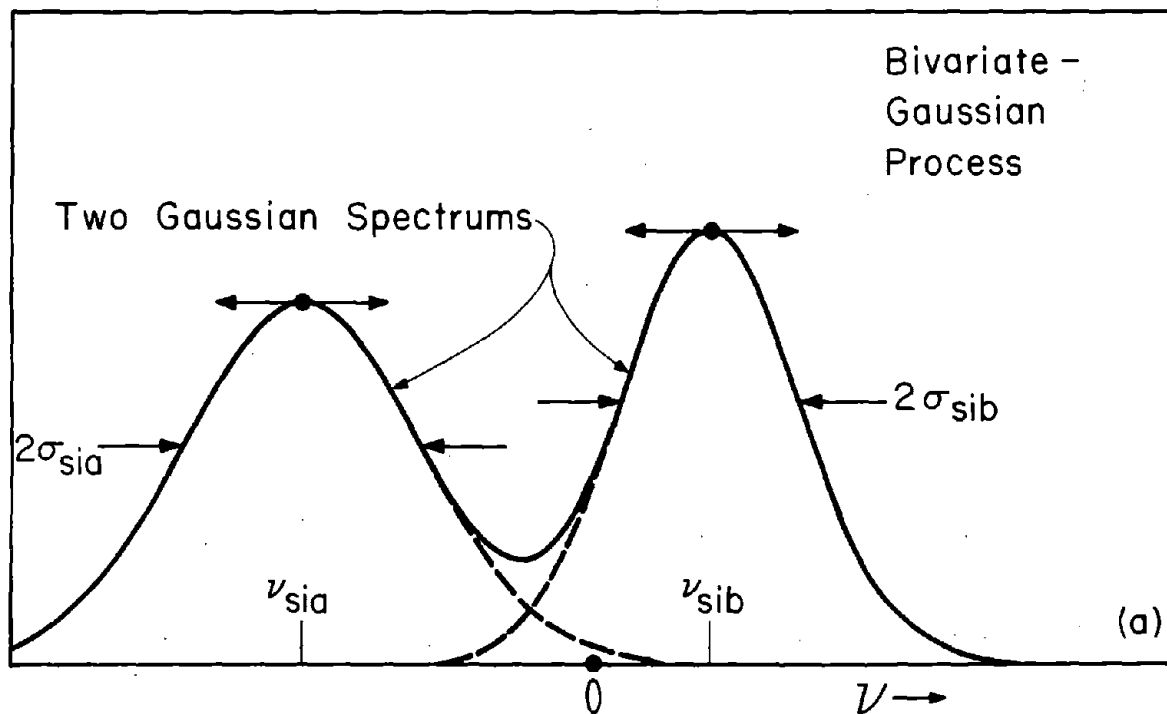


Figure 3. Tap-gain spectrums in chosen model.

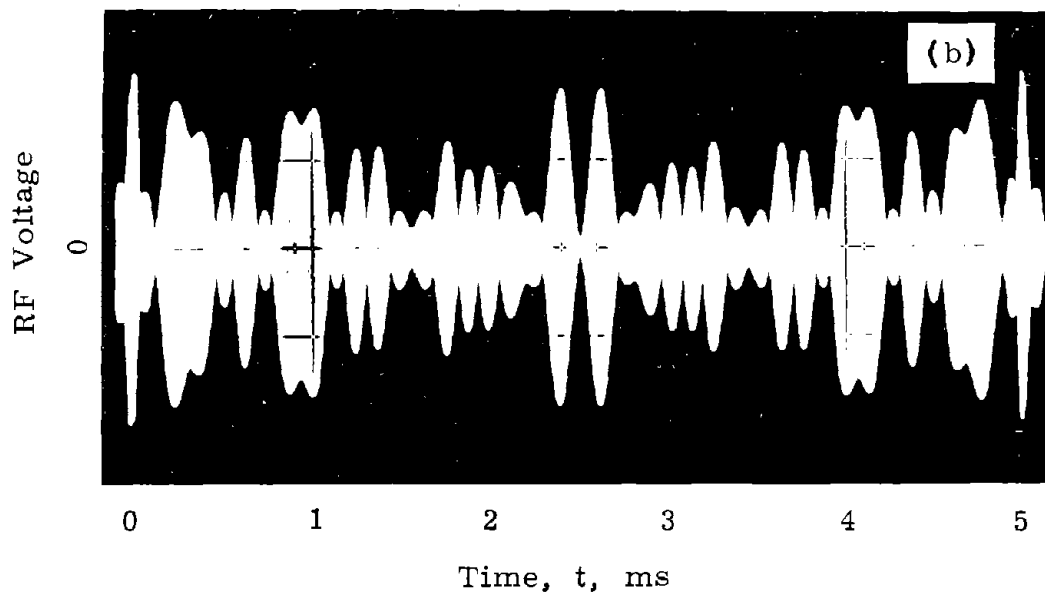
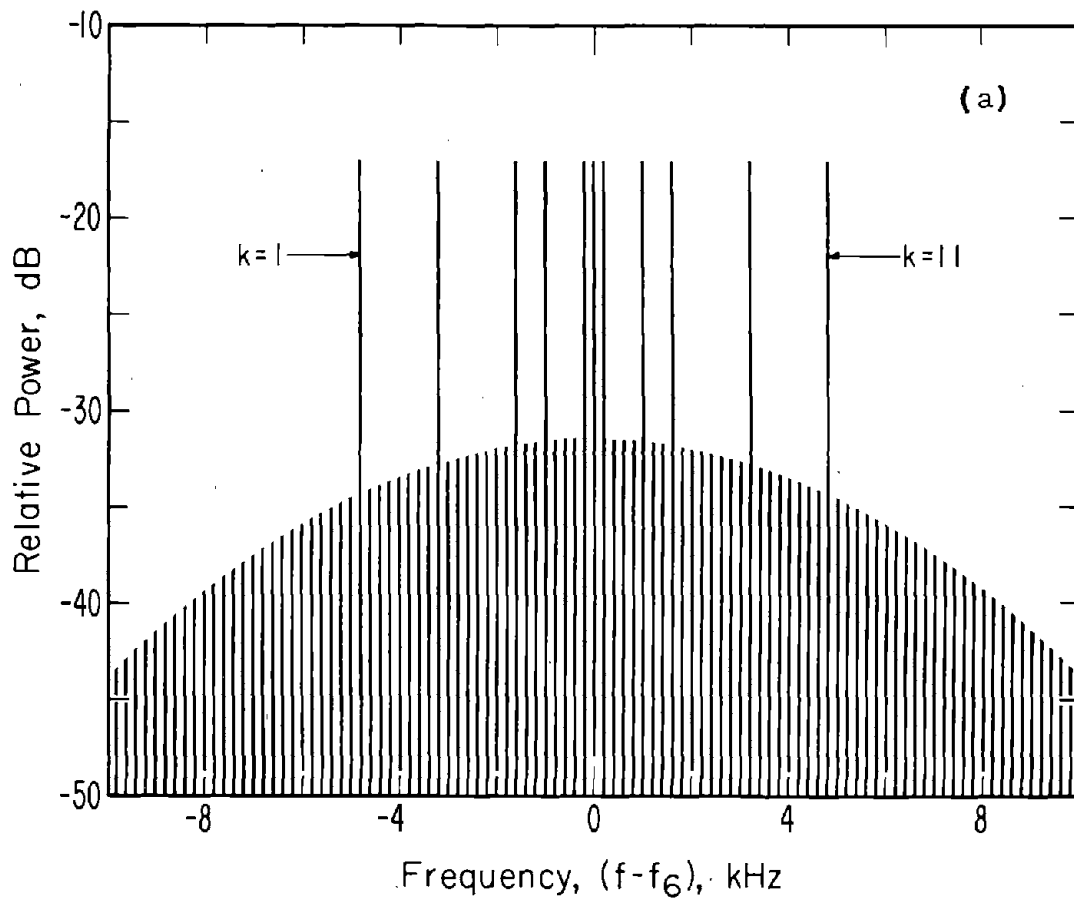


Figure 4. Transmitter output; (a) power spectrum and (b) time function.

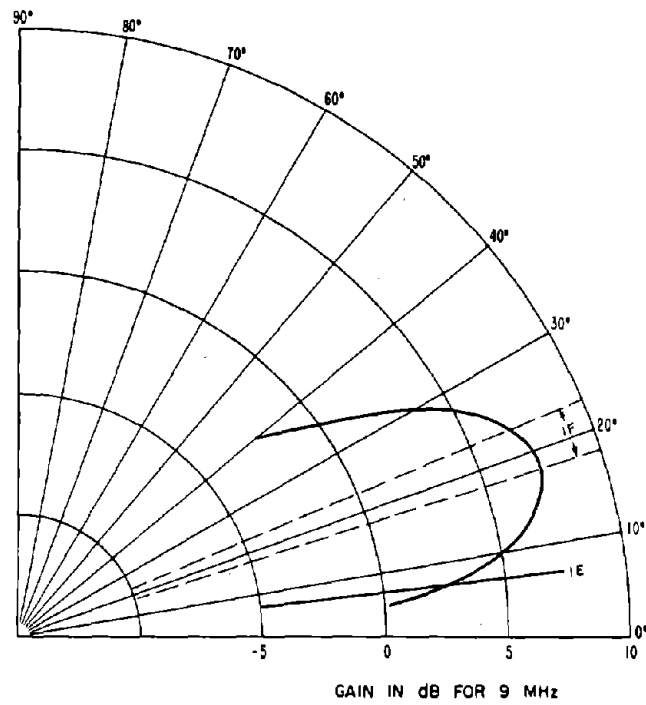
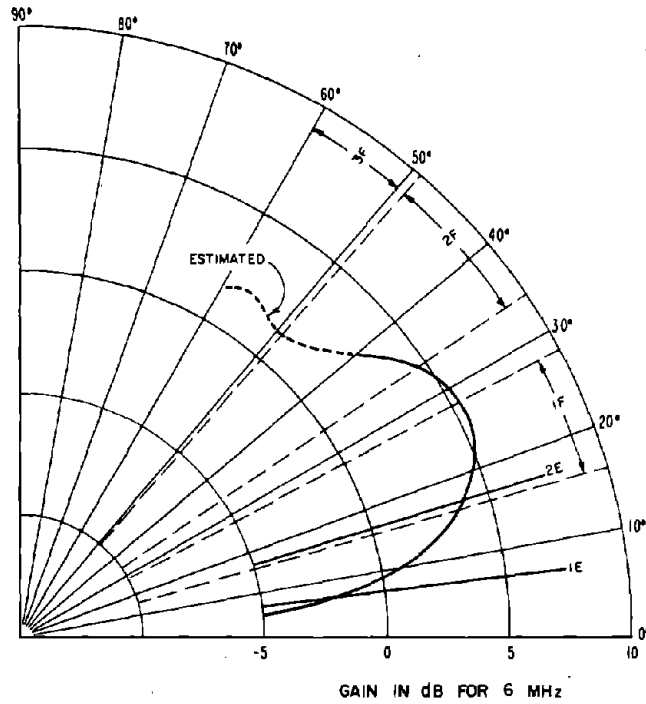


Figure 6. Transmitting and receiving theoretical antenna patterns.

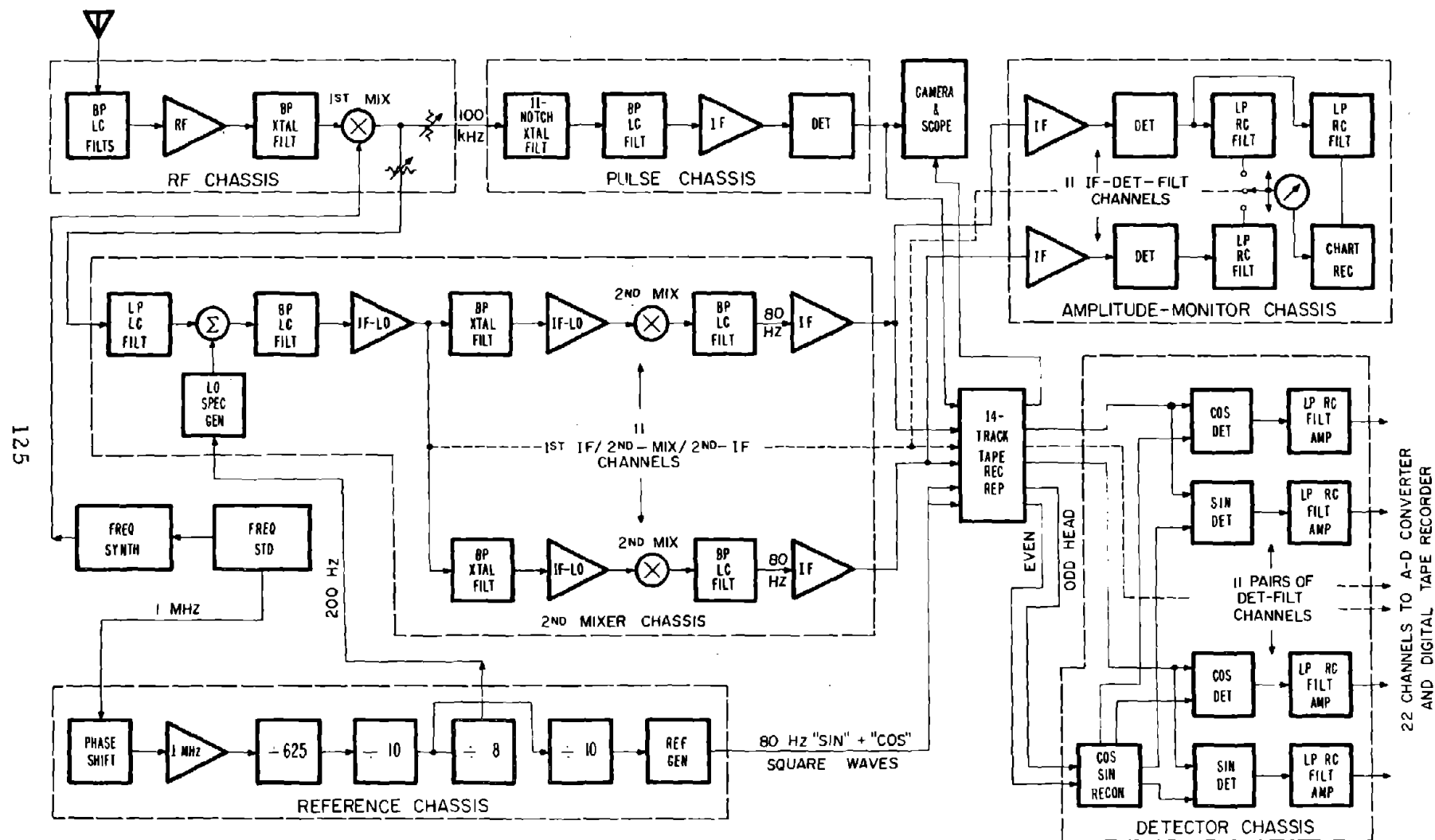


Figure 7. Receiver block diagram.

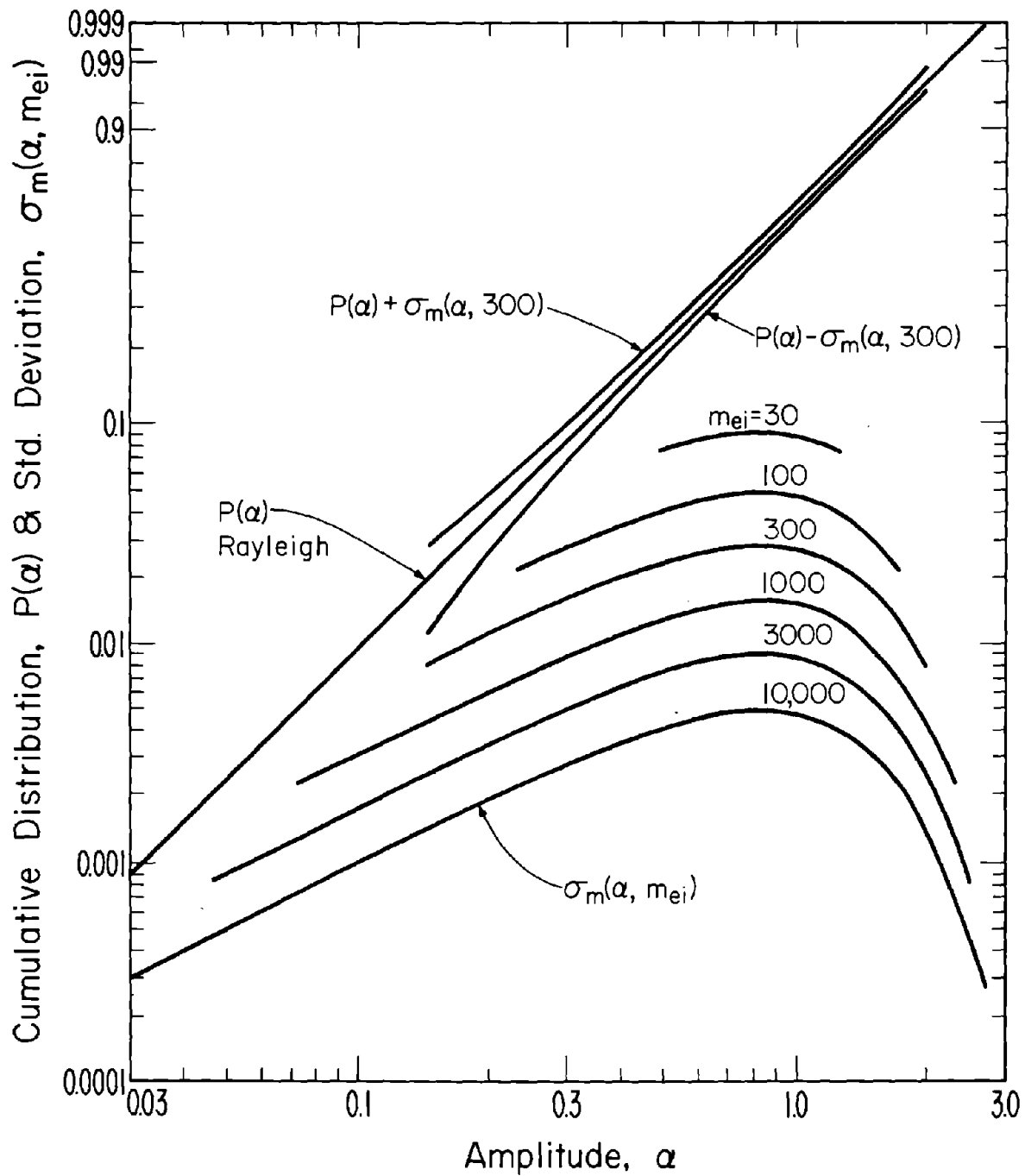


Figure 8. Standard deviation of the cumulative distribution of a Rayleigh-distributed variable.

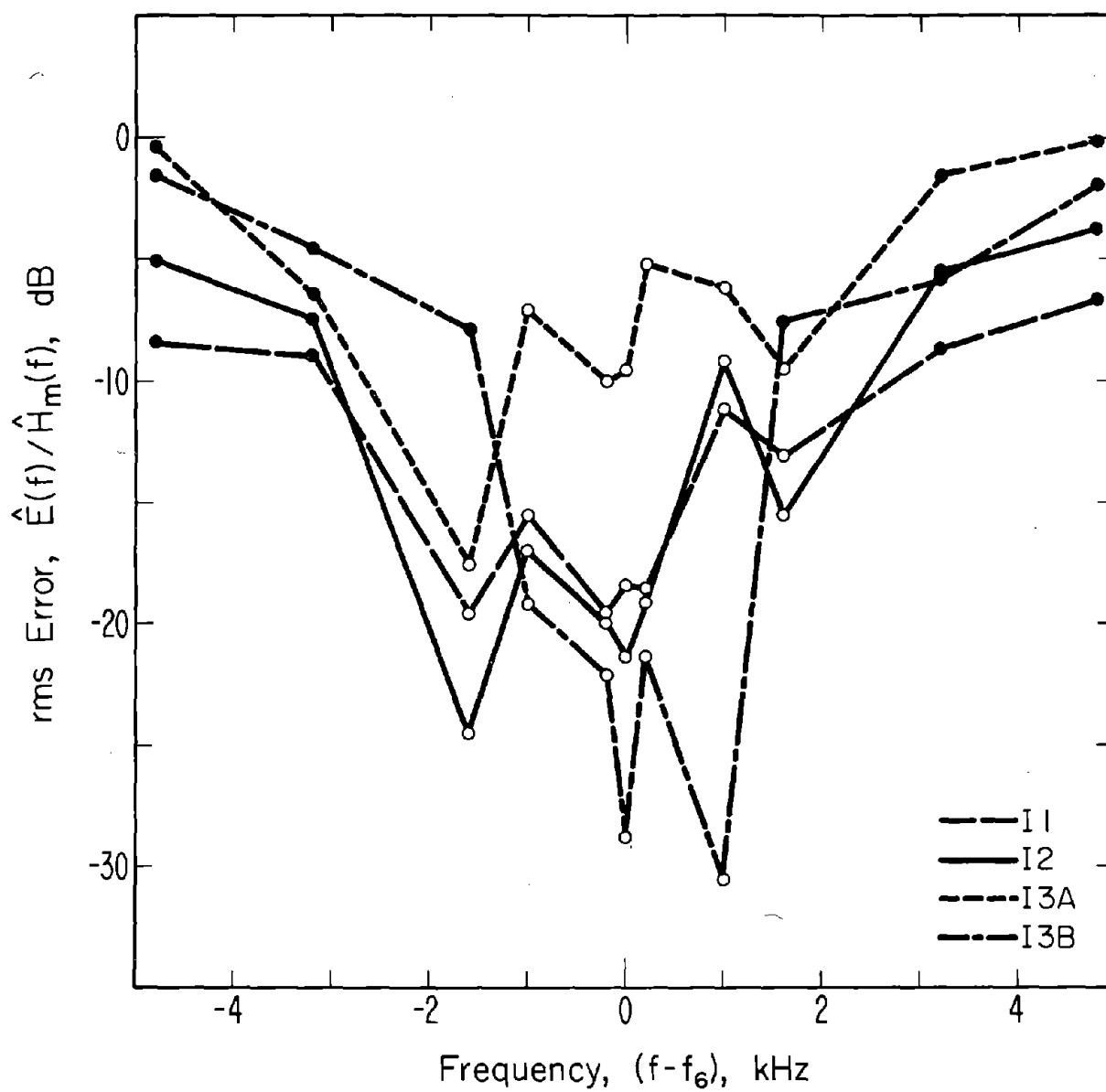


Figure 9. RMS errors in time of the deterministic fits.

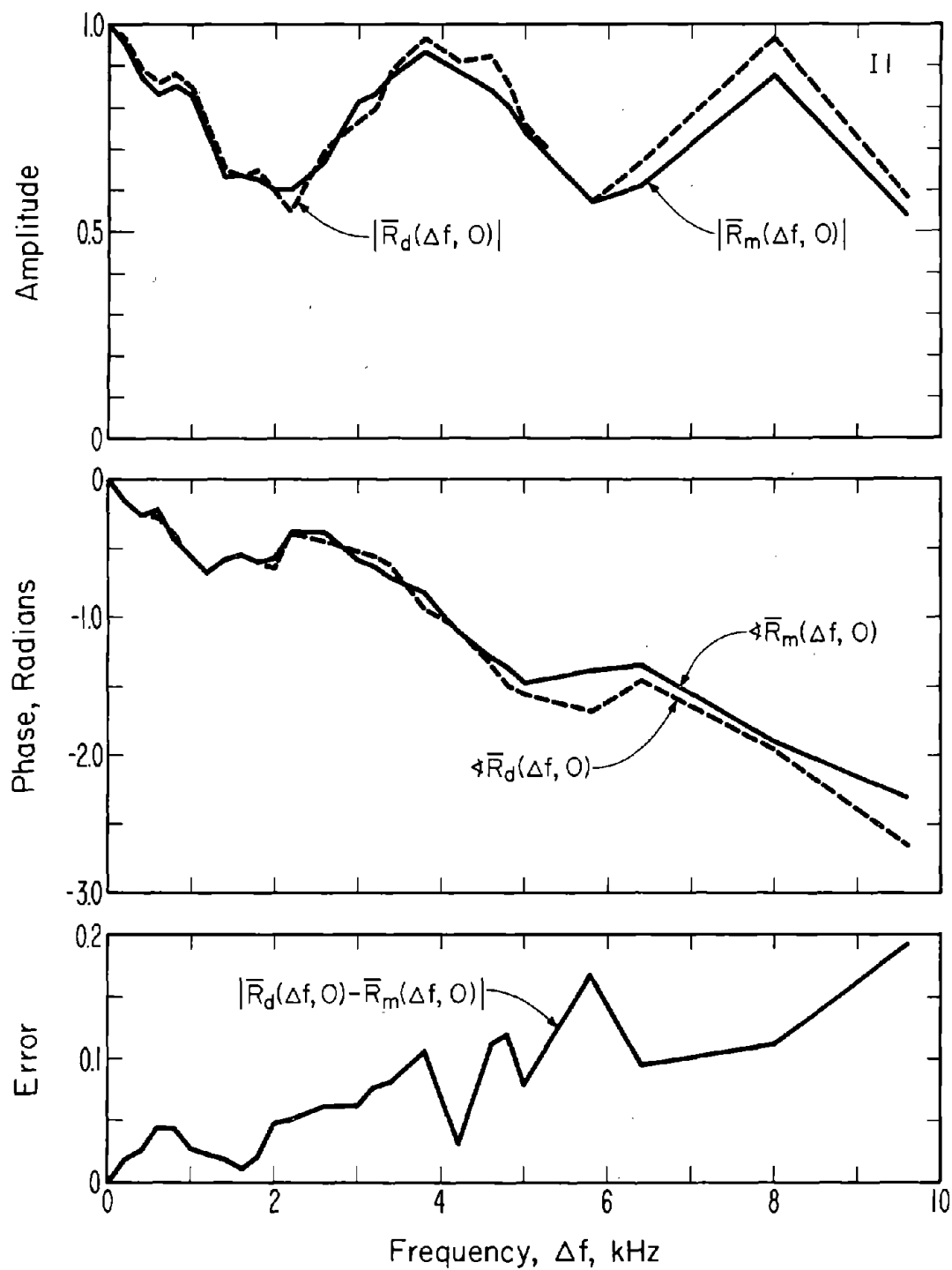


Figure 10. Channel correlation functions on the frequency axis for measured and deterministic channels in sample 11.

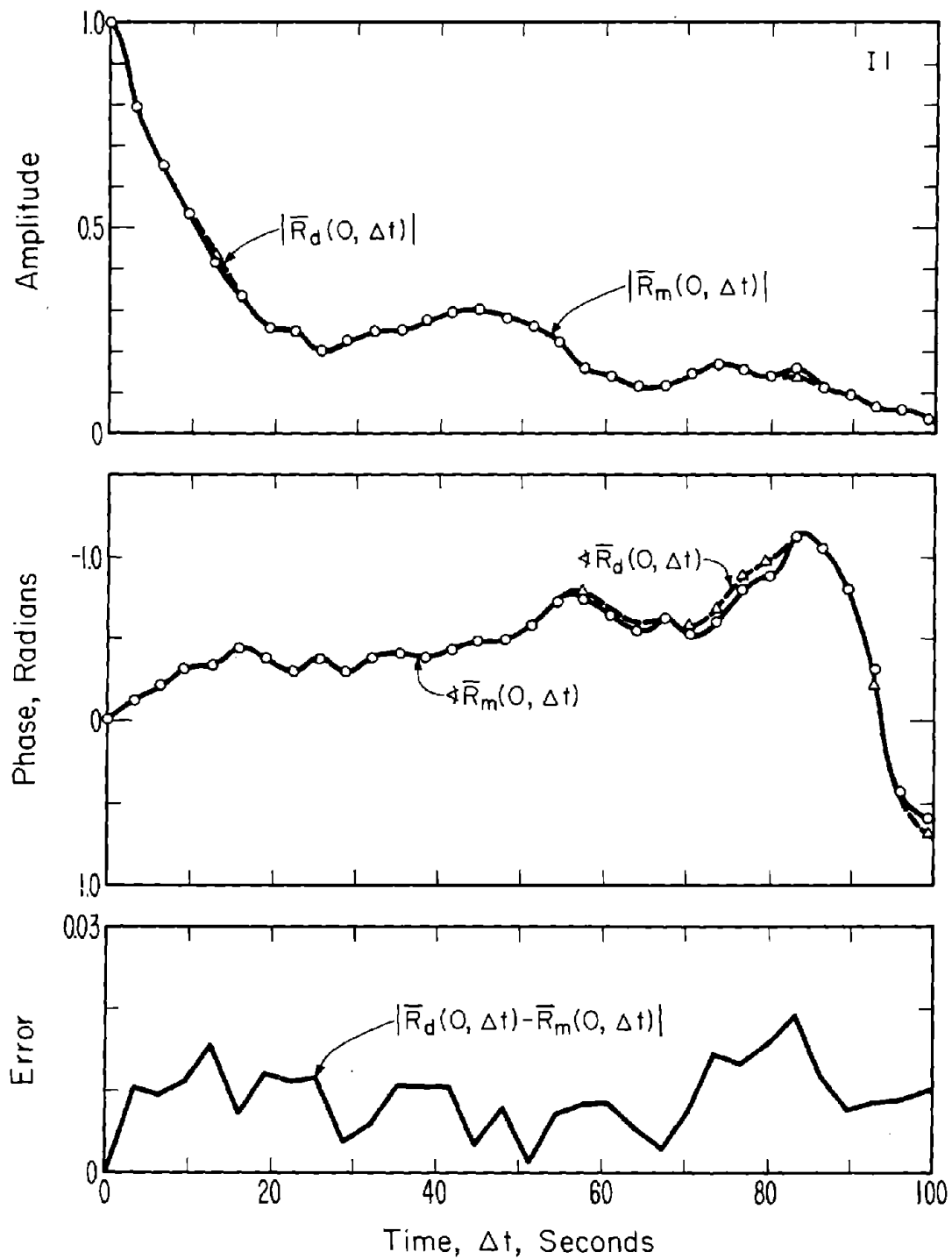


Figure 11. Channel correlation functions on the time axis for measured and deterministic channels in sample 11.

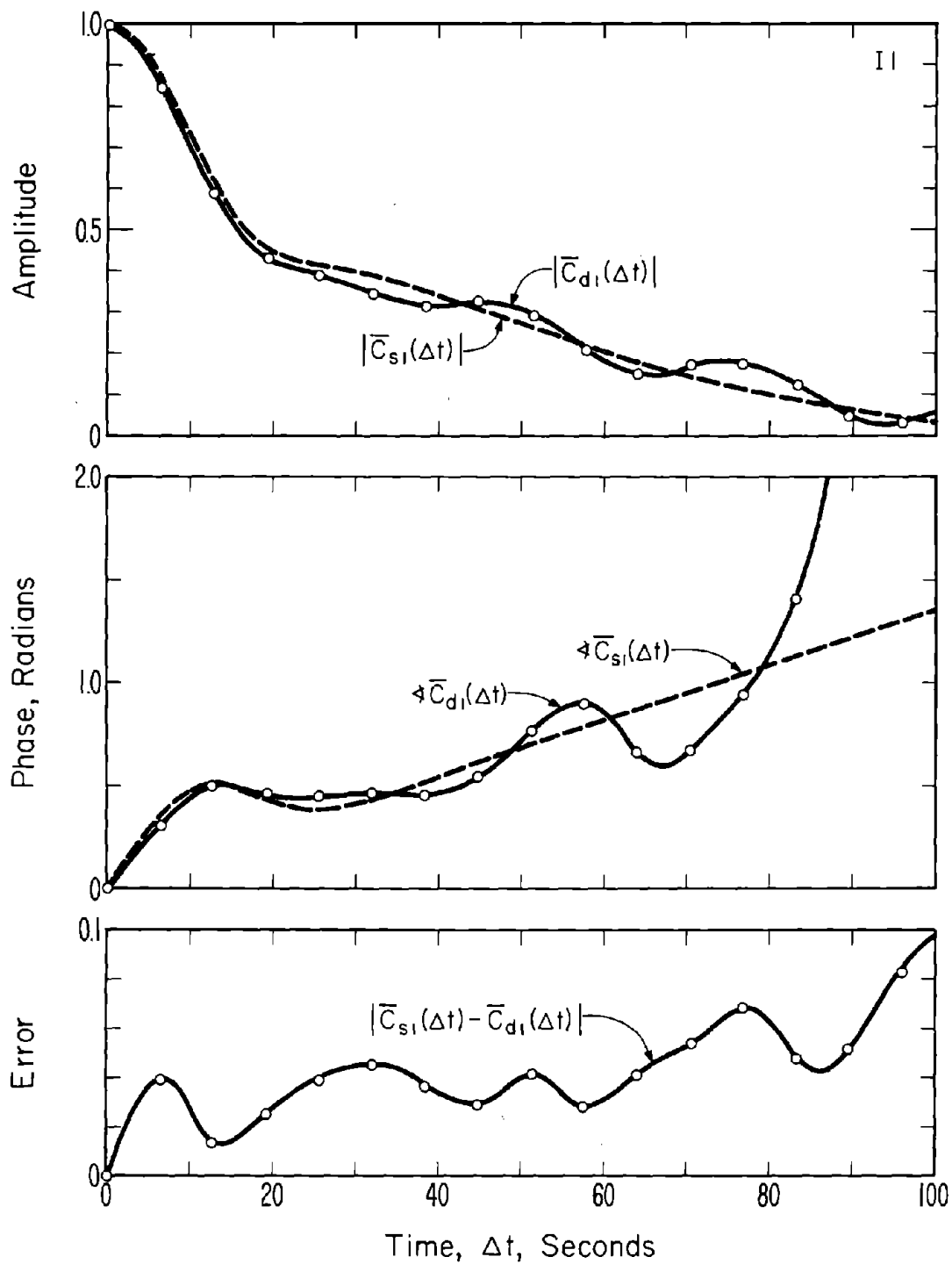


Figure 12. Tap-gain correlation functions for deterministic and statistical channels on path $i=1$ in sample 11.

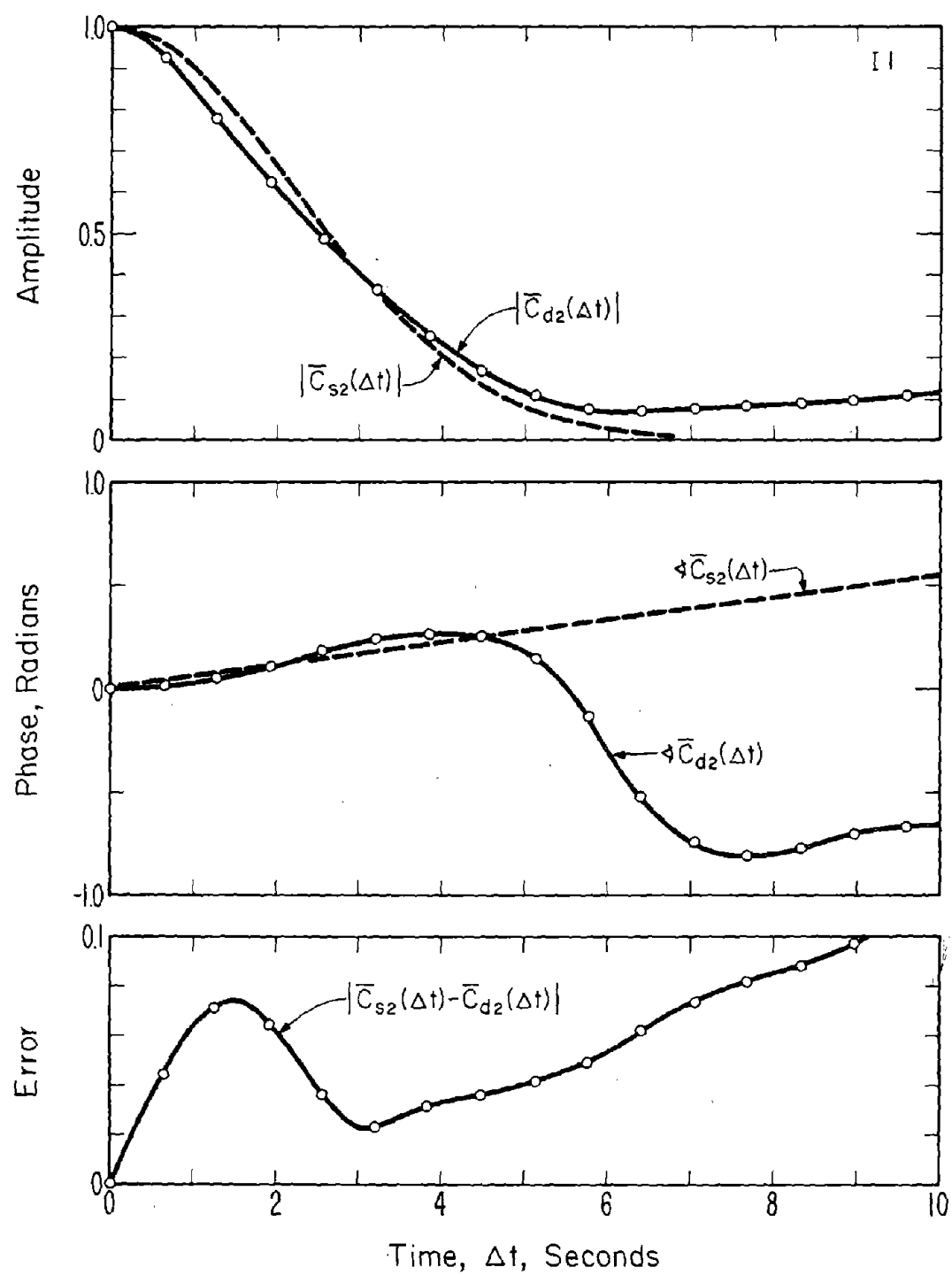


Figure 13. Tap-gain correlation functions for deterministic and statistical channels on path $i=2$ in sample I1.

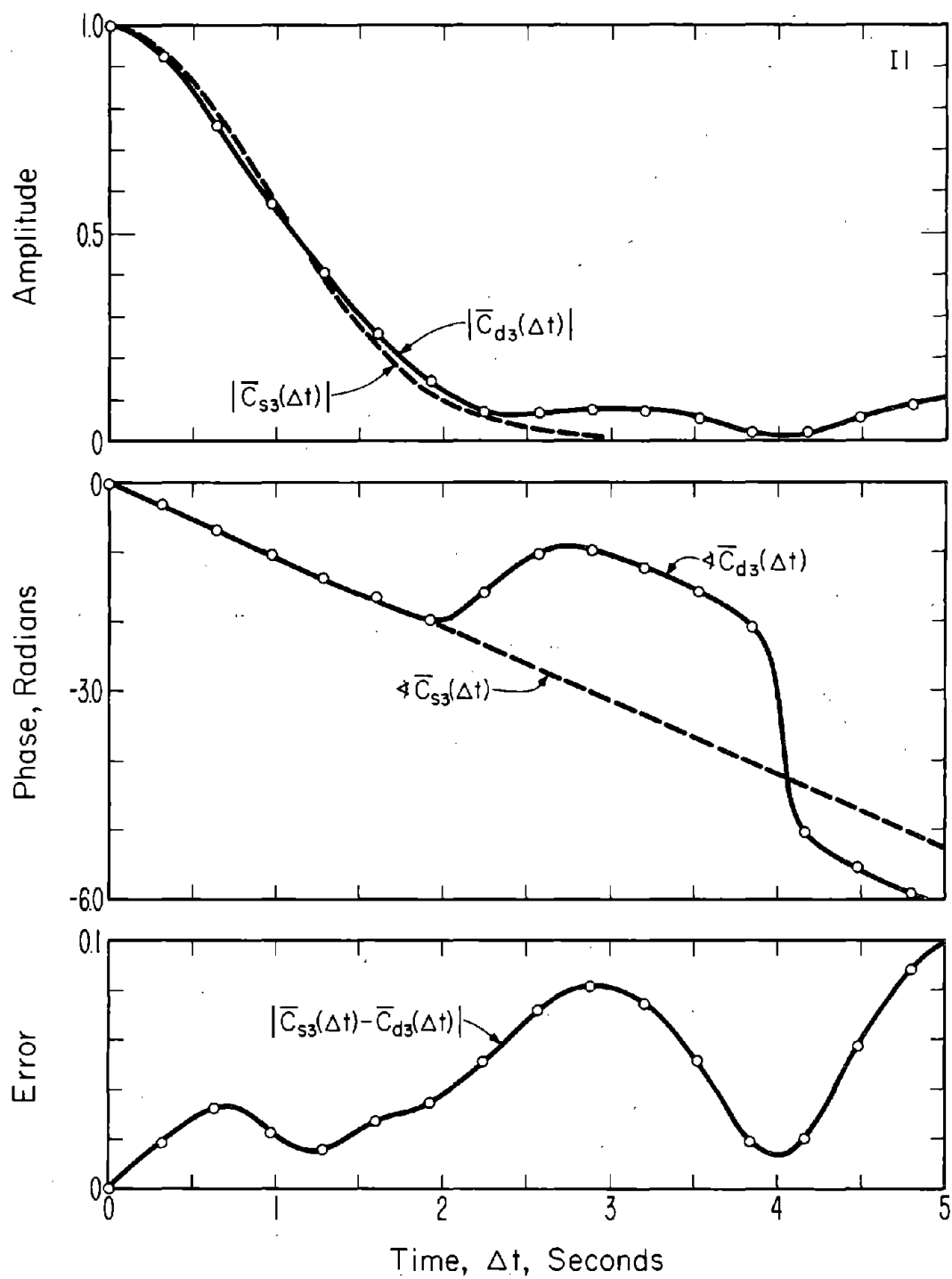


Figure 14. Tap-gain correlation functions for deterministic and statistical channels on path $i=3$ in sample II.

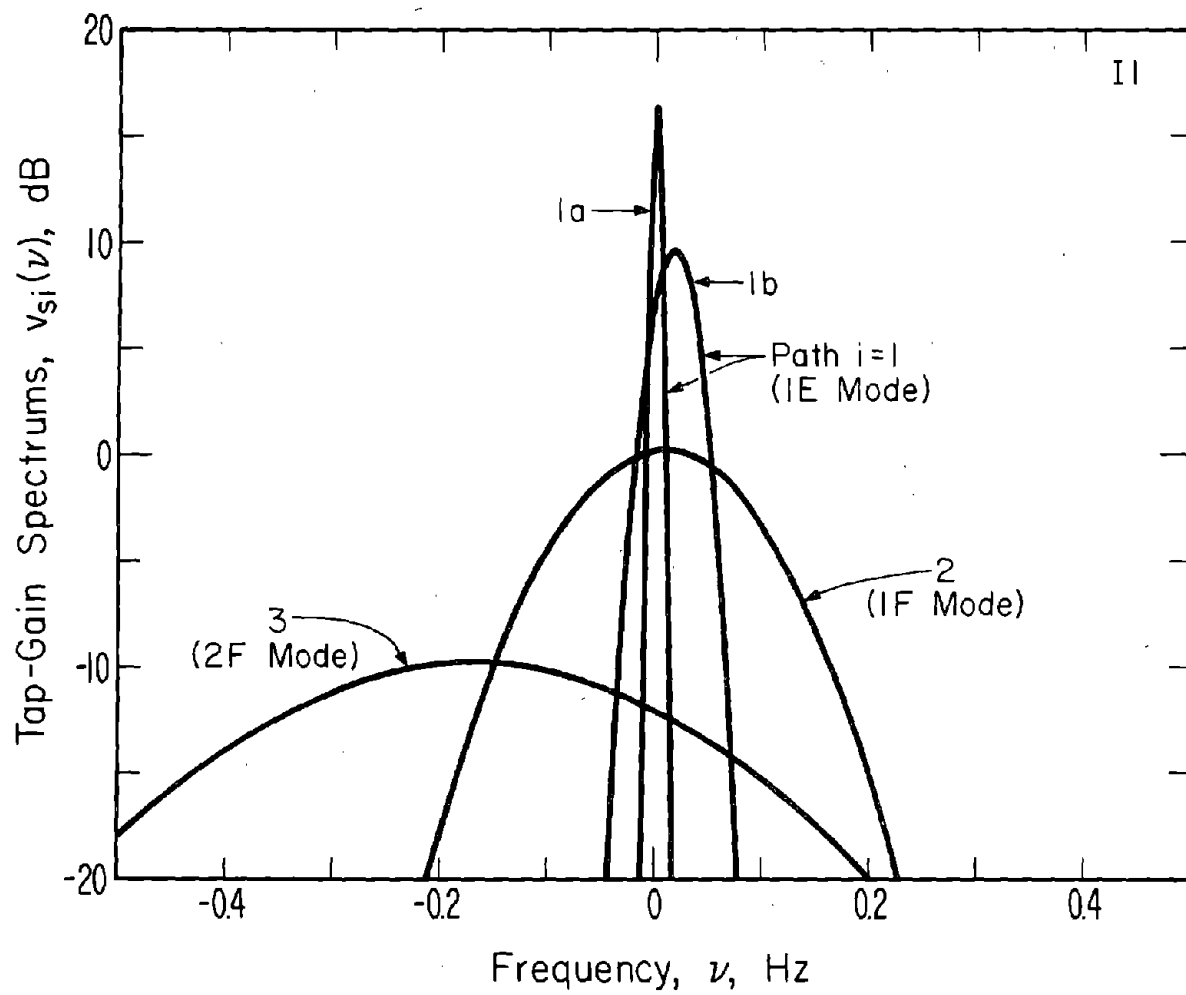


Figure 15. Tap-gain spectrums for the statistical channel in sample 11.

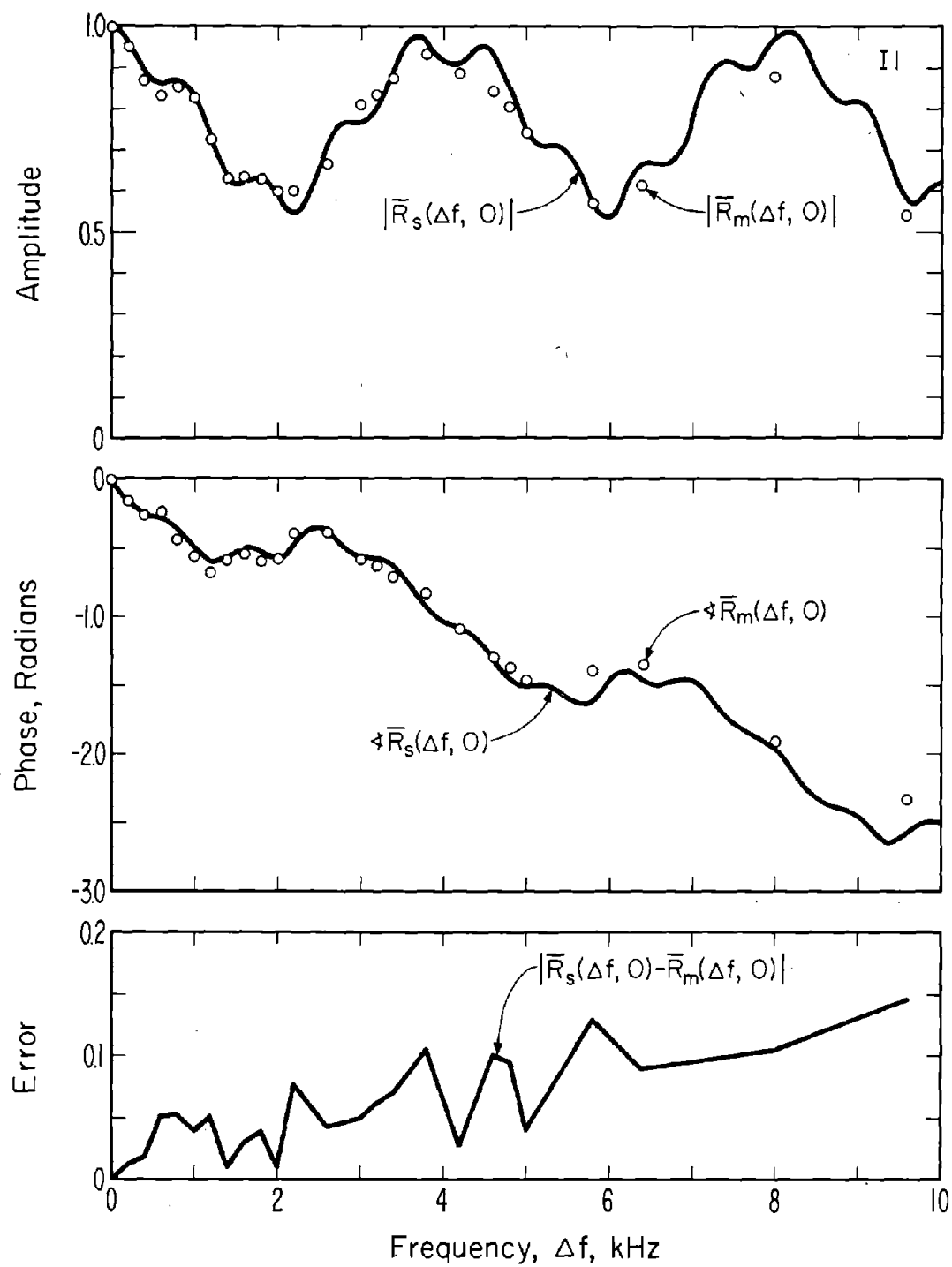


Figure 16. Channel correlation functions on the frequency axis for measured and statistical channels in sample II.

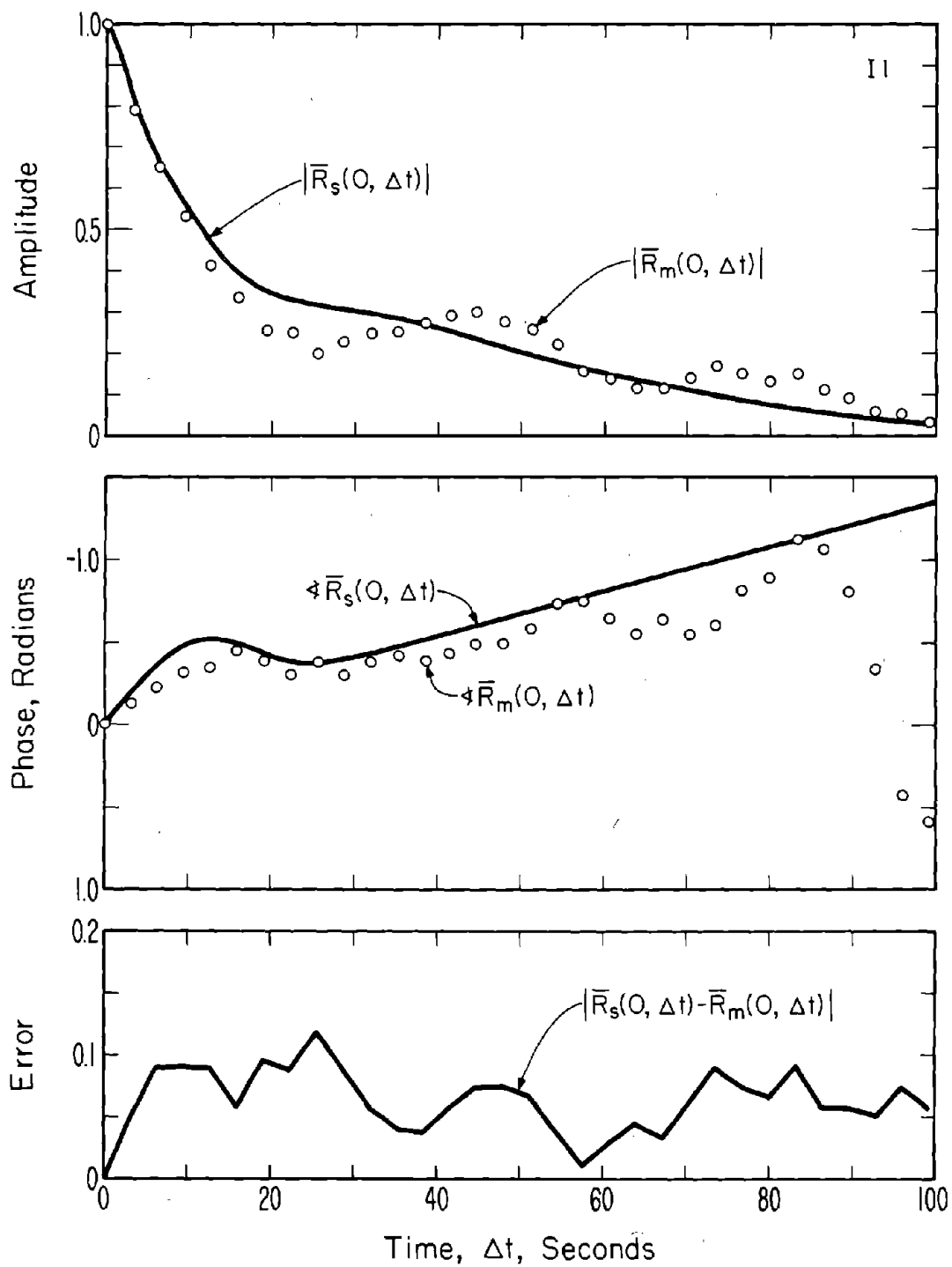


Figure 17. Channel correlation functions on the time axis for measured and statistical channel in sample II.

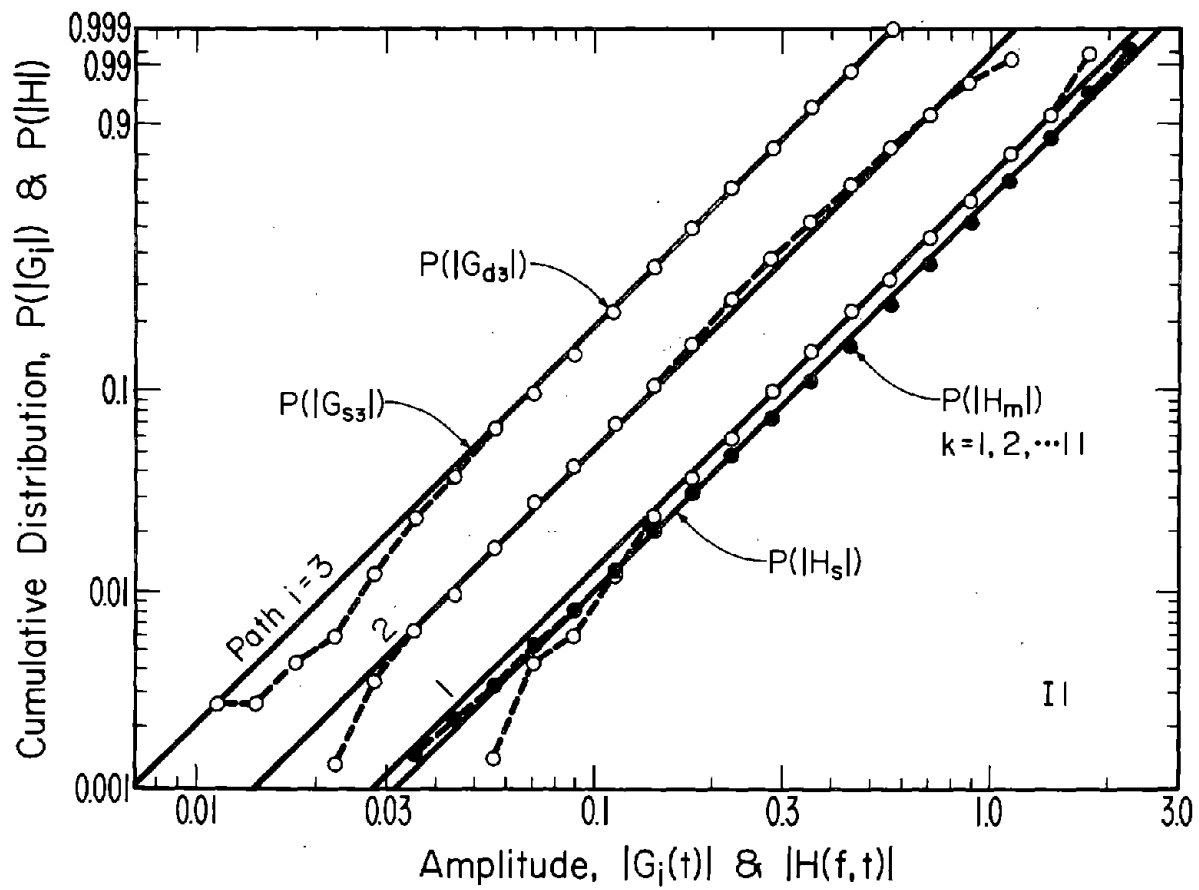


Figure 18. Cumulative distributions of the magnitudes of the tap-gain functions in the deterministic and statistical channels in sample I1.

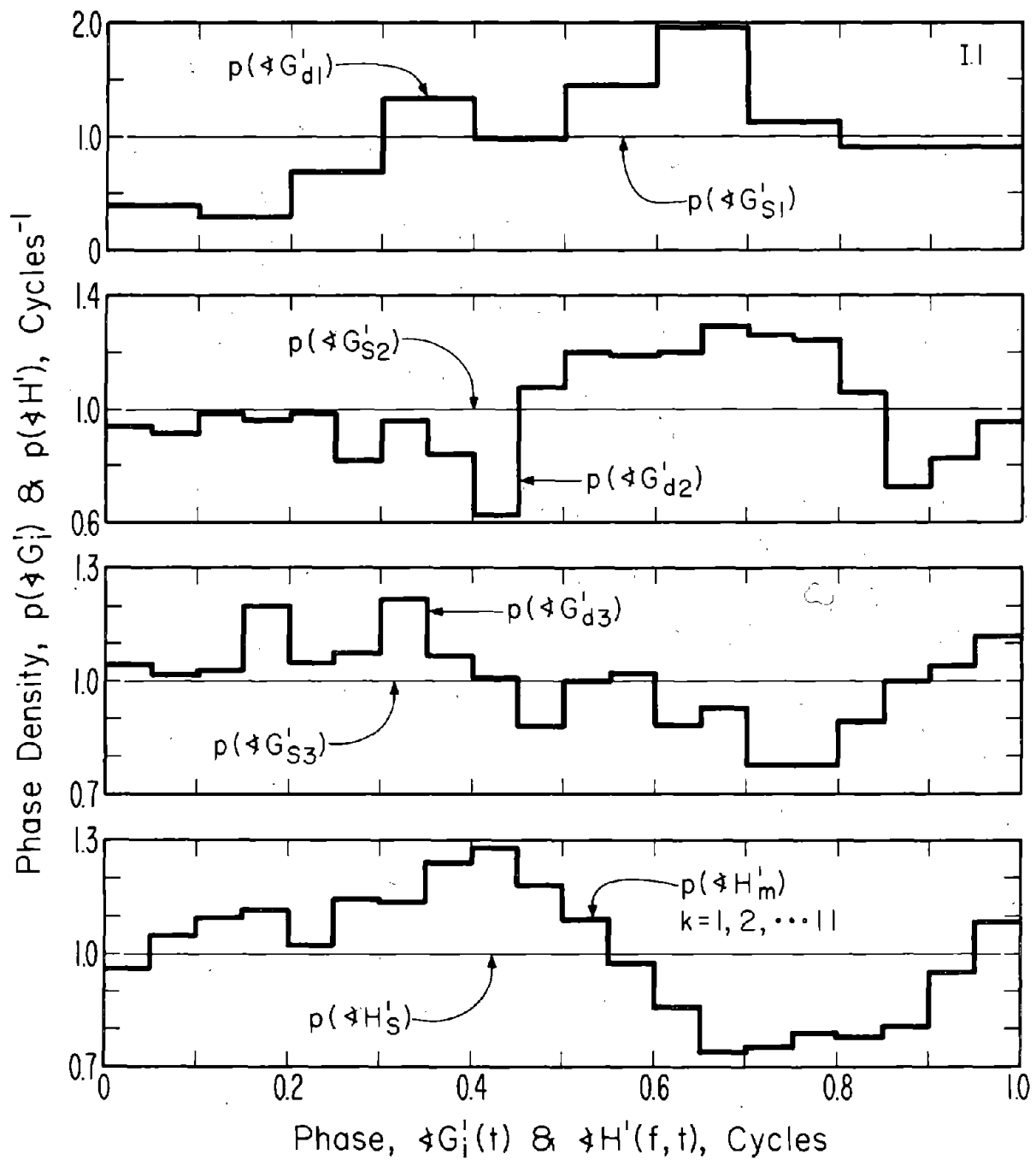


Figure 19. Histograms of the phases of the tap-gain functions in the deterministic and statistical channels in sample 11.

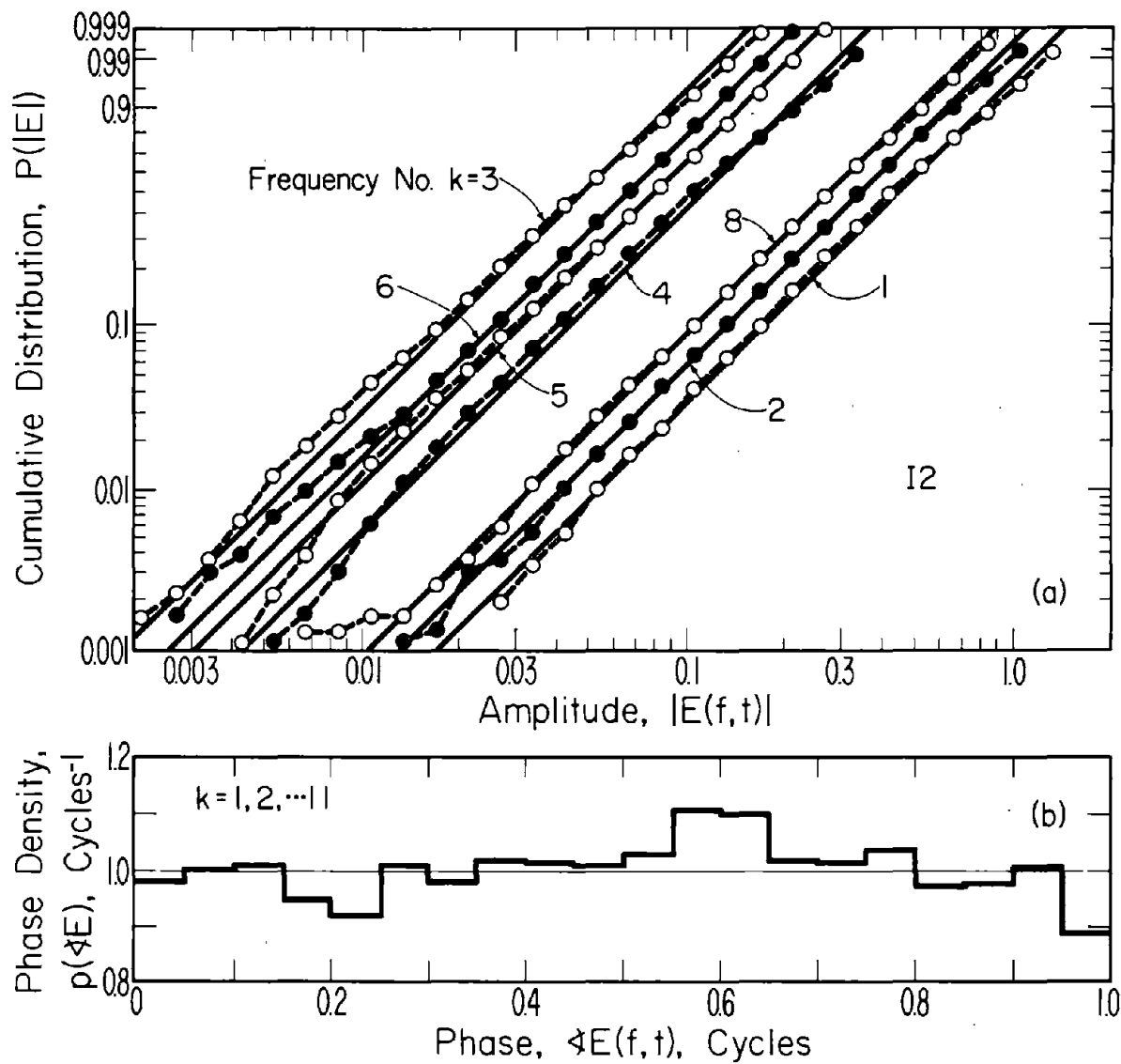


Figure 20. Distributions of the magnitudes and phases of the errors in the deterministic fit in sample I2.

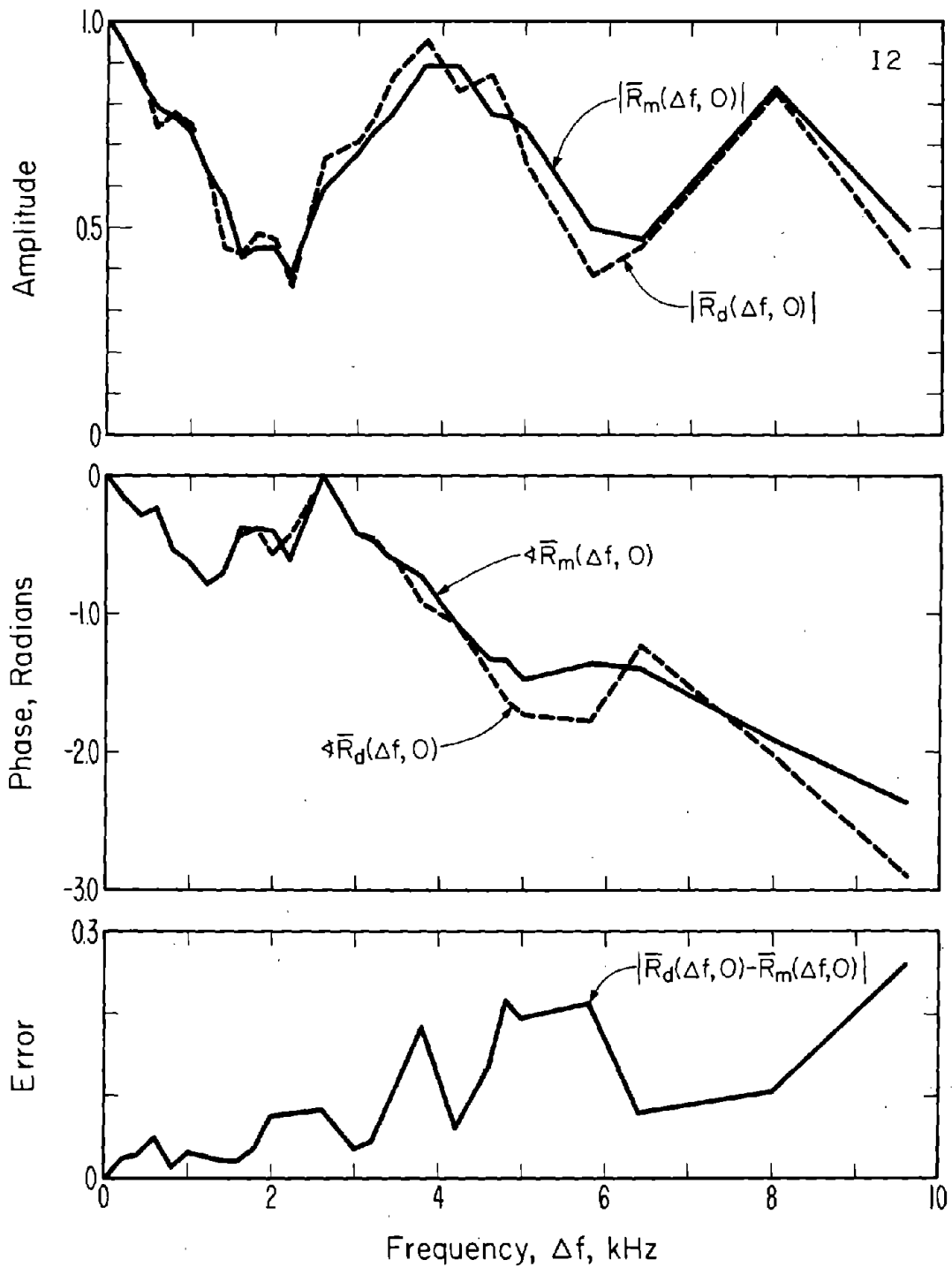


Figure 21. Channel correlation functions on the frequency axis for measured and deterministic channels in sample 12.

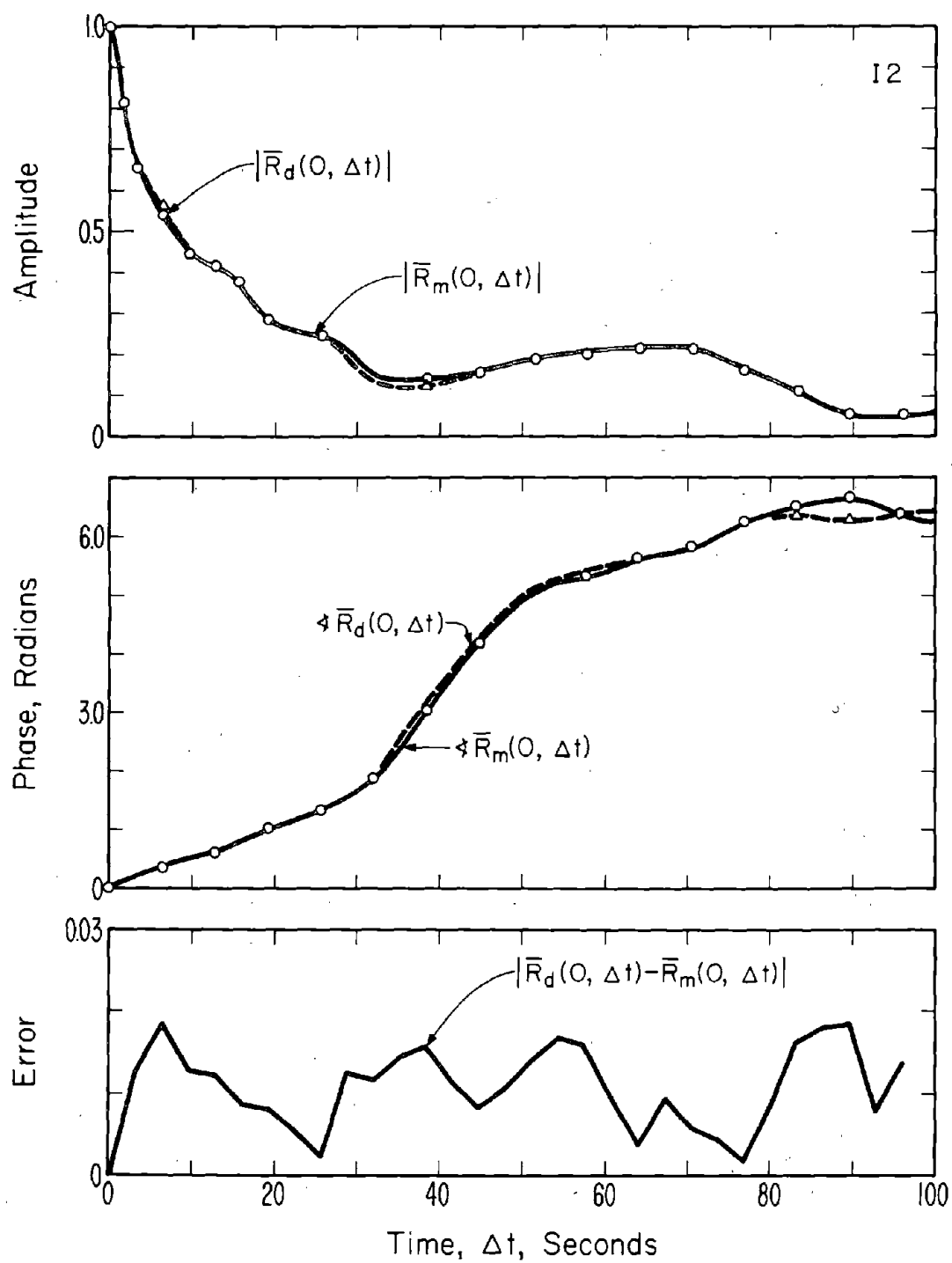


Figure 22. Channel correlation functions on the time axis for measured and deterministic channels in sample 12.

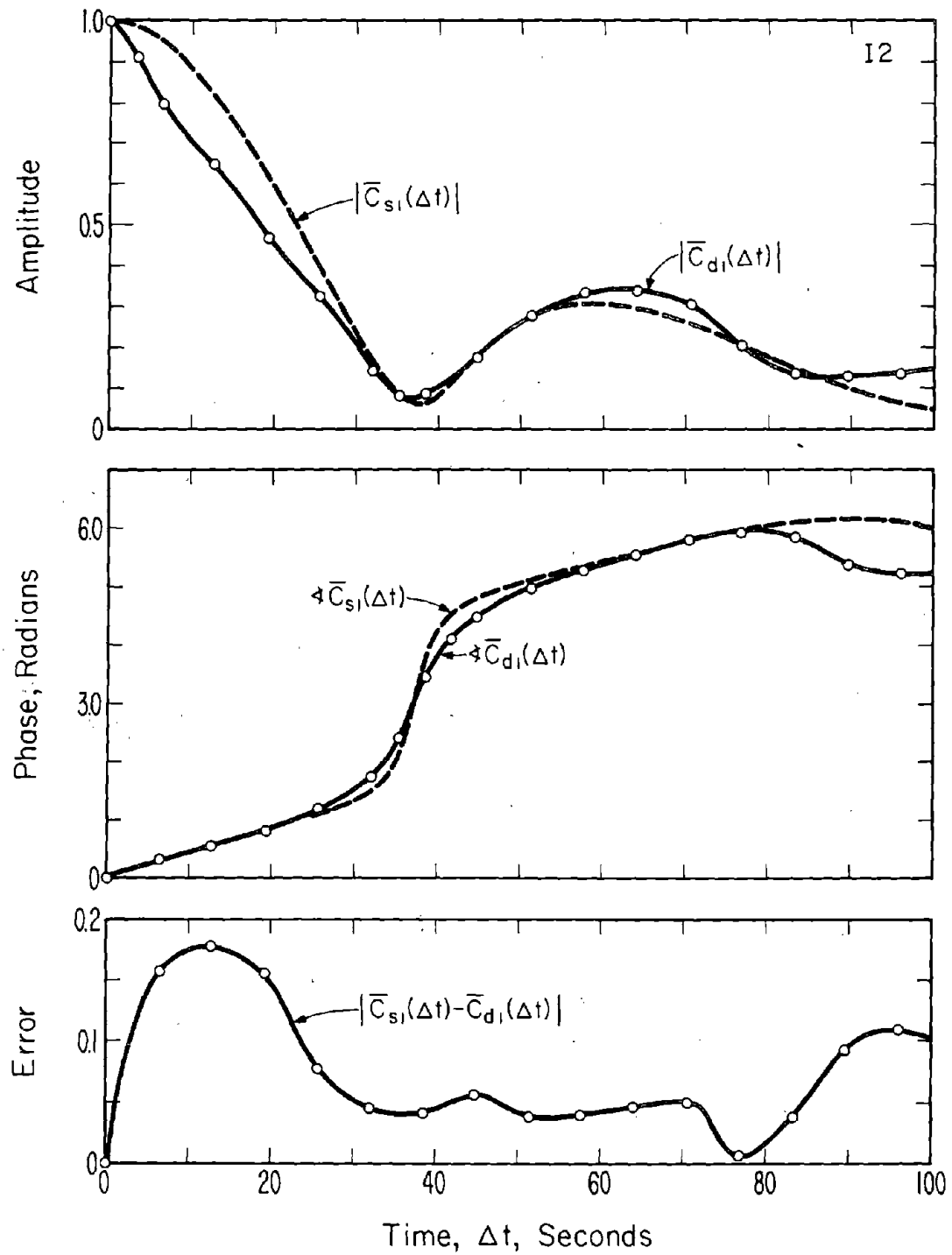


Figure 23. Tap-gain correlation functions for deterministic and statistical channels on path $i=1$ in sample I2.

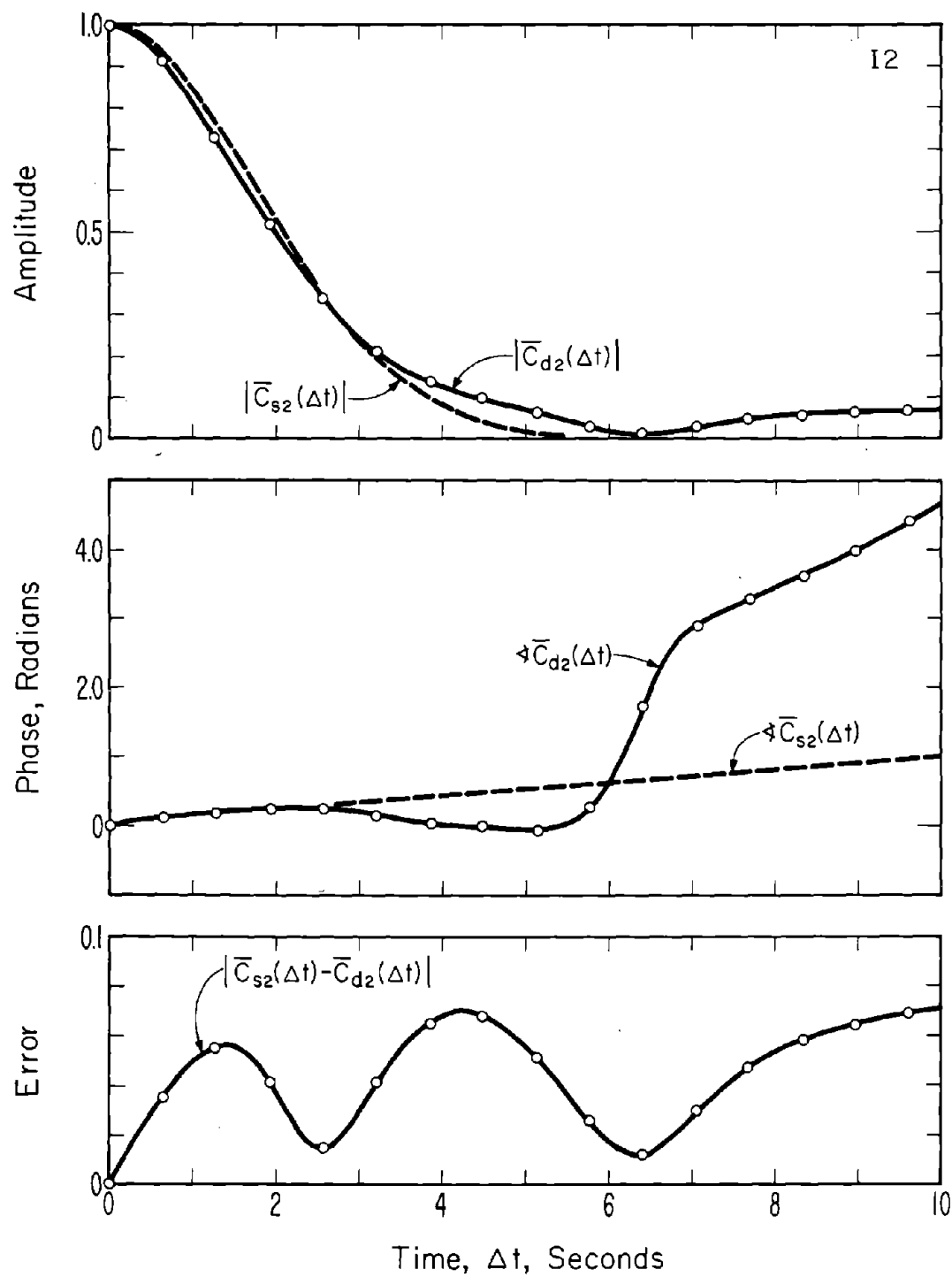


Figure 24. Tap-gain correlation functions for deterministic and statistical channels on path $i=2$ in sample I2.

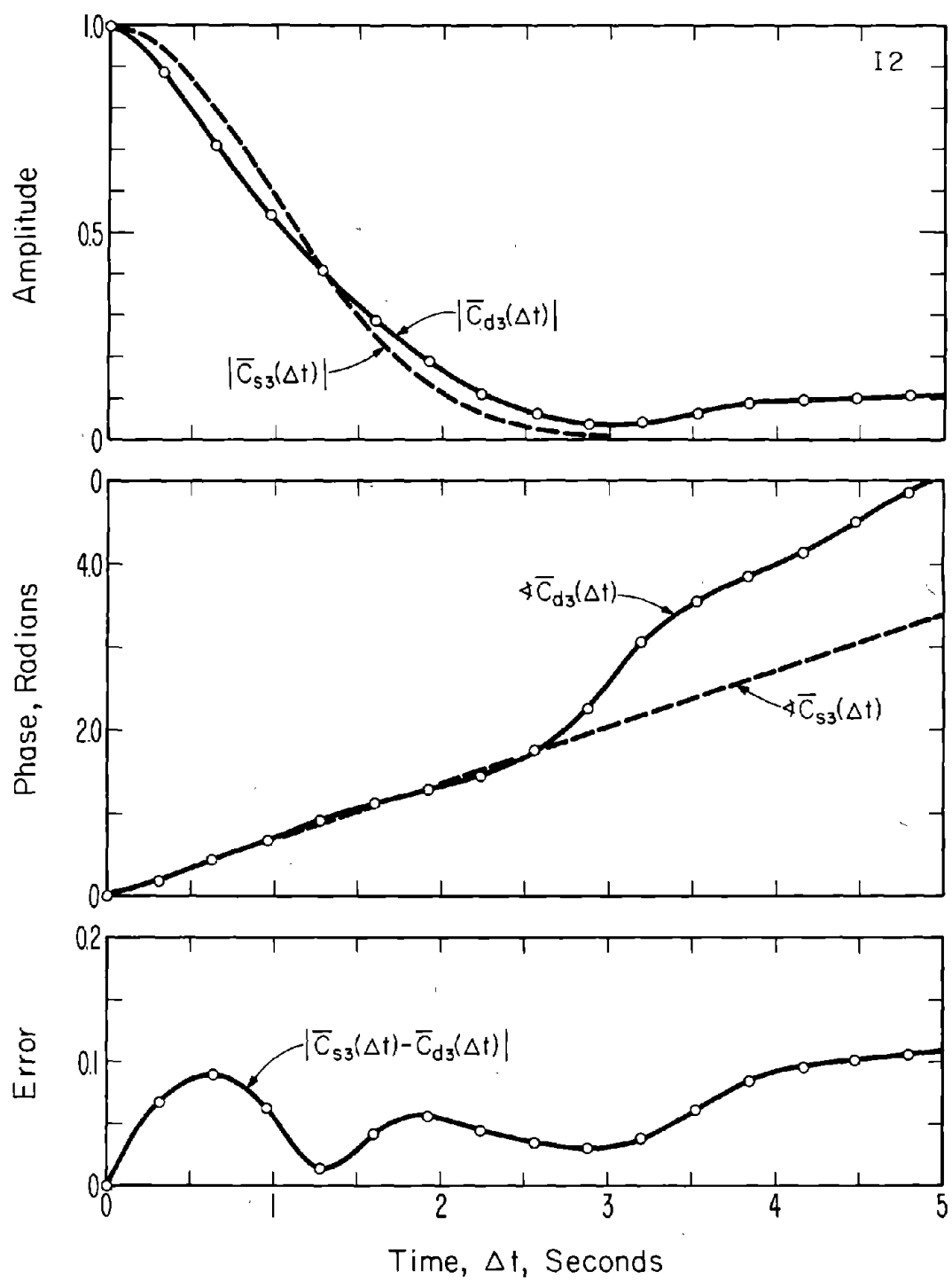


Figure 25. Tap-gain correlation functions for deterministic and statistical channels on path $i = 3$ in sample I2.

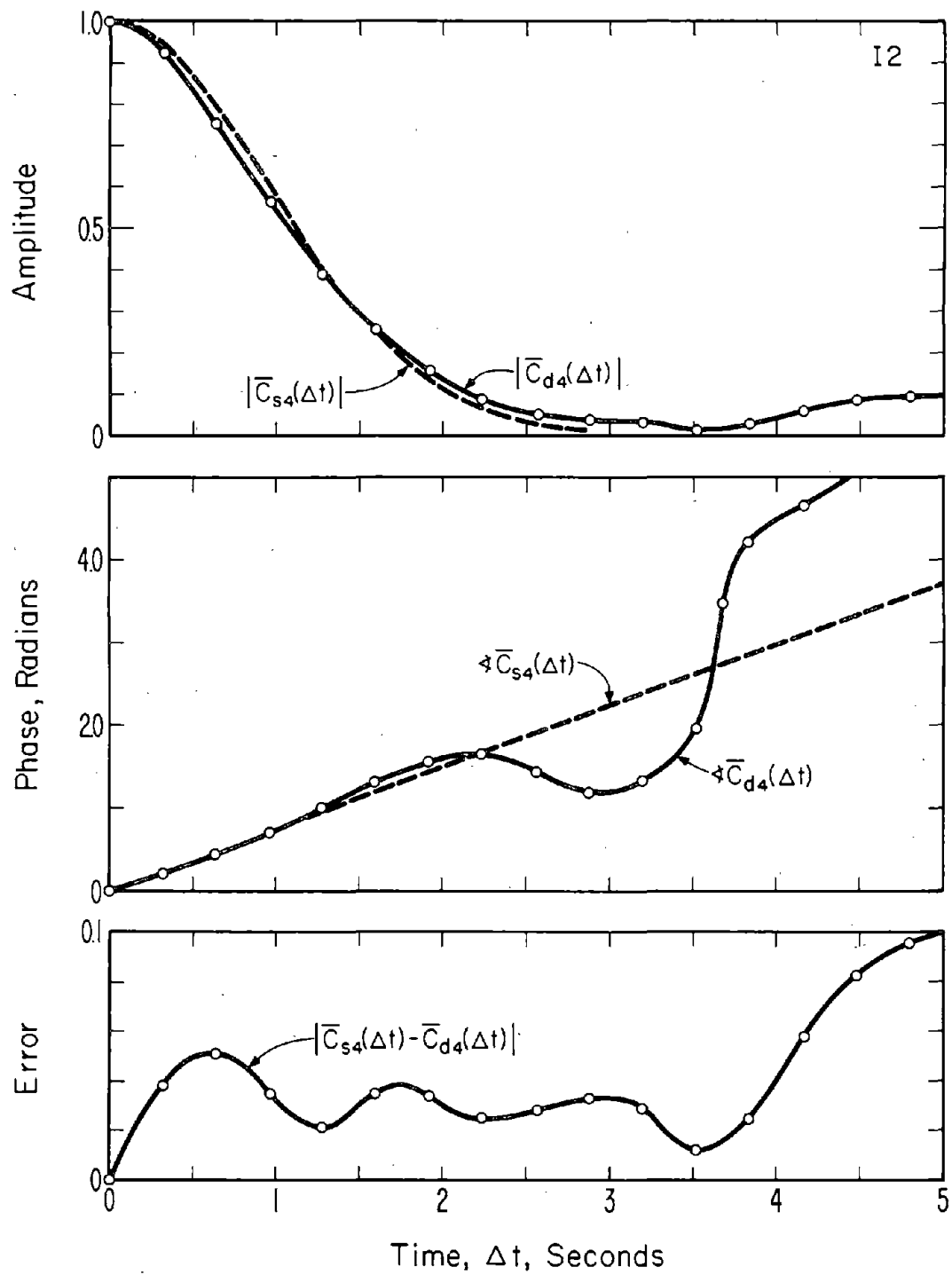


Figure 26. Tap-gain correlation functions for deterministic and statistical channels on path $i = 4$ in sample I2.

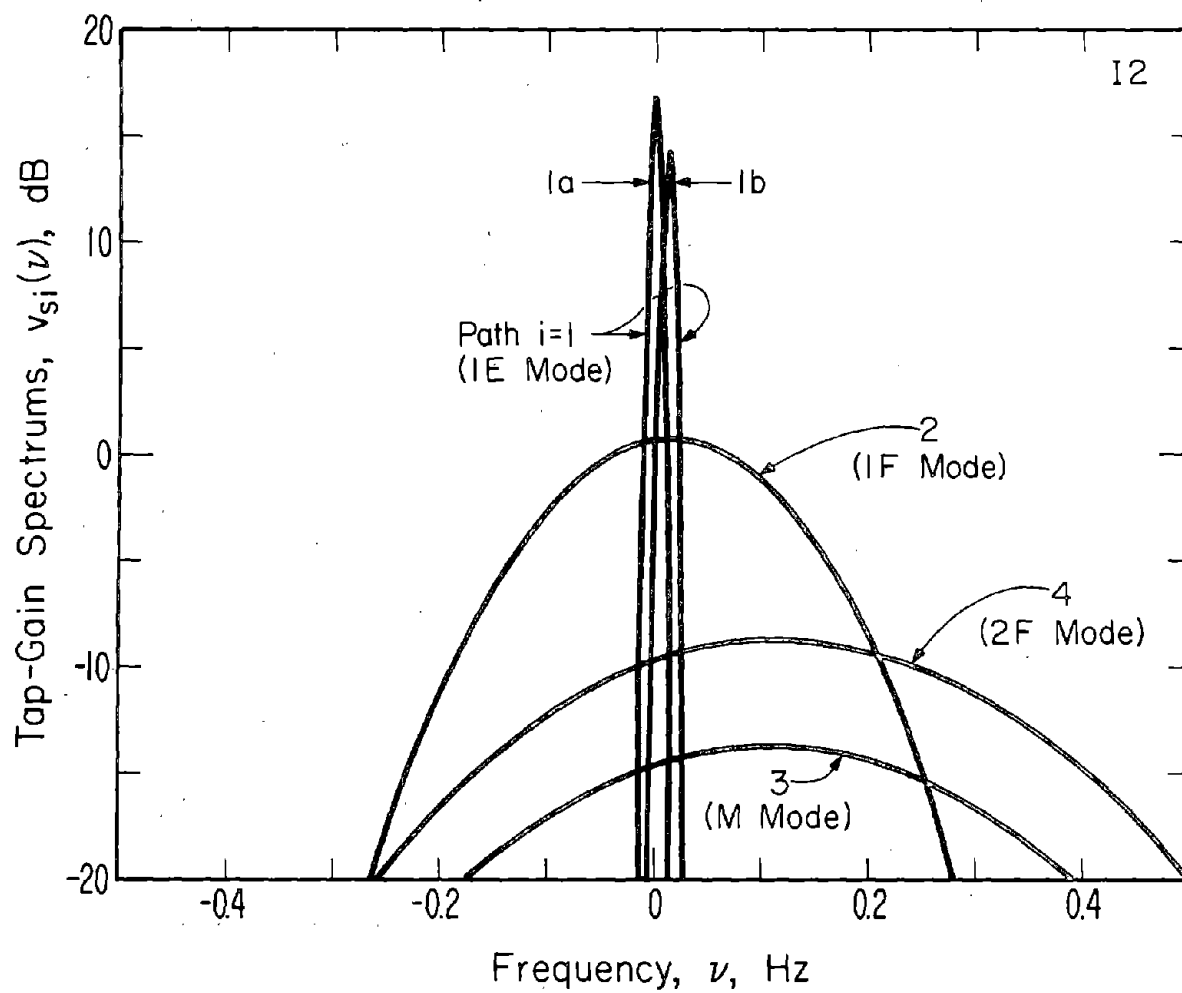


Figure 27. Tap-gain spectrums for the statistical channel in sample I2.

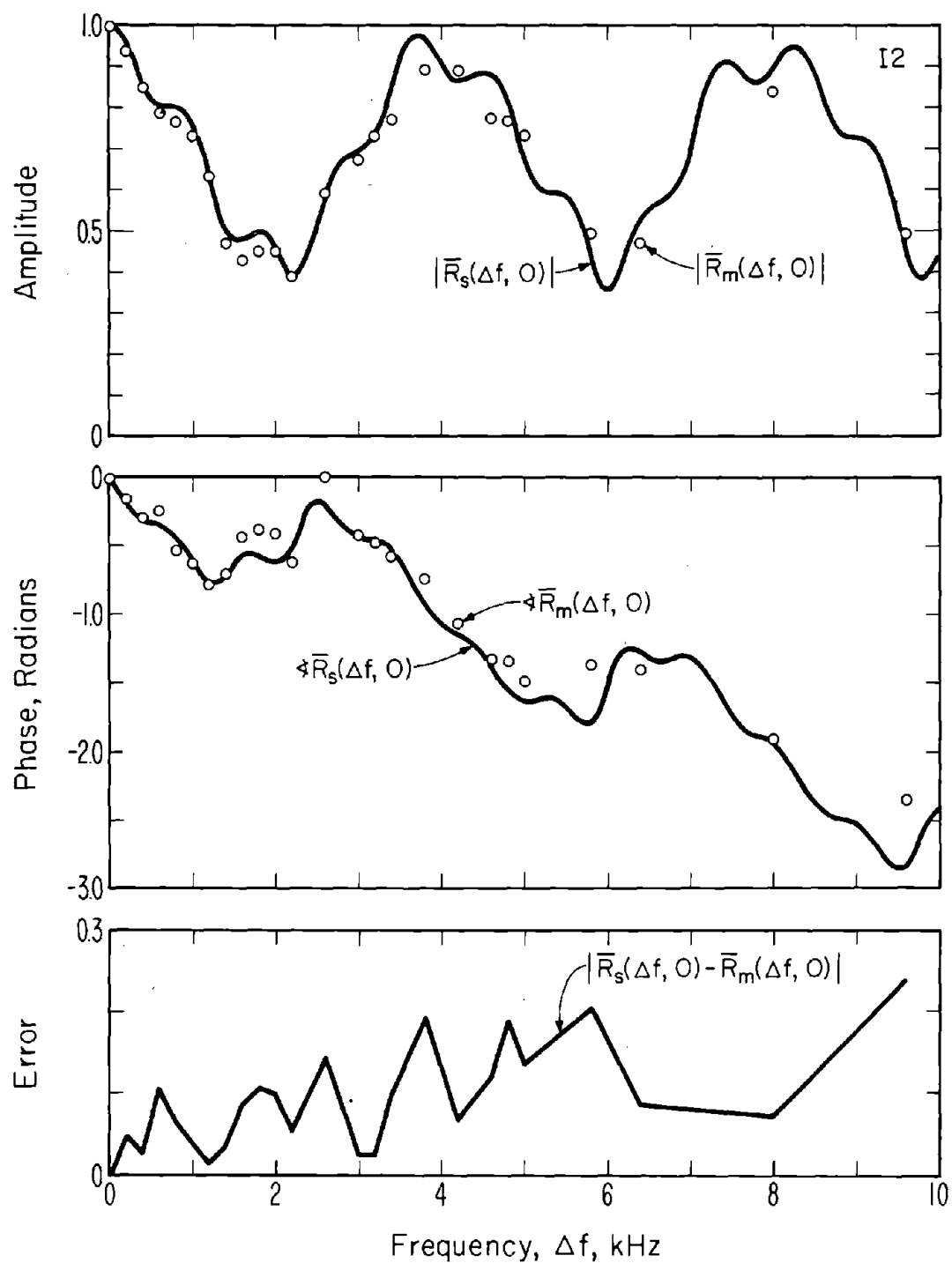


Figure 28. Channel correlation functions on the frequency axis for measured and statistical channels in sample I2.

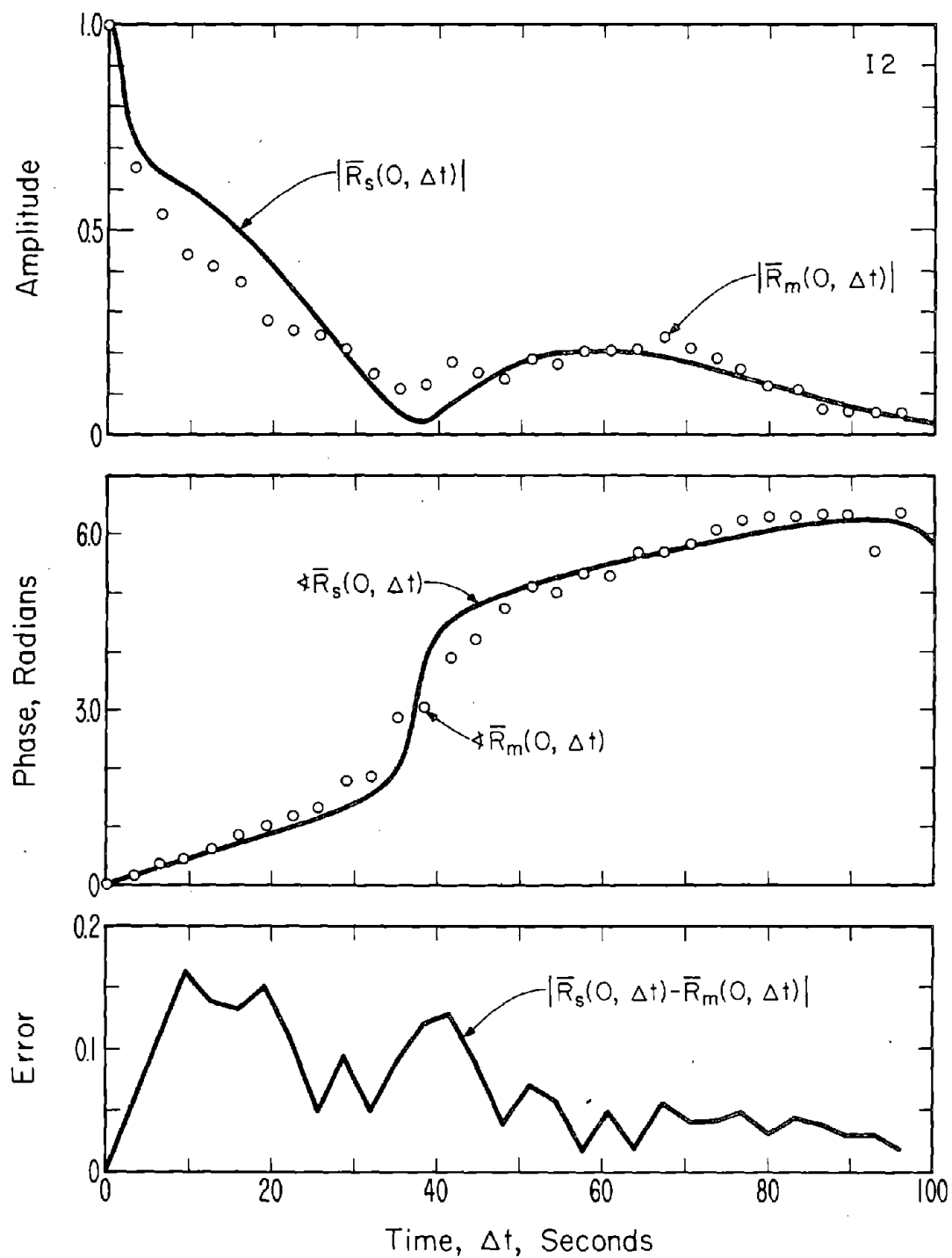


Figure 29. Channel correlation functions on the time axis for measured and statistical channels in sample 12.

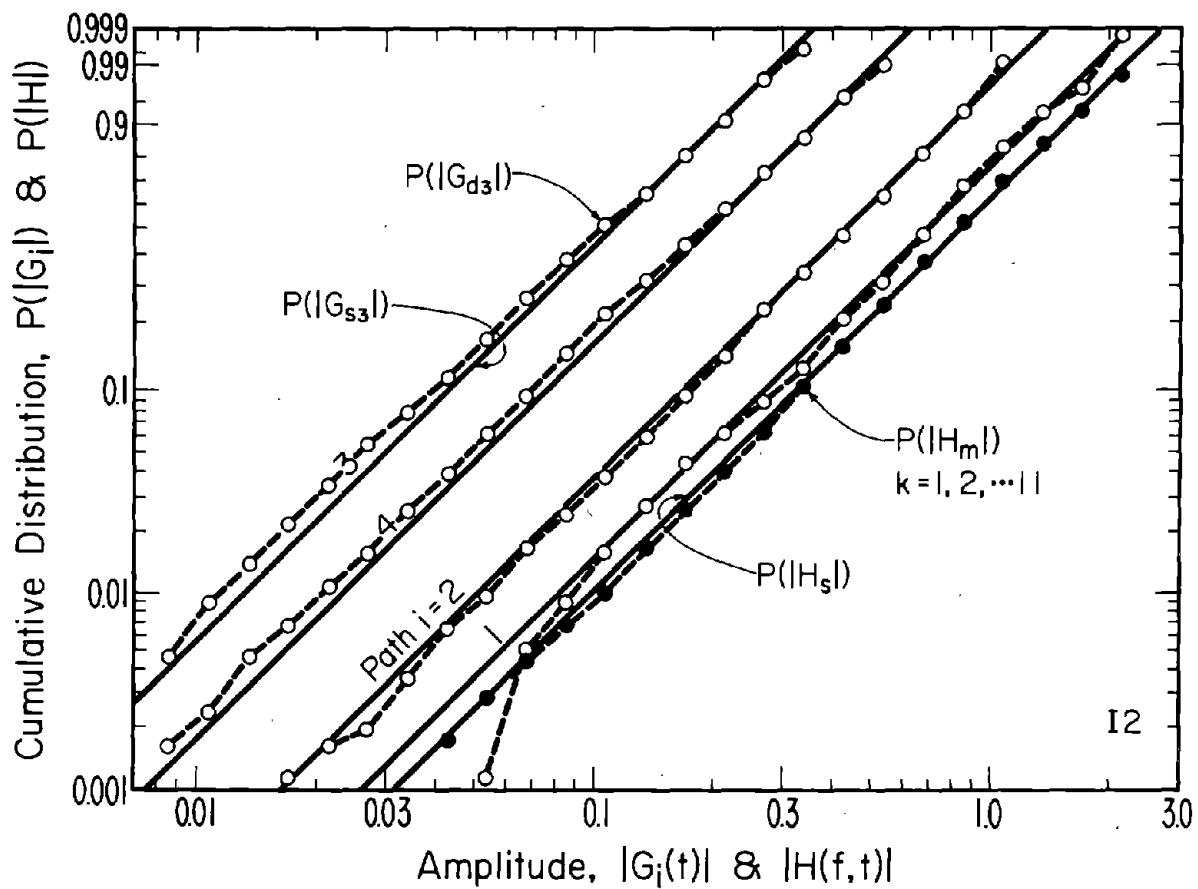


Figure 30. Cumulative distributions of the magnitudes of the tap-gain functions in the deterministic and statistical channels in sample 12.

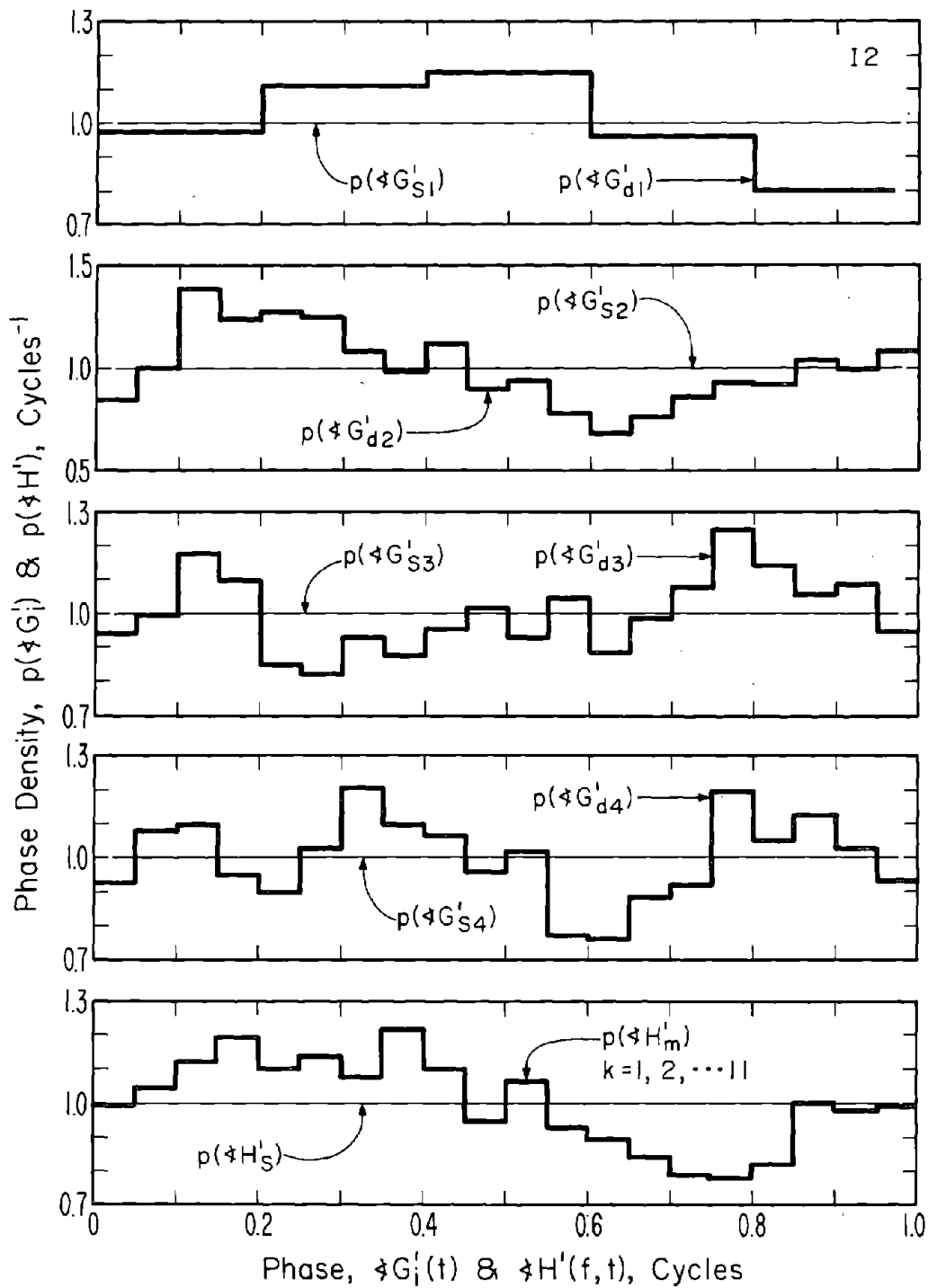


Figure 31. Histograms of the phases of the tap-gain functions in the deterministic and statistical channels in sample 12.

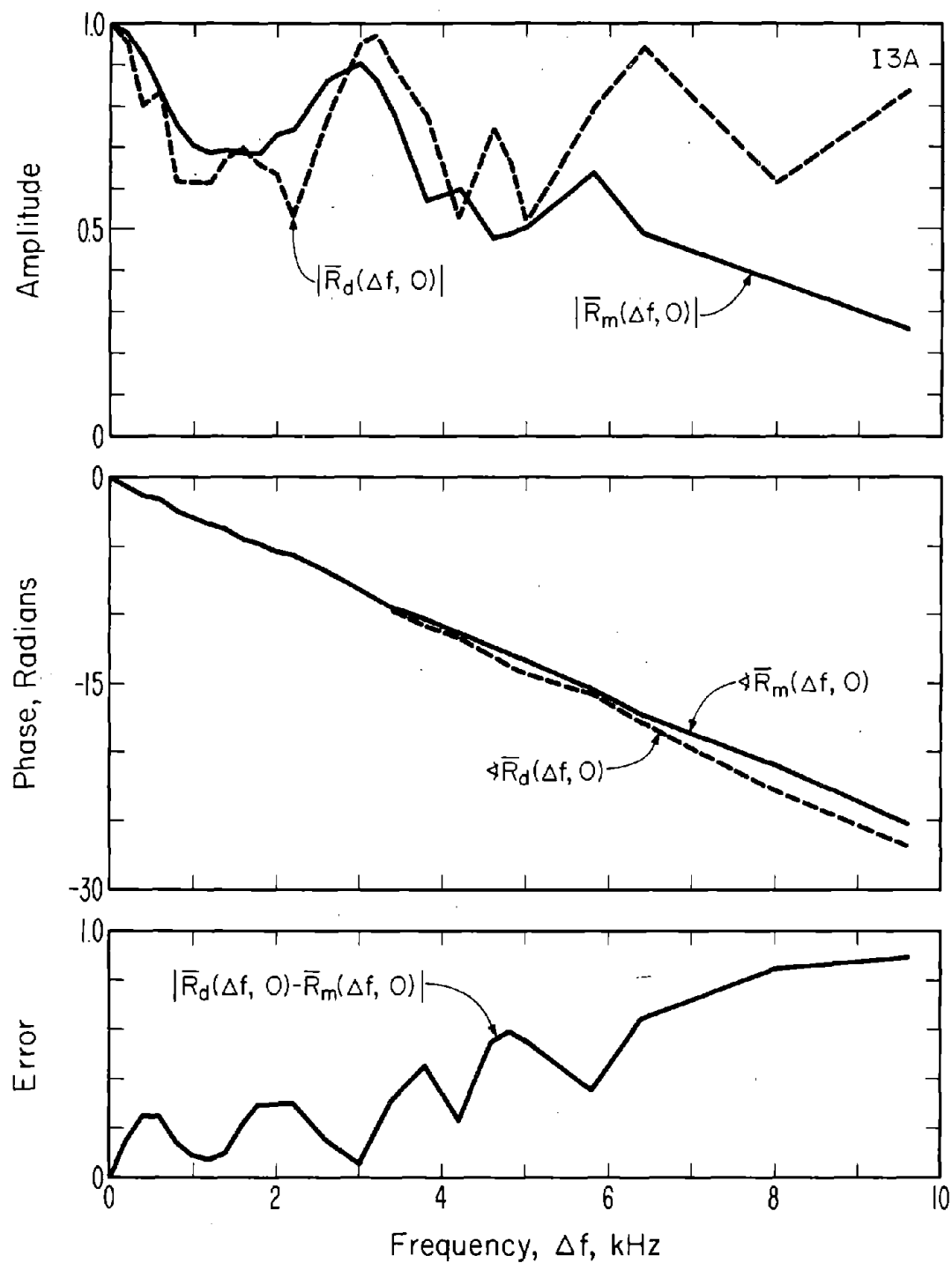


Figure 32. Channel correlation functions on the frequency axis for measured and deterministic channels in sample I3A.

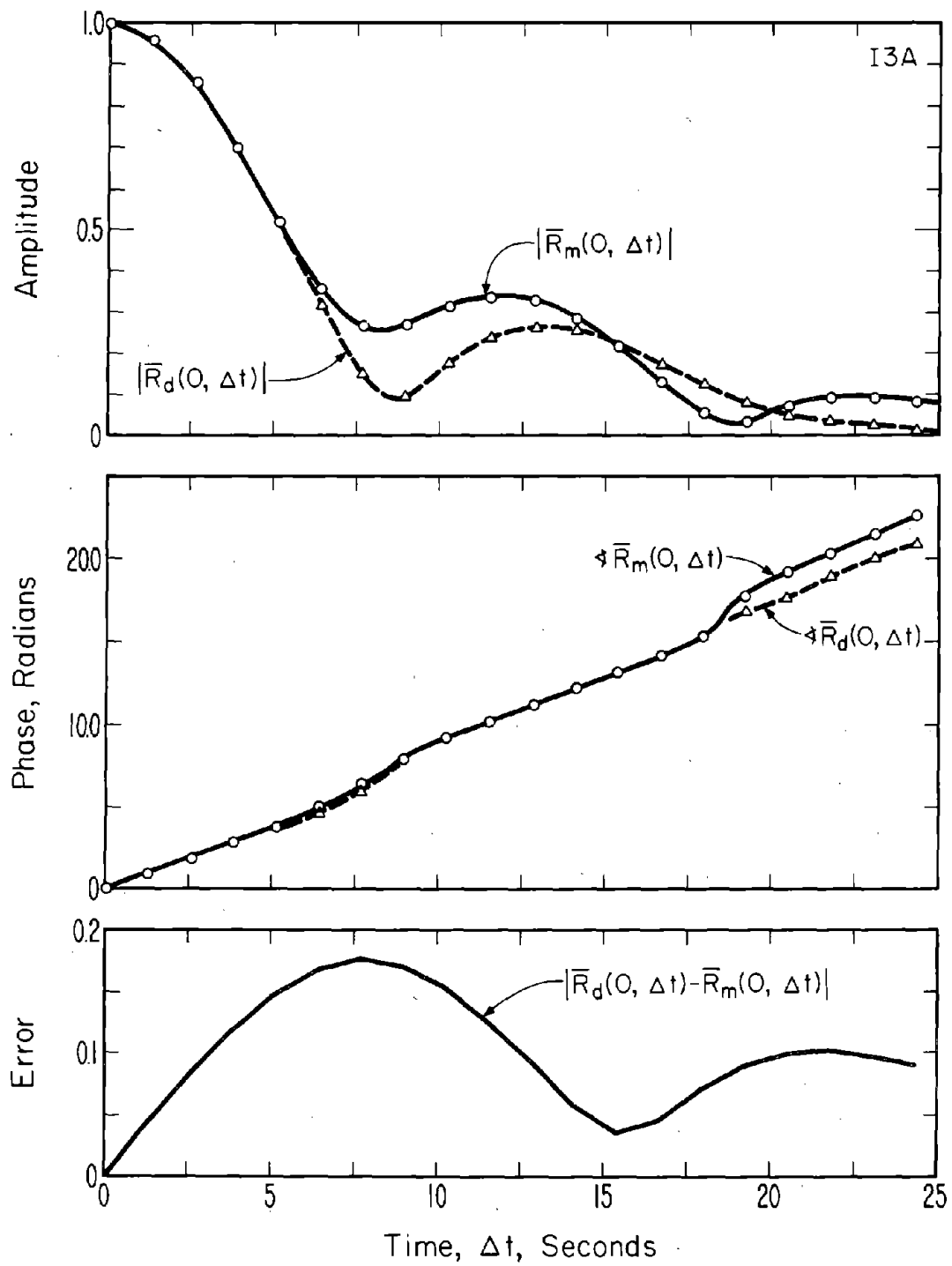


Figure 33. Channel correlation functions on the time axis for measured and deterministic channels in sample I3A.

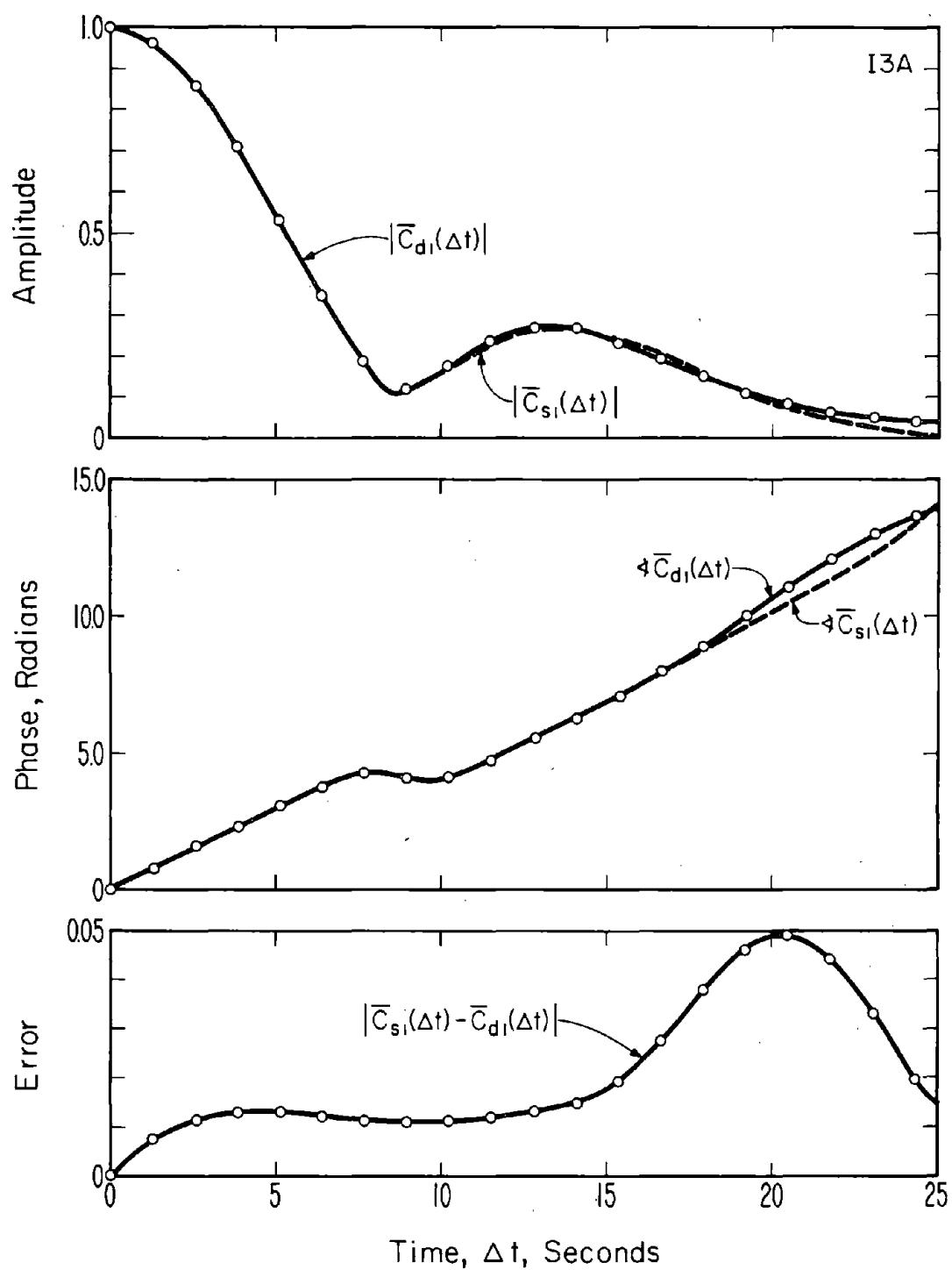


Figure 34. Tap-gain correlation functions for deterministic and statistical channels on path $i=1$ in sample I3A.

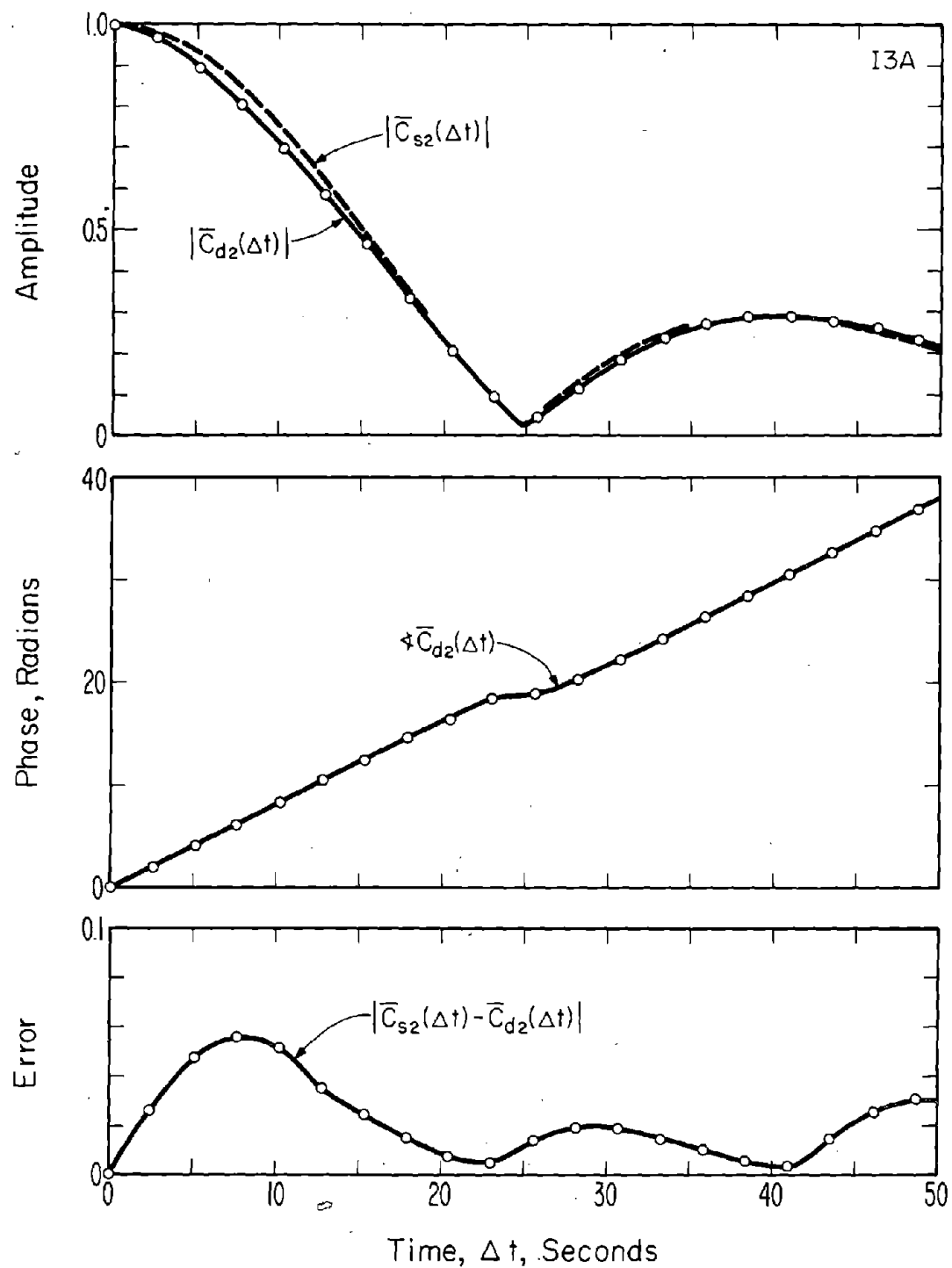


Figure 35. Tap-gain correlation functions for deterministic and statistical channels on path $i=2$ in sample I3A.

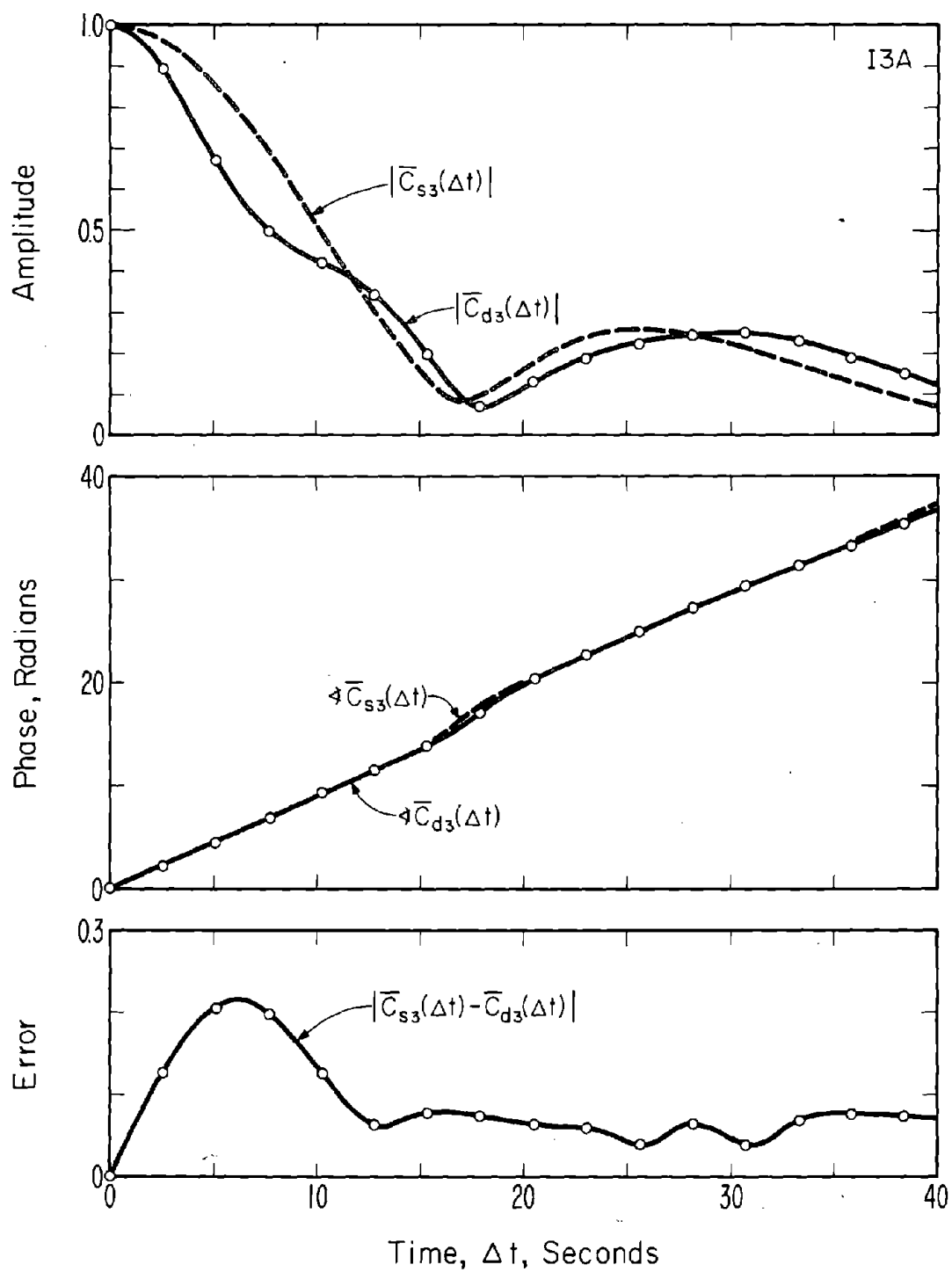


Figure 36. Tap-gain correlation functions for deterministic and statistical channels on path $i=3$ in sample I3A.

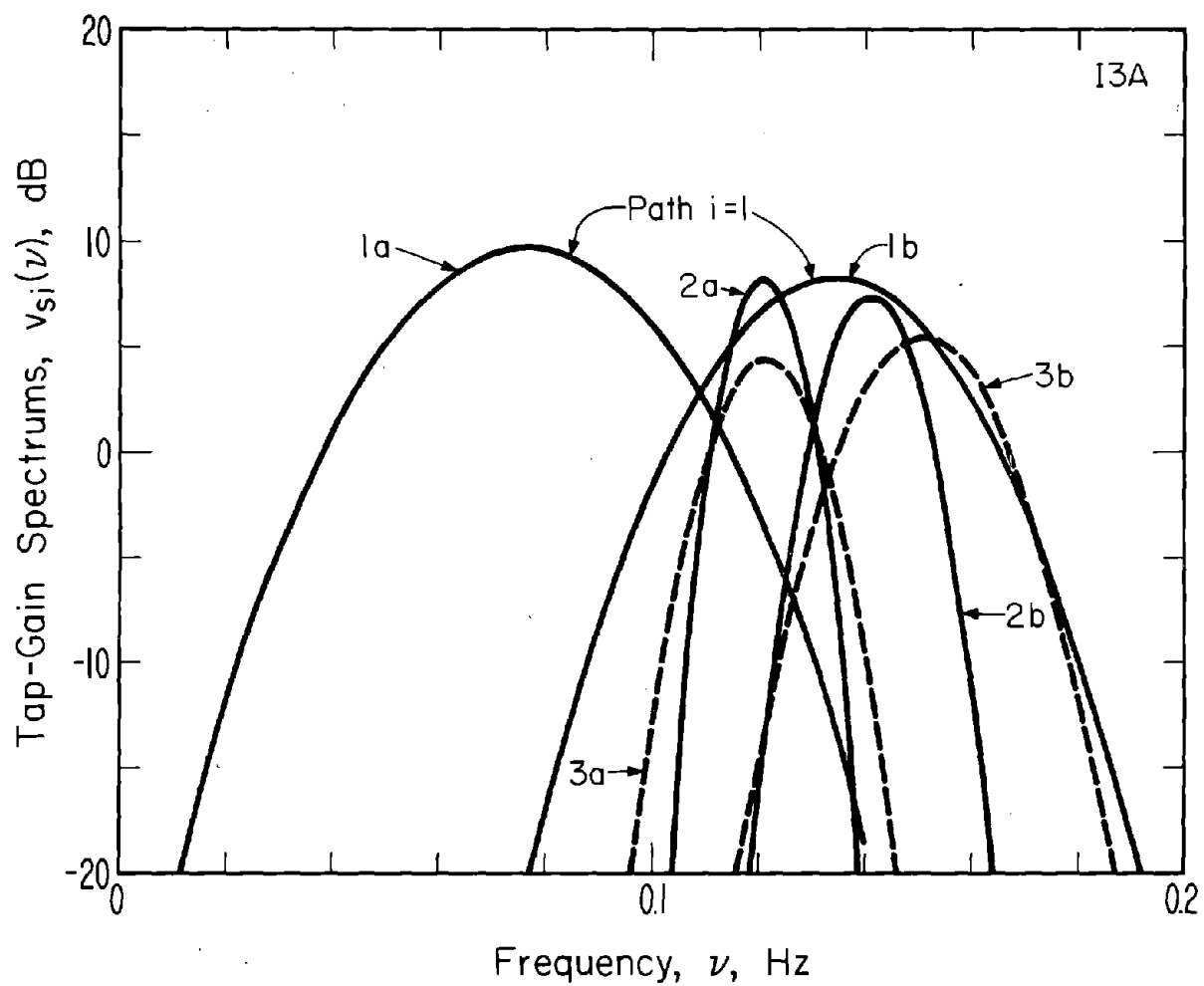


Figure 37. Tap-gain spectrums for the statistical channel in sample I3A.

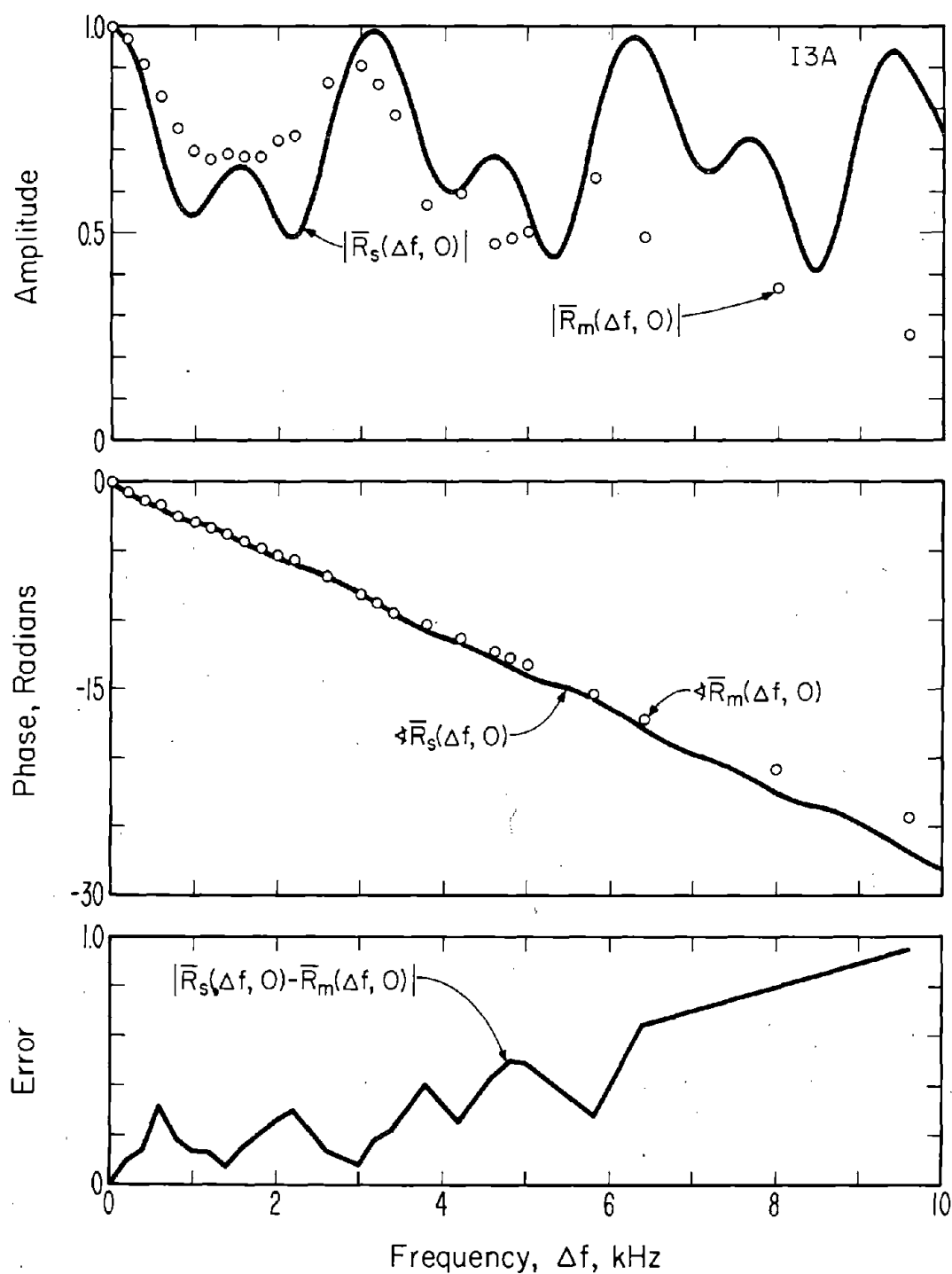


Figure 38. Channel correlation functions on the frequency axis for measured and statistical channels in sample I3A.

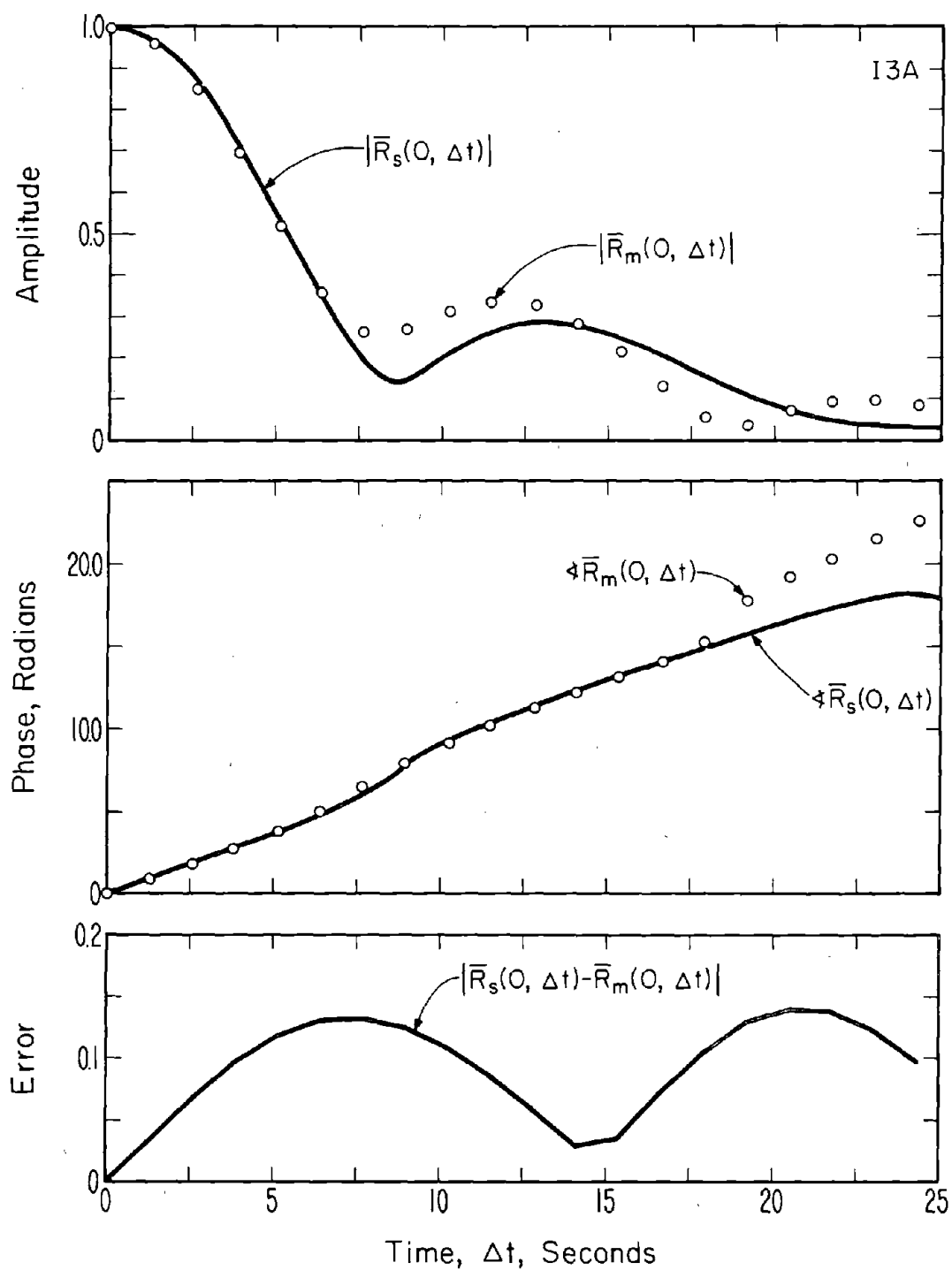


Figure 39. Channel correlation functions on the time axis for measured and statistical channels in sample I3A.

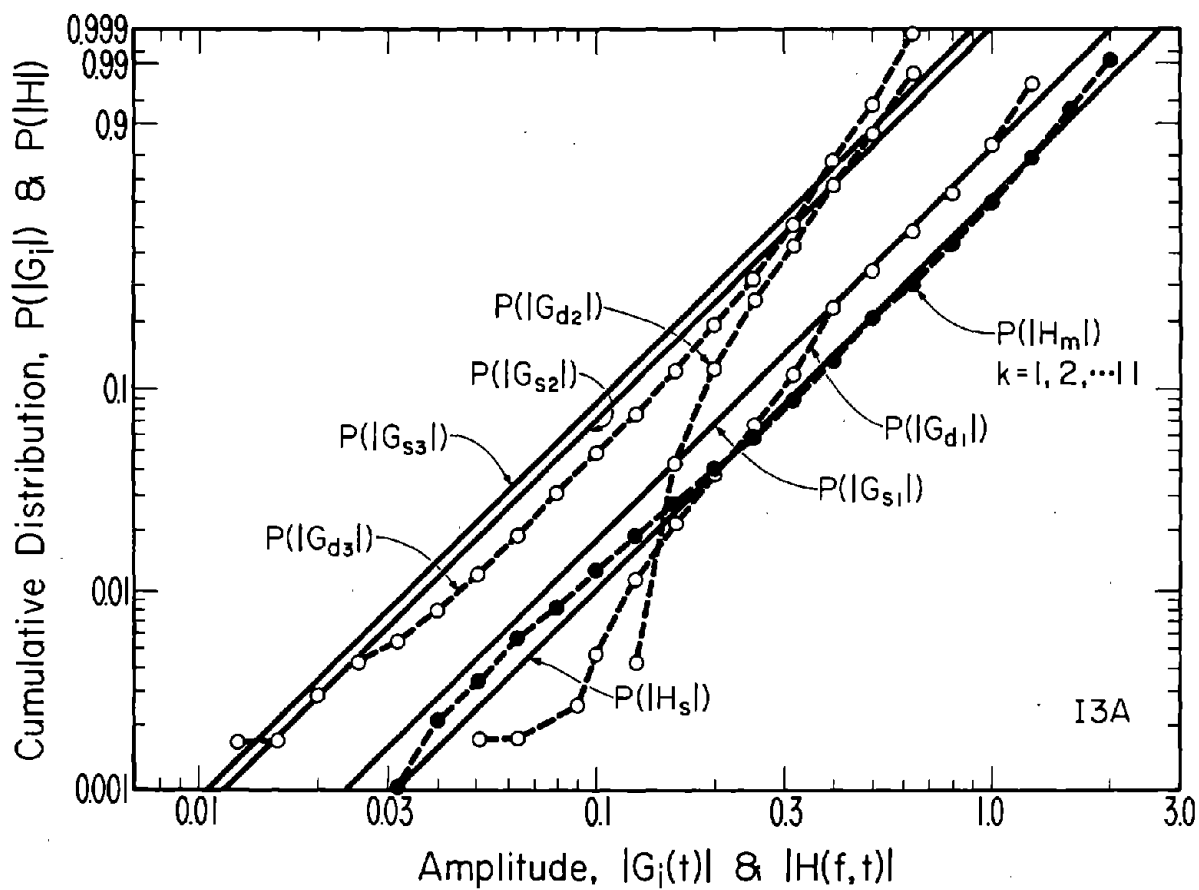


Figure 40. Cumulative distributions of the magnitudes of the tap-gain functions in the deterministic and statistical channels in sample I3A.

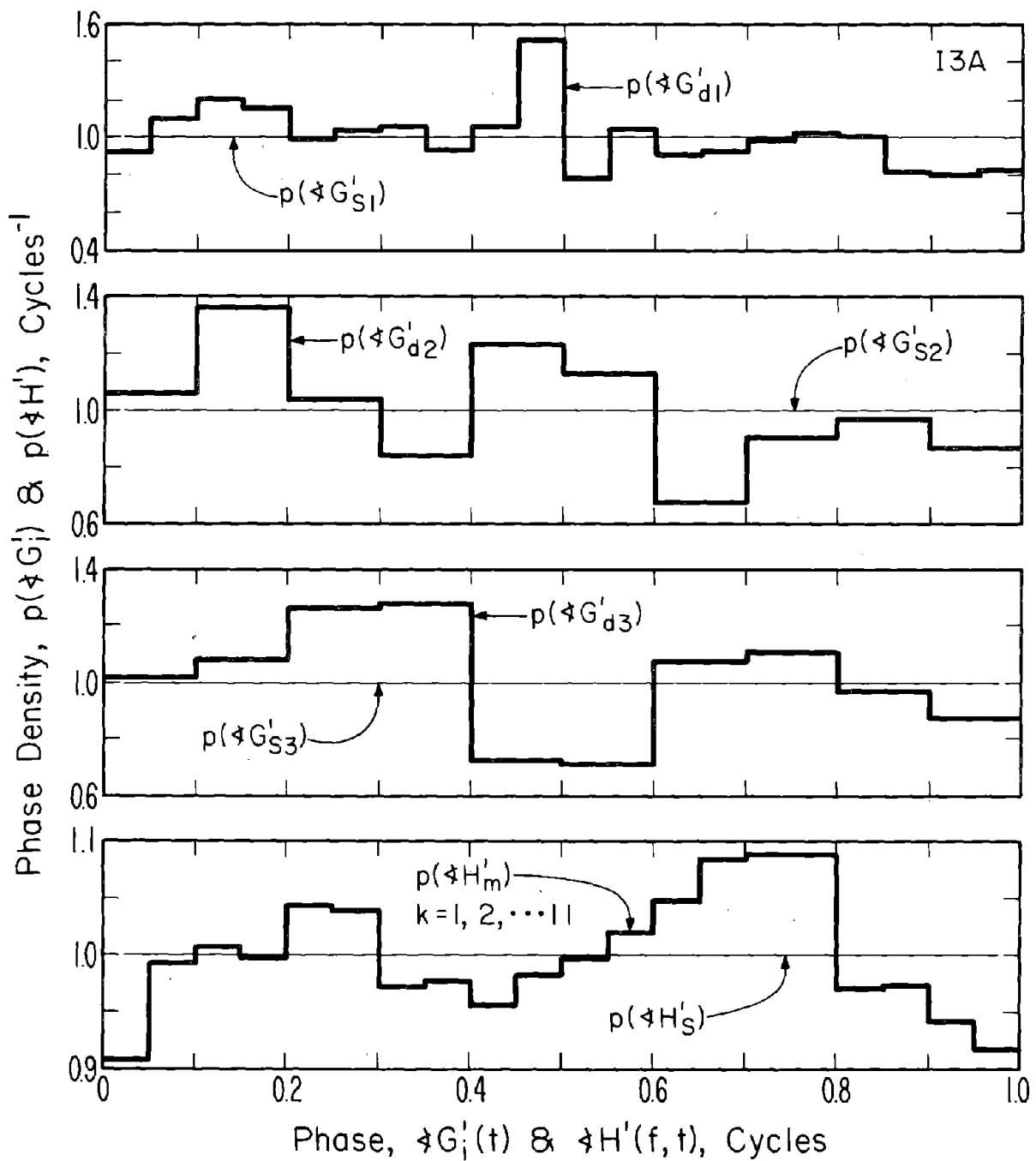


Figure 41. Histograms of the phases of the tap-gain functions in the deterministic and statistical channels in sample 13A.

